



NTNU – Trondheim
Norwegian University of
Science and Technology

Investigation of Low Temperature Toughness and Crack Initiation In Welded Structural Steels

Therese Vadholm

Materials Science and Engineering

Submission date: June 2014

Supervisor: Odd Magne Akselsen, IPM

Co-supervisor: Erling Østby, DNV

Norwegian University of Science and Technology
Department of Engineering Design and Materials

Preface

This master's thesis has been submitted to the Norwegian University of Science (NTNU) and Technology and Department of Engineering Design and Materials as a part of the Master's degree program in Materials Science and Engineering. The responsible supervisor at NTNU has been Odd Magne Akselsen, and co-supervisor has been Dr. Erling Østby from Det Norske Veritas Germanischer Lloyd (DNV GL). The work has been performed in cooperation with SINTEF as part of the Arctic Materials project and in cooperation with DNV GL. The master's thesis has been written while studying at UC Berkeley and finalized at NTNU.

I would like to express my gratitude to Agnes Marie Horn and Erling Østby from DNV GL for their guidance and knowledgeable advice and for giving me the opportunity to write my thesis in co-operation with DNV GL. I would also like to acknowledge the help I have received from Tore Andre Kristensen and Håkon Ottar Nordhagen from SINTEF. Kristensen has performed all of the tests at NTNU, while Nordhagen has contributed with valuable comments and remarks on the work performed.

I would also like thank Jefferey P. Clarkson at the Marvell NanoLab at UC Berkeley for helping out with training prior to the work performed on the SEM. A special thank you is also given to fellow student Torstein Grøstad in assistance in sample preparation for OLM and Synnøve Åldstedt at SINTEF for making it possible to image the samples with the LaPera etchant.

Furthermore, I would like to express my appreciation to Professor Ronald Gronsky at UC Berkeley for his assistance and noble advice and Professor Odd Magne Akselsen at NTNU for his guidance and support while writing this thesis and completing my degree.

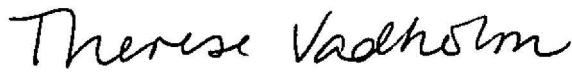
To my fellow students, friends and family: thank you for good conversations, advice, support good times over the five years that has passed while studying at NTNU and UC Berkeley.

Last, but not least I would like to direct a special thank you to the Norwegian Fulbright Association for supporting my stay in the United States.

Declaration

I hereby declare that this work has been carried out independently and according to the examination regulations of The Norwegian University of Science and Technology (NTNU).

Trondheim, June 12, 2014

A handwritten signature in black ink that reads "Therese Vadholm". The signature is written in a cursive style and is positioned above a horizontal line.

Therese Vadholm

Abstract

The work performed in this master's thesis includes the four following parts that relate to each other; (1) a characterization of microstructures in the heat affected zones of welded simulated steel test specimens using optical light microscopy, (2) a fracture surface investigation of Instrumented Charpy impact specimens tested at low temperatures using scanning electron microscopy, (3) a comparison of transition curves obtained from instrumented Charpy impact testing for V-notched and fatigue pre-cracked specimens and (4) a comparison of instrumented Charpy tests with quasi-static CTOD tests for weld simulated samples.

A 420 MPa HSLA steel has been investigated. Instrumented Charpy impact tests and quasi-static CTOD tests have been performed on specimens of weld simulated Coarse Grained Heat Affected Zone (CGHAZ) and Intercritically Reheated Coarse Grained Heat Affected Zone (ICCGHAZ) microstructures. Charpy specimens with both a conventional V-notch and a sharp crack obtained by fatigue pre-cracking have been tested above and below the ductile-to-brittle transition temperature. The aim of the first two parts has been to study the location of brittle fracture initiation sites in samples tested with both conventional V-notch and sharp fatigue pre-cracks. The fracture surfaces of CGHAZ and ICCGHAZ samples with both notch configurations have been examined in a Scanning Electron Microscope and the microstructures have been investigated in an Optical Light Microscope.

The transition curves obtained for all combinations of microstructure and notch configurations have been used to evaluate the effect of the blunt notch used in conventional Charpy testing as opposed to the sharp crack used in quasi-static fracture mechanical testing. In addition the effect of testing specimens with weld-simulated microstructures has been evaluated. The last part includes an evaluation of two different correlations that use Charpy impact test values to estimate fracture toughness obtained from quasi-static

fracture mechanical testing. The two correlations include the lower bound relation for lower shelf and lower transitional behaviour described in the British Standard (BS) BS7910 and Master Curve (MC) approach for the lower shelf transitional behaviour described in the American Society for Testing and Materials (ASTM) standard ASTM E1921.

The results show that the fracture toughness of the investigated steel is clearly deteriorated when subjected to welding, and was found to be lowest for the ICCGHAZ microstructure. The deteriorated fracture toughness is linked to the weld microstructures being more heterogeneous and to the MA constituents found in these. Introducing a fatigue pre-crack in the Charpy specimen was seen to have the effect of lowering the fracture resistance in terms of increasing the transition temperature. The difference in fracture toughness between the notched and pre-cracked was found to be largest within the transition region. The upper shelf plateau was found to be lower in the weld-microstructures tested compared to the base material. The scatter was found to be large within the transition region for all combinations of microstructure and notch sharpness, where the CGHAZ microstructure was shown to have the overall largest scatter. The test data was found to be more scattered when testing notched specimens compared to the pre-cracked specimens.

Several initiation sites were found close to the notch and fatigue pre-crack in the investigated fracture surfaces. For specimens with a pre-crack, the initiation sites were seen to occur closer to the fatigue crack than in the notched specimens tested at the same temperature for the same microstructure. The notched specimens show a more ductile appearance compared to the pre-cracked specimens at the same test temperature. A ductile region was found in front of the cleavage area in the samples tested at the highest test temperatures.

Some of the parameters that can be obtained from the instrumented Charpy data recorded were discussed. These include the energy measured to maximum load, the energy measured to the onset of brittle fracture initiation and the fractions of the total measured energy these energies make. These were linked to the five different curve classes defined for instrumented Charpy curves. The increase in maximum load with curve class number was seen to resemble the increase in the measured CTOD values with temperature. The change in energies to maximum load and to the onset of brittle fracture with temperature were seen to have a shape that resembled the Charpy transition curves. The curve classes

obtained at the lowest test temperatures show signs of early fracture initiation. It has been challenging to classify some of these curves. The validity of these curves are also uncertain. This was mainly a result of early fracture initiation where un-dissipated inertia effects leads to oscillations in the measured load.

The lower bound relation after BS7910 was shown not shown to provide a good coefficient correlation for the microstructures tested, although conservative results were obtained for the pre-cracked parallels. The Master Curve relation was seen to provide better estimates of the CTOD. The degree of correlation was best for the ICCGHAZ microstructure tested. When using the MC correlation, changing the parameters in the correlation were shown to have a large impact on the degree of correlation. A difference in how the two standards investigated, ASTM E1921 and BS7910, define some of these parameters were also found. A suggestion in using data obtained from instrumented Charpy testing in obtaining new and alternative correlations to estimate parameters obtained from quasi-static fracture mechanical tests from Charpy test data was proposed.

Sammendrag

Denne masteroppgaven består av følgende fire deler som er knyttet til hverandre; (1) karakterisering av mikrostrukturen i ulike sveisesoner ved hjelp av optisk lysmikroskopi, (2) undersøkelse av bruddflater fra instrumentert Charpy-testing ved lave temperaturer ved hjelp av elektronmikroskopi, (3) sammenligning av omslagskurver fra instrumentert Charpy- testing med prøver med V-skår og skarp sprekk (4) en sammenligning av instrumentert Charpy og kvasistatiske CTOD tester for sveisesimulerte prøver.

Et 420 MPa-stål har blitt undersøkt. Instrumentert Charpy og kvasistatisk CTOD testing har blitt utført med prøver av sveisesimulerte CGHAZ og ICCGHAZ mikrostrukturer. Charpy-prøver med både konvensjonelt V-skår og skarp utmattingssprekk har blitt testet. Hensikten med de to første delene har vært å studere hvor sprøbruddinitiering skjer i prøver testet med både konvensjonelt V-skår og skarp utmattingssprekk for temperaturer både over og under omslagstemperaturen for duktilt og sprøtt brudd. Bruddflater av CGHAZ og ICCGHAZ prøver med begge skårkonfigurasjoner har blitt undersøkt i et Scanning Elektron Mikroskop og mikrostrukturene har blitt undersøkt i et optisk lysmikroskop.

Omslagskurvene funnet for alle kombinasjoner av mikrostruktur og skårkonfigurasjon har blitt brukt til å evaluere effekten av det uskarpe skåret som vanligvis benyttes i Charpy-testing, i motsetning til den skarpe sprekken brukt i kvasi-statisk bruddmekanisk testing. I tillegg har påvirkningen ulike sveisemikrostrukturer har gitt på resultatene når skårets skarphet endres blitt evaluert. I den siste delen inngår en evaluering av to ulike korrelasjoner som benytter verdier fra Charpy slagprøving til å estimere bruddseighet oppnådd gjennom kvasi-statisk bruddmekanisk testing. De to korrelasjonene inkluderer "Lower Bound"-korrelasjon for nedre platå og nedre omslagsområde beskrevet i British Standard BS7910 og en Master Curve-tilnærming for nedre platå og nedre omslagsområde beskrevet i ASTM standard ASTM E1921 og BS7910.

Resultatene viser at bruddseigheten til det undersøkte stålet er betydelig dårligere etter sveisesimulering, hvor bruddseigheten var lavest for ICCGHAZ mikrostrukturen. Den lave bruddseigheten ble knyttet til at mikrostrukturen i de sveisesimulerte prøvene er mer heterogen, og til MA-bestanddelene som ble funnet i disse. Effekten av å teste Charpy-prøver med utmattingsprekk istedenfor V-skår var senket bruddmotstand i form av økt omslagstemperatur. Forskjellen i bruddseigheten mellom prøver med V-skår og utmattingsprekk viste seg å være størst i overgangsområdet. Det øvre energi plåtet av Charpy-omslagskurvene var lavere for de sveisesimulerte mikrostrukturene som ble testet sammenlignet med grunnmaterialet. Spredningen i data var størst i omslagsområdet for alle kombinasjoner av mikrostruktur og sprekkskarphet testet. CGHAZ mikrostrukturen viste seg å ha størst spredning for alle test temperaturer. Resultatene viste også at spredningen i data var større ved testing av prøver med V-skår enn med skarp utmattingsprekk.

Flere initieringspunkter ble funnet ved enden av V-skåret og utmattingsprekken i de undersøkte bruddflatene. For prøver med utmattingsprekk ble initieringspunktene observert nærmere enden av sprekkene enn i prøvene med V-skår for prøver testet ved samme temperatur og mikrostruktur. I tillegg hadde bruddflatene fra prøver med V-skår mer duktilt utseende i forhold til prøver med skarp sprekk testet ved samme temperatur. Et duktilt område ble funnet foran området med kløyvningsbrudd i noen av prøvene testet ved de høyeste test temperaturene.

Noen av parameterne funnet fra data oppnådd fra instrumentert Charpy-testing ble diskutert. Disse inkluderer energien målt før høyeste målte last, energien målt til last ved sprøbrudd initiering og fraksjonene disse utgjør av den totale målte energien. Fraksjonene ble knyttet til fem ulike kurveklasser som er definert for å klassifisere kurver fra instrumentert Charpy-testing. Det ble observert at høyeste målte last økte med kurveklassenummer. Formen på denne kurven lignet økningen i målte CTOD verdier med temperatur. Endringen i energi absorbert før maksimal last og til last ved sprøbruddinitiering med temperatur ble observert å ha en form som lignet Charpy-overgangskurvene. Kurveklassene oppnådd ved de laveste testtemperaturene viste tegn på tidlig bruddinitiering. Det har vært vanskelig å klassifisere en del av disse kurvene og gyldigheten til kurvene er også usikker. Årsaken til dette var hovedsakelig

tidlig bruddinitiering, hvor treghets effekter kan ha ført til store svingninger i den målte belastning tidlig i testforløpet.

"Lower Bound"-korrelasjonen for nedre platå og nedre omslagsområde fra BS7910 ble viste lav grad av korrelasjon mellom estimerte og målte CTOD verdier for mikrostrukturene som ble testet, selv om konservative resultater ble oppnådd for paralleller testet med prøver med skarp utmattingssprekk. Master Curve korrelasjonen viste seg å gi noe bedre estimater av reelle CTOD verdier. Graden av korrelasjon var best for ICCGHAZ mikrostrukturen. Ved bruk av MC korrelasjonen, viste det seg at de ulike parameterne som inngår i korrelasjonen har en stor innvirkning på hvor godt samsvaret mellom estimerte og målte verdier er. Det ble funnet forskjeller i hvordan de to undersøkte standardene hvor MC metoden inngås, ASTM E1921 og BS7910, definerer noen av disse parameterne. Et forslag til å bruke data og parametere oppnådd ved instrumentert Charpy-testing til å utvikle nye og alternative korrelasjoner for å estimere parametere oppnådd ved kvasi-statisk bruddmekanisk testing fra Charpy-data ble foreslått.

List of Acronyms

AFSuM	Accurate Fracture Substantiation Method
ASTM	American Society for Testing and Materials
BCC	Body Centered Cubic
BCT	Body Centered Tetragonal
BS	British Standard
CE	Carbon Equivalent
CGHAZ	Coarse Grained Heat Affected Zone
CMOD	Crack Mouth Opening Displacement
CT	Compact Tension
CTOD	Crack Tip Opening Displacement
CCT	Continous Cooling Temperature
CVN	Charpy-V Notch
DBT	Ductile-to-Brittle Transition
DBTT	Ductile-to-Brittle Transition Temperature
DNV GL	Det Norske Veritas Germanischer Lloyd
DP	Diamond Paste
EDM	Electro Discharge Machined
EPFM	Elastic Plastic Fracture Mechanics
FCC	Face Centered Cubic
FGHAZ	Fine Grained HAZ
HAZ	Heat Affected Zone
HSLA	High Strength Low Alloy
ICCGHAZ	Intercritically Reheated Coarse Grained Heat Affected Zone
ICHAZ	Intercritical HAZ

IIW	International Institute of Welding
ISO	International Standardisation Organisation
IT	Isothermal Temperature
LAST	Lowest Anticipated Service Temperature
LBZ	Local Brittle Zones
LE	Lateral Expansion
LEFM	Linear Elastic Fracture Mechanics
MA	Martensite-Austenite
MAC	Martensite-Austenite-Carbide
MC	Master Curve
PCM	Parameter of Crack Measurement
RCN	The Research Council of Norway
NTNU	The Norwegian University of Science and Technology
RSD	Relative Standard Deviation
SA	Percent Shear Area
SCCGHAZ	Subcritically Reheated Coarse Grained Heat Affected Zone
SCHAZ	Subcritical HAZ
SD	Standard Deviation
SEM	Scanning Electron Microscope
SENB	Single Edge Notch Bend
SMACC	Fundamental Studies of Materials' behaviour for future Cold Climate applications
SMYS	Specified Minimum Yield Strength
SSY	Small Scale Yielding
TMCP	Thermo-Mechanically Controlled Processing
wt	Weight

Nomenclature

Latin Letters

a	Crack length	mm
a_0	Initial crack length	mm
A_1	Temperature for eutectoid transformation from austenite to ferrite in the phase diagram of steel. A_{e1} and A_{c1} commonly used for plain carbon steels and alloys, respectively	°C
A_3	Transformation line between the austenite and ferrite-austenite in the phase diagram of steel. A_{e3} and A_{c3} commonly used for plain carbon steels and alloys, respectively	°C
B	Thickness of a specimen	mm
C_V	Measured absorbed Charpy V-notch impact energy	J
$C_{V,c}$	Calculated Charpy V-notch impact energy	J
$C_{V,f}$	Amount of C_V measured at the onset of brittle fracture initiation	J
$\frac{C_{V,f}}{C_{V,c}}$	Fraction of absorbed energy calculated up to maximum load over the total calculated absorbed energy	-
$C_{V,m}$	Amount of total C_V measured up to maximum load	J
$\frac{C_{V,m}}{C_{V,c}}$	Fraction of absorbed energy calculated to maximum load over the total calculated absorbed energy	-
C_{V-US}	Upper-self C_V value	J
E	Young's modulus	GPa

F	Load/force	N
F_a	Load at fracture arrest	N
$f\left(\frac{a}{W}\right)$	Correction factor in fracture toughness calculations	-
G	Energy release rate	J/m ²
F_{gy}	Load at general yielding	N
F_m	Maximum load	N
F_u	Load at fracture initiation	N
J	The J-integral	J/mm ²
K	Stress intensity factor	MPa√m
K_{crit}	Critical stress intensity factor	MPa√m
K_i	K corresponding to specific applied load, P_i , during CTOD testing	MPa√m
K_I	Crack driving force	MPa√m
K_{Ia}	Static fracture arrest toughness	MPa√m
K_{IA}	Dynamic fracture arrest toughness	MPa√m
K_{IC}	Critical stress intensity factor for mode I loading	MPa√m
K_{ID}	Dynamic fracture toughness	MPa√m
K_{JC}	Critical stress intensity factor based on the J-integral. Equal to K_{mat} in the correlations	
K_{mat}	Estimated toughness	MPa√m
m	Effective mass of Charpy pendulum corresponding to its effective weight	kg
P_f	Probability for failure at or before K_{mat} for an arbitrarily chosen sample from a population of specimens (ASTM1921), probability of K_{mat} being less than estimated (BS7910)	-
P_i	Applied load CTOD test used in K calculations	kN
q	Heat input during welding	mm

r	Distance from the crack tip	mm
s	Bending displacement of specimen during Charpy testing	mm
s_m	Bending displacement at maximum load	mm
S	Specimen span	mm
t	Time	s
t_0	Time at the beginning of the deformation	s
T	Temperature	°C
T_0	Reference temperature at which the median fracture toughness is $100 \text{ MPa}\sqrt{m}$ in a 25 mm thick specimen, used in the master curve	°C
T_{trans}	Ductile-to-brittle transition temperature	°C
T_{CVxxJ}	Temperature where the C_V value equals xx J	°C
T_p	Peak temperature	°C
T_{px}	Peak temperature during cycle number x during weld thermal simulation	°C
v	Impact velocity	m/s
v_0	Initial impact velocity	m/s
W	Width of fracture specimen	mm
x	Distance from fusion line during welding	mm

Greek Letters

δ	CTOD	mm
Δa	Increase in crack length	mm
$\Delta t_{6/4}$	Cooling time between 600°C and 400°C	s
$\Delta t_{8/5}$	Cooling time between 800°C and 500°C	s
ϵ	Strain	-
λ	Constant in J-CTOD correlation	
ρ	Root radius	mm
σ	Applied stress	MPa
$\sigma_{1,2,3}$	Principal stresses	MPa
σ_f	Fracture strength	MPa
σ_M	Von Mises stress	MPa
σ_{UTS}	Ultimate tensile strength	MPa
σ_Y	Yield strength	MPa
σ_{yy}	Stresses in the y direction parallel to the xz-plane	MPa
ν	Poissons ratio	-

Referenced Standards

Short name	Title
ASTM A992	ASTM Standard A992/A992M – 11: Standard Specification for Structural Steel Shapes
ASTM E23	American Society for Testing and Materials (ASTM) Standard E23 – 12c: Standard Test Methods for Notched Bar Impact Testing of Metallic Materials
ASTM E399	American Society for Testing and Materials (ASTM) Standard E399: Standard Test Method for Linear-Elastic Plane-Strain Fracture Toughness K_{Ic} of Metallic Materials
ASTM E1820	American Society for Testing and Materials (ASTM) Standard E1820 – 11Test: Method for Measurement of Fracture Toughness
ASTM E1921	American Society for Testing and Materials (ASTM) Standard E1921-13a Standard Test Method for Determination of Reference Temperature, T_0 , for Ferritic Steels in the Transition Range
BS7448	British Standard (BS) 7448-1:1991 Fracture mechanics toughness tests – Part 1: Method for determination of K_{Ic} , critical CTOD and critical J values of metallic materials
BS7910	British Standard (BS) 7910:2005: Guide to Methods for Assessing the Acceptability of Flaws in Metallic Structures
ISO14556	International Standardisation Organisation (ISO) Standard EN ISO 14556:2000 – Steel – Charpy V-notch pendulum impact test. Instrumented test method
ISO19902	International Standardisation Organisation (ISO) Standard EN ISO 19902:2007 – Petroleum and natural gas industries–Fixed steel offshore structures

Contents

Preface	I
Abstract	III
Sammendrag	VII
List of Acronyms	XI
Nomenclature	XIII
1 Introduction	1
1.1 The Arctic Materials Project	1
1.2 Motivation	2
1.3 Aim of this Work	4
2 Theoretical Background	5
2.1 HSLA Steels	5
2.2 Phase Transformations in Steels	6
2.3 Equilibrium Phases of Steel and the Austenite-Ferrite Transformation	7
2.3.1 Austenite and Ferrite	8
2.4 Metastable Phases of Steel	9
2.4.1 Martensite	9
2.4.2 Bainite	10
2.4.3 Acicular Ferrite	12
2.4.4 Widmanstätten Ferrite	13
2.5 Fracture	14
2.5.1 Fracture Mechanics	14
2.5.2 Fracture Behaviour	14
2.5.3 Fracture Toughness	18
2.5.4 Applicability to Structures	21
2.6 Welding of HSLA Steels	22
2.6.1 Weldability	22
2.6.2 Weld Zones	23
2.6.3 The Heat Affected Zone Formed During Single-Pass Welding	25
2.6.4 The Heat Affected Zone Formed During Multi-Pass Welding	26
2.7 Local Brittle Zones	28
2.7.1 The MA Region	28
2.7.2 Toughness in the CGHAZ and ICCGAZ	30
2.7.3 Fracture Associated With Local Brittle Zones	30

2.8	Fracture Toughness Testing	33
2.8.1	The CTOD Test	34
2.8.2	Fracture Toughness Testing and the Charpy Notched Impact Test	36
2.9	The Charpy Notched Impact Test	38
2.9.1	The Charpy Specimen	38
2.9.2	Charpy Test Data and Procedure	39
2.9.3	Charpy Data Report Methods	40
2.9.4	Stress State	40
2.9.5	The Instrumented Charpy Test	41
2.9.6	Fatigue Pre-Cracked Charpy Specimens and Measured Energy	42
2.10	Fracture Testing of the HAZ	44
2.11	Weld Thermal Simulation	45
2.12	Crack Arrest	46
3	Previous Work	49
3.1	Physical Differences Between the Charpy Impact Test and Quasi-Static Fracture Mechanical Tests	51
3.1.1	Specimen Size	51
3.1.2	Flaw Geometry	52
3.1.3	Strain Rate	53
3.1.4	Event Described During Testing	54
3.1.5	Level of Constraint	54
3.2	Charpy and Quasi-Static Fracture Mechanical Test Correlations	55
3.2.1	Correlations for Welded Materials	57
3.3	Scatter in Fracture Toughness Measurements Related to Fracture Mechanism	58
3.4	Results From Instrumented Charpy Testing	59
3.4.1	Transition Curves	59
3.4.2	Curve Classes Obtained During Instrumented Charpy Testing	60
3.5	Fracture Surface Investigation	65
4	Materials and Experimental Procedures	67
4.1	Material	67
4.2	Weld Simulation	67
4.3	Instrumented Charpy Impact Testing	69
4.4	Transition Curves	72
4.5	CTOD Testing	73
4.6	Microstructural Investigation	74
4.6.1	Moulding and Specimen Preparation	74
4.6.2	Etching	75
4.6.3	Imaging	76
4.7	Fracture Surface Investigation	77
4.8	Correlations Used to Estimate CTOD Values from Data Obtained During Charpy testing	78
4.8.1	Lower Bound Relation for Lower Shelf and Lower Transitional Behaviour According to BS7910	79
4.8.2	Lower Shelf Transitional Behaviour Based on the Master Curve	80
4.8.3	Validity limits	82
4.8.4	Procedure to Convert Fracture Toughness to CTOD	82

4.8.5	Procedure and Parameters Used in Evaluating the Degree of Correlation of the two Investigated Methods	83
5	Results	85
5.1	Estimated Carbon Equivalent	85
5.2	Results from Instrumented Charpy Testing	86
5.3	Transition Curves From Instrumented Charpy Test Data	87
5.4	Charpy Energies and Curve Classes	90
5.4.1	Charpy Energies Absorbed Before Maximum Load and Brittle Fracture Initiation	90
5.4.2	Charpy Energy Fractions	94
5.5	Results From CTOD Testing	100
5.6	Results From Fracture Surface Investigations	101
5.6.1	CGHAZ, V-notched tested at -30°C	102
5.6.2	CGHAZ, V-notched tested at -60°C	103
5.6.3	CGHAZ, pre-cracked tested at 0°C	104
5.6.4	CGHAZ, pre-cracked tested at -30°C	105
5.6.5	ICCGHAZ, V-notched tested at -30°C	106
5.6.6	ICCGHAZ, V-notched tested at -60°C	107
5.6.7	ICCGHAZ, pre-cracked tested at 0°C	108
5.6.8	ICCGHAZ, pre-cracked tested at -30°C	109
5.6.9	ICCGHAZ, pre-cracked tested at -60°C	110
5.7	Results From Microstructural Investigations	111
5.8	Results From Using CTOD Correlations	115
5.8.1	Lower Bound Relation after BS7910	115
5.8.2	The Master Curve Approach	117
6	Discussion of Results	123
6.1	Transition Curves	123
6.1.1	Effect of Changes in Microstructure	123
6.1.2	Effect of Notch Geometry	126
6.1.3	Data Scatter	127
6.2	Fracture Surfaces	129
6.3	Microstructure	131
6.4	Results and Parameters Obtained from Instrumented Charpy Tests	133
6.4.1	Challenges in Curve Class Determination	133
6.4.2	Distribution of Energies Measured to Maximum Load and Load to Brittle Fracture Initiation With Temperature	135
6.5	Change in Energy Fractions with Curve Class	137
6.6	Change in Energy Fractions with Temperature	139
6.6.1	The Relation Between SEM Results, Energy Fractions and Curve Classes	140
6.7	Correlations Used to Relate Charpy Data and Quasi Statical Fracture Mechanical Parameters	142
6.7.1	Degree of Correlation of the Lower Bound Relation After BS7910	143
6.7.2	Degree of Correlation of the Master Curve	144
6.7.3	Comparison of the Lower Bound Relation After BS7910 and the Master Curve Correlation	150

6.7.4	Use of Instrumented Charpy Test Data in Obtaining Fracture Mechanical Parameters	151
7	Conclusions	153
8	Suggestions for Further Work	157
	Bibliography	159
	Appendices	167
A	Data From Instrumented Charpy Testing	169
A.1	All Data From Charpy Testing of V-notched Base Material	170
A.2	All Data From Charpy Testing of pre-cracked Base Material	171
A.3	All Data From Charpy Testing of V-notched CGHAZ	172
A.4	All Data From Charpy Testing of pre-cracked CGHAZ	173
A.5	All Data From Charpy Testing of V-notched ICCGHAZ	174
A.6	All Data From Charpy Testing of pre-cracked ICCGHAZ	175
B	Data From CTOD Testing	177
B.1	CTOD Testing of CGHAZ	178
B.2	CTOD Testing of ICCGHAZ	179
C	Curves From Instrumented Charpy Testing	181
C.1	Base material V-notched	182
C.2	Base Material pre-cracked	185
C.3	CGHAZ V-notched	189
C.4	CGHAZ pre-cracked	193
C.5	ICCGHAZ V-notched	196
C.6	ICCGHAZ pre-cracked	198
D	Formal Problem Formulation	201
E	Risk Evaluation	205
	List of Figures	211
	List of Tables	215

1 Introduction

1.1 The Arctic Materials Project

It is believed that about 13 % of the planet's undiscovered oil reserves, 30 % of the undiscovered natural gas reserves and 20 % of the undiscovered natural gas liquids reserves are located in the Arctic region. This represents about 22 % of all undiscovered and technically recoverable oil and gas resources in the world [1–5]. The Arctic region is associated with harsh climate conditions, long distances and poor infrastructure, making operations challenging to carry out.

To explore and extract oil and gas in this region, proper materials selection is important, and materials solutions to be used in the Arctic regions can be expensive as the materials are required to survive the harsh climate conditions over acceptable durations of time as well as light weight solutions being necessary. In addition, the lack of standards to be used in qualifying structural materials to be used in the Arctic region also makes materials selection challenging.

This master's thesis has been written in close cooperation with the Arctic Materials Project, a competence project for the industry and commerce supported by the The Research Council of Norway (RCN) via the Fundamental Studies of Materials' behaviour for future Cold Climate applications (SMACC) project. Four oil and gas companies, four engineering companies and six material suppliers are involved, including SINTEF, The Norwegian University of Science and Technology (NTNU) and DNV GL that has been closely involved in the present master's thesis.

The objective of the Arctic Materials Project is to establish criteria and solutions for safe and cost-effective applications of materials used in hydrocarbon exploration and production in Arctic regions. The project focuses on the use of high strength steel for

applications at temperatures down to $-60\text{ }^{\circ}\text{C}$, and on extending the application range for structural steels by characterizing brittle fracture resistance in welded steel structures, where also local variations of materials properties are of interest [6]. The project also has activities towards polymer materials and aluminium.



Figure 1.1: Map of resource basins in the Arctic Circle region [7].

1.2 Motivation

High Strength Low Alloy (HSLA) steels are designed for use in low temperature applications due to their good combination of strength and toughness. Toughness is of special interest when investigating steels for low temperature applications, where sudden fracture can be a problem, as the toughness of steels may decrease at low temperatures, as the operational temperatures often lie below the transition temperature. This leads to brittle failures being frequently observed at low temperatures.

Although HSLA steels generally provide a good combination of strength and toughness, they may also exhibit local brittle zones associated with local variations in microstructure, often as a result of the welding and production methods performed. Existence of local

brittle zones can have detrimental results on the toughness of steels, especially in the heat-affected zones (HAZs) formed during welding. Previous work has indicated that fracture initiation can be linked to certain microstructural phases in different weld zones. In this regard, it is of interest to investigate the microstructural features associated with brittle fracture at low temperatures in addition to fracture initiation sites in the weld zones of the candidate steel intended to be used in Arctic applications.

The Charpy V-notch impact test is usually required as a part of the procedure when qualifying weldments of structural steels. The Charpy test is usually used for qualification and ranking purposes as it is simple, cheap and with a long history of applications, as it has been used successively for decades. Moreover, using the Charpy impact test to estimate material fracture toughness is important in material specification, where Charpy values are used to establish design requirements for metals at minimum service temperatures to meet satisfactory safety levels. These requirements are often having a sufficiently high Charpy energy or a transition temperature well above the service temperature. An example of material requirements given by ISO 19902 can be seen in Figure 1.2 [8].

Material thickness mm	Steel toughness class				
	NT	CV1		CV2/CV2Z/CV2ZX	
	SMYS \leq 400 MPa Group I and II	SMYS \leq 400 MPa Group I and II	SMYS $>$ 400 MPa Group III	SMYS \leq 400 MPa Group I and II	SMYS $>$ 400 MPa Group III, IV and V ^b
$t \leq 12$ ($t \leq 0,5$ in)	LAST +10 °C (LAST +18 °F)	LAST +10 °C (LAST +18 °F)	LAST +10 °C (LAST +18 °F)	LAST +10 °C (LAST +18 °F)	LAST -10 °C (LAST -18 °F)
$12 < t < 25$ ($0,5$ in $< t < 1,0$ in)	LAST +10 °C (LAST +18 °F)	LAST +10 °C (LAST +18 °F)	LAST -10 °C (LAST -18 °F)	LAST -10 °C (LAST -18 °F)	LAST -30 °C (LAST -54 °F)
$25 \leq t < 50$ ($1,0$ in $\leq t < 2,0$ in)	LAST -10 °C (LAST -18 °F)	LAST -10 °C (LAST -18 °F)	LAST -30 °C (LAST -54 °F)	LAST -30 °C (LAST -54 °F)	LAST -30 °C (LAST -54 °F)
$t \geq 50$ ($t \geq 2,0$ in)	Combination not allowed	LAST -30 °C (LAST -54 °F)	LAST -30 °C (LAST -54 °F)	LAST -30 °C (LAST -54 °F)	LAST -30 °C (LAST -54 °F)
Energy requirement ^a	27 J (20 ft-lbs)	27 J (20 ft-lbs)	40 J (30 ft-lbs)	34 J (25 ft-lbs)	40 J (30 ft-lbs)
^a No individual specimen test value shall be less than 70 % of the minimum average value described in this table.					
^b Higher energy should be considered for group IV and V used in DC1 applications.					

Figure 1.2: Table F.1 from ISO1992 [8] showing minimum weld metal HAZ Charpy energy and temperature (Lowest Anticipated Service Temperature (LAST)) requirements for steel. The table is divided according to different design classes with varying SMYS.

The current trend in the industry is to employ more sophisticated fracture toughness test methods, like the quasi-static CTOD test, since the industry needs to be more conservative when assessing new criteria for steels of higher strength and thicker sections. It has been anticipated that Charpy tests performed with a sharp pre-crack could provide information about the implications of the circular notch commonly used in Charpy specimens as well as provide knowledge about the comparability to fracture mechanical tests. Pre-cracking is commonly not used, as it is associated with higher costs and requires more work to machine the specimens. The notch sharpness may be of importance for the fracture toughness values obtained in the Charpy test, and is especially important to investigate in connection with testing of HAZs formed during welding. The widely varying microstructures formed in these zones influences the fracture toughness and brittle fracture susceptibility of the steel, and the notch geometry may be especially detrimental when measuring the fracture toughness of weldments.

1.3 Aim of this Work

The primary goal of this master's thesis has been to investigate low temperature toughness and crack initiation in structural steels. The work intends to study the microstructural features contributing to brittle fracture in steels intended for low temperature applications. Furthermore, the work intends to contribute to explore the importance of the difference in crack configuration, microstructure and physical differences that makes direct correlations between quasi-static fracture mechanical tests and the Charpy impact test difficult to obtain. This has been done to explore whether and how the instrumented Charpy test might serve as more than a quality control test in the future. Also, the work intends to take a closer look at correlations developed to estimate fracture mechanical parameters from Charpy data.

2 Theoretical Background

2.1 HSLA Steels

HSLA steels are commonly used in structural applications due to combined strength and toughness properties [9], with yield strengths, σ_Y , ranging from 250–590 MPa. These steels are accepted for use in low temperature applications due to their low Ductile-to-Brittle Transition Temperature (DBTT), down to -70°C [10, 11]. HSLA steels can be classified into four different categories: micro-alloyed steels with fine grained ferrite, acicular ferritic steels, bainitic steels and dual phase steels [11]. The aim of the development of HSLA steels has been to produce steels with high strength and toughness by refining the acicular ferrite microstructure by Thermo-Mechanically Controlled Processing (TMCP) [12].

HSLA steels generally derive their high strength properties by specific choice of alloying elements. Different alloying elements are added to the steel to increase the hardenability by retarding the formation rate of perlite and bainite, making the martensite transformation more competitive [13, 14]. The microstructure of the steel greatly affects the low-temperature mechanical properties of the alloy, the toughness especially [15].

HSLA steels can be produced with a fine ferrite grain structure, by using TMCP like controlled rolling in the austenite phase field (Figure 2.1). By controlling the rolling parameters i.e. temperature, strain, number of rolling passes and finishing temperature in addition to the chemical composition of the steels, the microstructure and hence the mechanical properties of the HSLA steels can be carefully modified [10].

Although HSLA steels are associated with good low temperature toughness properties, a drop in toughness in the Heat Affected Zone (HAZ) is generally found after welding, as the heat from the welding process results in a change in the microstructure including

the formation of Martensite-Austenite (MA)-phases especially at prior austenite grain boundaries and mixture of upper bainite and martensite, depending on the thermal cycles [16]. This also results in the DBTT being shifted to higher temperatures [17].

2.2 Phase Transformations in Steels

A variety of microstructures can be found in steels, depending on the thermo-mechanical procedure and alloying elements used. Different phases can be formed during a phase transition between equilibrium states, since the atoms can move in a variety of ways to achieve a change in crystal structure. Phase transformations can be either reconstructive, where bonds are broken and atoms are rearranged into an alternative pattern, or displacive, also called shear transformations, where the original atomic pattern is homogeneously deformed into a new crystal structure [10, 11].

During a shear transformation, the change in crystal structure also changes the macroscopic shape of the material, which in turn introduces elastic and plastic stresses in the surrounding matrix. Therefore, the product phase tends to grow in the form of thin plates that minimize the strains during displacive transformations. Furthermore, atoms are moved in a coordinated motion, and therefore displacive transformations do not require diffusion [10, 11].

Reconstructive transformations, on the other hand, involve diffusion. The atomic mobility is sufficient to avoid shape deformation and shear components, although the volume may change. Since diffusion processes can occur, substitutional solute atoms may also redistribute between phases during reconstructive phase transformations [10, 11].

2.3 Equilibrium Phases of Steel and the Austenite-Ferrite Transformation

The equilibrium phases of steel include ferrite, austenite and cementite. Austenite is the stable phase of low carbon steels at high temperatures, while α -ferrite (low temperature ferrite), cementite and pearlite, a two-plate intergrowth structure of α -ferrite and cementite (Fe_3C), are the equilibrium phases at temperatures below the eutectoid temperature. During eutectoid decomposition, the austenite phase generates a lamellar product of alpha ferrite and cementite known as pearlite because of its "mother-of-pearl" appearance under the light microscope. These equilibrium phases are formed in a reconstructive manner, where diffusion of atoms occurs during nucleation and growth.

According to the Fe-C phase diagram, shown in Figure 2.1, the transformation from austenite to ferrite occur in the temperature range between the A_1 and A_3 temperatures at equilibrium (often denoted A_{e1} and A_{e3}). Phases of steel generated by the decomposition of austenite by a reconstructive mechanism include allotriomorphic ferrite, idiomorphic ferrite, massive ferrite and pearlite [10]

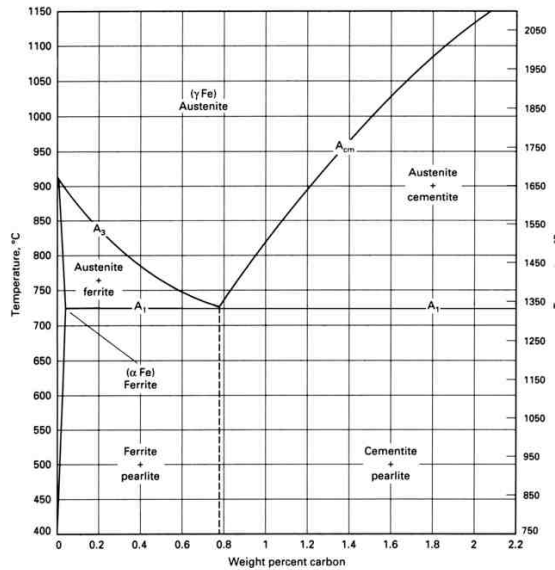


Figure 2.1: The iron-carbon phase diagram for low carbon contents[18].

2.3.1 Austenite and Ferrite

Austenite has a Face Centered Cubic (FCC) crystal structure, while ferrite has a Body Centered Cubic (BCC) structure. This is essential for understanding transformation behavior and when investigating phases formed during heat treatment. As the FCC structure has larger interstitial positions compared to the BCC structure, austenite has a higher solubility of carbon than ferrite [13].

Austenite can dissolve up to 2.14 wt% carbon, while the solubility of carbon is 0.022 wt% in ferrite [13], determined by the phase diagram (Figure 2.1). The transformation from austenite to ferrite is accompanied by an atomic volume change of approximately 1% [10]. The rate of the austenite transformation is proportional to the degree of under-cooling up to a certain point, where the reaction is limited by slow diffusivity of the controlling element, which may be carbon in the case of plain carbon steels.

The Morphologies of Ferrite

Ferrite can exist in one of the four morphologies [10]:

- *Grain boundary allotriomorphs* nucleate at the austenite grain surfaces and forms layers following the grain boundaries.
- *Widmanstätten ferrite plates or laths* grow along well-defined planes in the austenite structure, and do not grow across grain boundaries.
- *Intergranular idiomorphs* nucleate inside the austenite grains on non-metallic inclusions, and grow as equiaxed crystals.
- *Intergranular plates* nucleate within the austenite grains, and resemble the plates growing from the austenite grain boundaries.

The various morphologies formed during the cementite transformation at lower temperatures are similar to the ones formed during the ferrite transformation [10].

2.4 Metastable Phases of Steel

The conditions under which the decomposition from austenite occur are very important influences on the microstructure formed during heat-treatment of steels. When steels are subjected to high cooling rates, the transformation from austenite occurs at temperatures below the equilibrium transformation temperatures A_{e1} and A_{e2} . The non-equilibrium temperatures are often termed A_{c1} and A_{c3} . Transformations at high cooling rates lead to the formation of metastable phases, where the degree of under-cooling influences the final microstructure.

Metastable phases are formed in a large measure by displacive transformation mechanisms with little to no substitutional diffusion occurs during the transformation process, and some of these phases can be described as invariant-plane strain shape deformations with large shear components. Phases of steel generated by the decomposition of austenite by a displacive mechanism include Widmanstätten ferrite, ferrite and cementite in the morphology known as bainite, acicular ferrite and martensite [10].

2.4.1 Martensite

Martensite is a non-equilibrium phase with a plate- or needle-like appearance. The martensite transformation is a diffusion-less process, both during nucleation and growth, and occurs when austenitic steels are cooled rapid enough to prevent diffusion of carbon [13]. The transformation begins at a specific temperature, M_s , and ends at a temperature, M_f , where M_f is often defined as the temperature where the fraction of martensite equals 95%. The M_s and M_f temperatures are independent of cooling rate and are characteristic for a given alloy. They are both seen to decrease with increasing carbon content The amount of martensite that is formed is dependent on the degree of undercooling below M_s [19].

The transformation of austenite to martensite is characterized by a shear deformation, where the FCC lattice cell of austenite is deformed into a tetragonal Body Centered Tetragonal (BCT) lattice. During the transformation, the atoms moves in an organized manner and do not change positions. This provides coherency with the martensite and the initial phases [19]. The BCT structure of martensite forms because carbon diffusion is

restricted. It begins as super-saturated solid solution structure of ferrite, where the BCT lattice results when a BCC lattice is elongated along one of its axes. As a result, the carbon solubility is higher in martensite than in ferrite. The resulting lattice distortion also induces a high dislocation density, making martensite hard and strong, but also brittle[13]. Also, the metastable nature of the martensite results in rapid transformation to other equilibrium phases if the steel is re-heated or deformed.

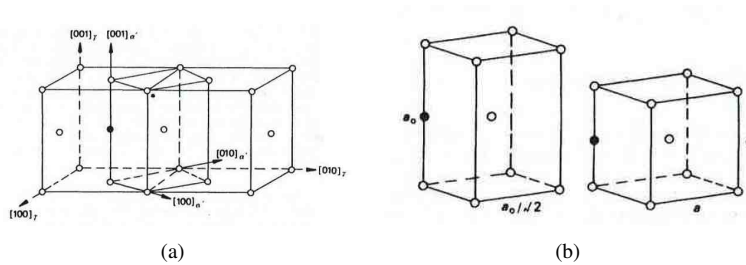


Figure 2.2: The BCT lattice shown in relation to the FCC and BCC lattices [10]. α and γ are commonly used symbols for ferrite and austenite respectively.

2.4.2 Bainite

Bainite is another microstructural morphology exhibited by steel, consisting of a mixture of α -ferrite and cementite phases [13]. The bainite product forms as needles or plates, depending on the degree of under-cooling during the transformation from austenite. The lower the temperature, the finer the resulting dispersion of the two phases becomes. The transformation occurs at temperatures above the M_s but below the temperature range where the pearlite reaction occurs, as illustrated in the Isothermal Temperature (IT) diagram in Figure 2.3.

The bainite transformation and the bainite structure exhibit features of both the pearlite transformation and the diffusion-less martensite transformation [19], as the bainite formation occurs with carbon diffusion during para-equilibrium nucleation, and little to no diffusion during growth [10]. Pure pearlite and bainite are competing reactions, where one structure cannot transform to the other after the transformation is completed, without reheating to and cooling from the austenite phase field [13].

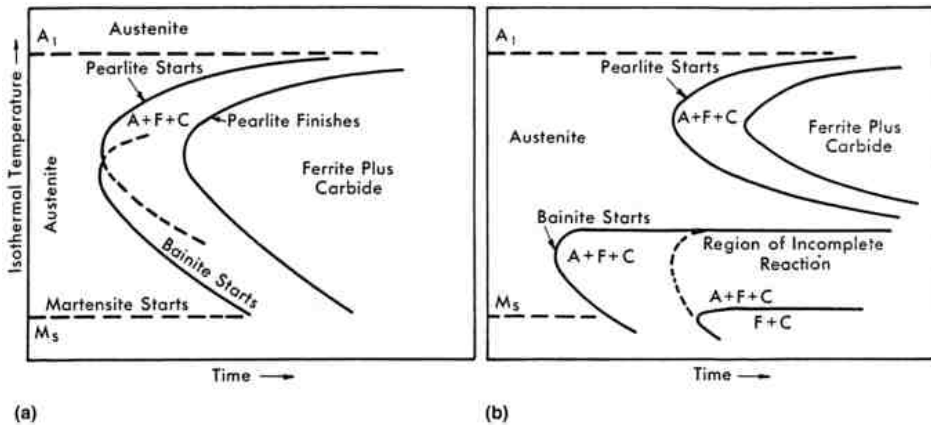


Figure 2.3: Isothermal transformation diagram for steel. a) Overlapping pearlite and bainite transformation common in plain carbon steels and b) separated pearlite and bainite transformation [18].

The bainite structure nucleates at austenite grain boundaries and is commonly divided into upper and lower bainite, depending on the temperature of which it was formed [10]. Upper bainite is formed at higher temperatures, where carbon is allowed to diffuse and carbides precipitate between the ferrite plates. Lower bainite is formed at lower temperatures, where diffusion of carbon is further suppressed. Therefore, some of the carbide can be found as precipitates within the ferrite, so that less carbide is precipitated between the plates.

Lower bainite tends to be harder and tougher than upper bainite, as the overall morphology is much finer in character, resulting in greater resistance to dislocation motion, in addition to the carbides precipitating within the plates [10, 11], which enables more residual toughness than when the carbides are distributed at the interfaces only.

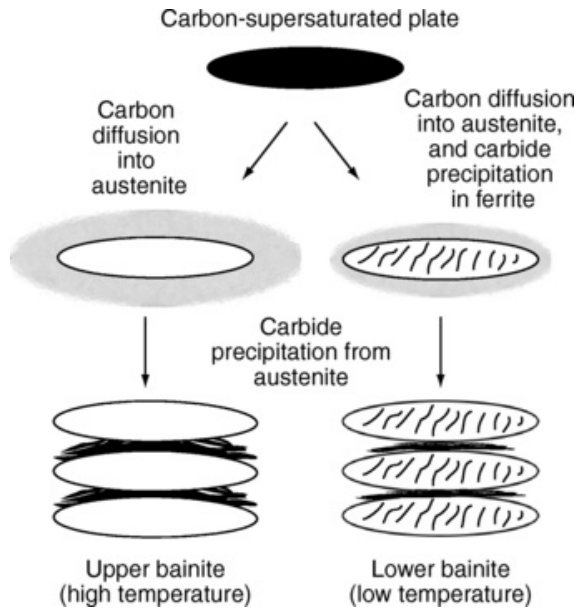


Figure 2.4: Transformation paths to upper and lower bainite structures [18, 20].

2.4.3 Acicular Ferrite

Acicular ferrite has nearly the same transformation mechanism as bainite, but nucleates at heterogeneities present in the material, rather than at the grain boundaries. The acicular ferrite plates nucleate on metallic inclusions and radiate in many different directions from the point-nucleation sites. Such plates usually do not grow across austenite grain boundaries, due to the large shear component associated with the transformation. The acicular ferrite phase grows with very short-range diffusion, causing excess carbon in the supersaturated ferrite matrix to be partitioned into the retained austenite after growth.

Acicular ferrite provides good mechanical properties, especially toughness, and is believed to be effective in deflecting propagating cleavage cracks due to the many different grain orientations present in the acicular ferrite phase. Therefore, it is often a desirable microstructure [10]. The transformation from austenite to acicular ferrite and bainite are competing reactions, depending on the amount of non-metallic inclusions present in the material.

2.4.4 Widmanstätten Ferrite

Widmanstätten ferrite occurs with carbon diffusion during para-equilibrium nucleation and growth [10], and forms at lower under-cooling than bainite, either by inter- and intergranular nucleation, after very long ageing times. Primary and secondary Widmanstätten ferrite may also form intragranularly at inclusions, making the acicular ferrite and Widmanstätten ferrite formation reactions competitive.

Widmanstätten ferrite can easily be confused with bainite and when performing microstructural classification, bainite and Widmanstätten ferrite are classified as ferrite side plates due to their similarities [21].

2.5 Fracture

2.5.1 Fracture Mechanics

Fracture mechanics is the study of materials with "pre-existing flaws", and can be used to predict structural failures due to the many cracks and flaws that are commonly found in all engineering materials. The field of fracture mechanics is important in structural design and materials selection, as it allows for estimation of a critical flaw size in a given material at a specific temperature and applied stress level [22], or a critical load size or critical material properties if the crack size in addition to material or critical load is given, respectively.

Fracture mechanics can generally be divided into Linear Elastic Fracture Mechanics (LEFM) and Elastic Plastic Fracture Mechanics (EPFM). In LEFM, the material deforms elastically and Small Scale Yielding (SSY) applies, i.e. the plastic zone in front of a crack tip is assumed to be smaller than any other characteristic dimension. Test specimens must be large for LEFM conditions to apply, and to ensure test reproducibility. In EPFM, the plastic zone in front of a crack tip is allowed to be much larger compared to the case when LEFM applies, and the the EPFM theory accounts for plastic deformation in the regions close to the crack tip. Due to the different conditions near the crack tip, distinctive fracture parameters are used to describe fracture events in the LEFM and EPFM regimes [23]. If SSY applies, EPFM and LEFM are related and provides equivalent results.

2.5.2 Fracture Behaviour

There are generally two possible fracture modes for engineering materials that can lead to failure: ductile and brittle fracture. A mix of the two can be found within the Ductile-to-Brittle Transition (DBT) region. Whether a material is ductile or brittle is governed by the ability of the material to initiate and sustain plastic deformation [13]. Under special circumstances, cracks can form and propagate along grain boundaries [23]. This type of fracture is called intergranular fracture, and is not presented further.

Brittle Fracture

Brittle fracture is often associated with rapid crack propagation occurring after very little plastic deformation in the area close to the fracture [15] and low energy absorption. Brittle fracture may occur without any prior warning and leads to severe structural damage. Since the material does not experience any stable crack growth before fracture occurs, brittle fracture is characterized as unstable, which means that the elastic energy stored in a structure can be enough to drive fracture.

The fracture mode of brittle materials is characterized as cleavage fracture. Fracture occurs trans-granularly in a crystallographic manner along planes of low indices and with low packing density [10, 13, 23]. Brittle fracture and low deformability can be associated with the absence of dislocations or immobile dislocations [11], and is often said to be stress controlled, as it occurs when a critical fracture stress is achieved ahead of the crack tip [24].

The fracture process can be divided into the processes of crack initiation and crack propagation [23]. Cleavage initiation involves the formation of a micro crack, often at material inhomogeneities and inclusions, like second-phase particles, pores, oxides and other defects introduced e.g. after welding, or by dislocation interaction, such as dislocation pile-ups at grain boundaries. Inhomogeneities act as stress raisers, and can give rise to a stress concentration high enough to initiate cleavage fracture when present in a material. A micro crack can also form by debonding between a particle and the surrounding matrix [25]. After a crack has been initiated, crack propagation may occur spontaneously without an increase in the applied stress level [13, 26].

Crack propagation by cleavage is influenced by the crystallographic orientation of neighbouring grains, as the crack may continue to grow into the neighbouring grain or arrest, depending on the grain orientation and available slip systems. Propagation can be described as the continuous breaking of bonds between atoms along specific crystallographic planes, where the local stress must be higher than the cohesive strength of the material. Therefore, planes with low packing density are often preferred, as fewer bonds have to be broken in order for fracture to occur. In BCC materials like ferritic steels, cleavage occurs on $\{100\}$ planes [23].

Brittle fracture can be described in terms of a weakest link model, where the probability of fracture follows a three-parameter Weibull distribution. Fracture is a result of finding a local critical defect large enough to exceed the material bond strength ahead of a crack tip, so the fracture probability depends on the sample volume of material in front of a crack [27].

Brittle fracture initiation often occur suddenly with a clear crack initiation point, leading to a sudden drop in load during mechanical testing. Therefore, it is possible to achieve a point measurement of the toughness during fracture mechanical testing of brittle materials [28].

A brittle fracture surface appears planar and faceted [15, 24, 29]. The fracture surface is often decorated with river patterns on a microscopic level. The river patterns indicate the direction of crack propagation [30], starting from the point of crack initiation.

Ductile Fracture

Ductile fracture, or shear fracture, occurs after substantial plastic deformation and high-energy absorption, and is associated with significant dimpling across the fracture interface, indicative of substantive plasticity [10]. As the fracture process in ductile materials proceeds relatively slowly, and yielding occurs prior to fracture, cracks present in ductile materials can be said to be more stable compared to cracks present in brittle materials. This is due to the fact that ductile fracture can be associated with mobile dislocations that allow for plastic deformation and blunting of a potentially harmful sharp crack to occur [11, 23].

As a result of mobile dislocations, yielding occurs prior to final fracture and abrupt failure, as would occur in brittle materials, is hindered. Ductile fracture is often said to be strain controlled and occurs when a critical fracture strain is obtained ahead of the crack tip [24].

Three distinct processes are often used to describe ductile fracture, associated with the nucleation, growth and coalescence of micro-voids. Ductile fracture is often initiated at second-phase particles, and the process is controlled by a combination of stress and strains acting on the particles [10, 26]. Voids are formed by cracking of particles or by de-cohesion at the particle matrix interface. Void growth is governed by strain and the hydrostatic stress component, while the fracture process is controlled mainly by a critical fracture strain during micro-void coalescence.

For ductile materials, the fracture surface has a rougher appearance than brittle fracture surfaces on a macroscopic level [29], while the fracture surface consists of numerous spherical dimples on a microscopic level [10, 30].

The Ductile-Brittle Transition

Certain materials, like BCC metals, experience a DBT when the temperature is lowered, where the fracture toughness of the material decreases rapidly over a limited temperature range as shown in Figure 2.5. Above a certain transition temperature, T_{trans} , the material fails by a ductile fracture mechanism, while the fracture mechanism changes to brittle cleavage fracture below T_{trans} . Generally, a low T_{trans} is desired [11] in order to prevent brittle fracture from occurring at the service temperature, and to allow for some yielding before the onset of brittle fracture.

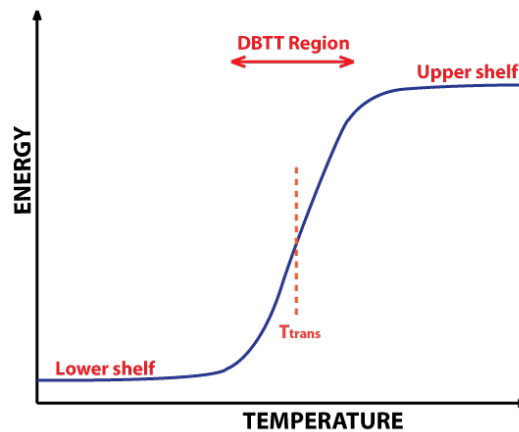


Figure 2.5: Schematic representation of a typical transition curve.

In the DBT region, fracture may occur by a brittle and ductile fracture mechanism in the same specimen. In the lower transition region, the fracture mechanism is pure cleavage, but when the temperature is increased and cleavage becomes more difficult, ductile fracture governs the fracture process, resulting in increasing toughness. In the upper transition region, crack initiation occurs by ductile micro-void coalescence, while final fracture occurs by cleavage after the crack has sampled enough material ahead of the crack tip to contain a critical flaw. Thus, the fracture toughness in the transition region depends on statistical sampling effects, which often leads to scattered data [23].

As outlined above, ferritic steels have a BCC structure, while austenitic steels have a FCC structure[10]. At low temperatures, BCC metals normally fail by cleavage fracture as the number of active slip systems (12 at room temperature) is limited. FCC materials usually do not fracture by cleavage due their 12 slip systems being less influenced by temperature variations. Therefore, FCC metals do not show a DBT behaviour like BCC metals, as the number of active slip systems is not as dependent on temperature [23].

The occurrence of a DBT can also be explained in terms of the temperature dependent Peierls stress, which is the force required to move a dislocation through a crystal lattice in a particular direction [31], and can be thought of as lattice friction. BCC metals have different conditions for plasticity compared with FCC metals because the Peierls stress is higher, making cross-slip for the slower screw dislocations easier. The dislocations in BCC metals are known to move more slowly in the crystalline lattice due to the higher Peierls stress, and the addition of the cross-slip mechanism increases the probability of forming dislocation networks, making dislocations immobile. Above a certain temperature, the Peierls stress for BCC metals becomes small, allowing screw dislocations to glide much easier [32], making the material more ductile.

As fracture in the DBT region is an intermediate case between ductile and brittle fracture, a specimen will fracture after a moderate amount of deformation and has a part crystalline and part fibrous surface appearance [29].

2.5.3 Fracture Toughness

Fracture toughness is a material's resistance to fracture, most often measured as the energy per area fracture surface. It can also be denoted in terms of a critical value of a crack driving force required to initiate a crack or propagate a crack already present in the material. Critical values of the stress intensity, K , the strain energy release rate, G , or the non-LEFM J-integral are parameters commonly used to express fracture toughness [33]. The Crack Tip Opening Displacement (CTOD) is also a commonly used fracture parameter. As high toughness materials are often desired for engineering purposes, this property is of utmost importance for many engineering applications, and is for this reason used as a standard for structural design and materials selection[22].

Fracture Toughness and Material Strength

Structural materials generally need to be both strong and tough. However, the properties of strength and toughness can be mutually exclusive properties in many engineering materials [33]. Strength is generally defined as resistance to plastic deformation, and comes in three variants: yield strength, σ_Y , ultimate tensile strength, σ_{UTS} , and fracture strength, σ_f . The yield strength and tensile strength of materials tend to be temperature dependent, generally decreasing as the temperature is increased. This affects the load bearing capacity of a material, which usually decreases with decreasing strength [26]. A high toughness is achieved by an optimum combination of strength and ductility.

The fracture toughness, or the energy to fracture, can be estimated from the area under the stress-strain curve during a tensile test under slow loading conditions according to Equation (2.1) [30]. More strain energy is required to induce ductile fracture than to induce brittle fracture, hence ductile materials are generally tougher.

$$\frac{Energy}{Volume} = \int_0^{\epsilon_f} \sigma d\epsilon \quad (2.1)$$

Toughness can therefore be said to represent the combination of strength and ductility. Very high-strength materials are often less ductile and have lower toughness than lower strength materials (Figure 2.6). Conversely, very ductile materials, such as polymers, have insufficient strength to be called "tough". This is also evident from looking at the relation between fracture toughness and stress in Equation (2.2) Some of the factors that influence the strength and fracture toughness of a material are temperature, which affects the dislocation mobility in a material, microstructural parameters such as grain size and inclusions, and the deformation and thermal history [11, 15]. At any given strength level, fine-grained metals and alloys generally possess significantly higher notched-bar impact properties than coarse-grained metals [15].

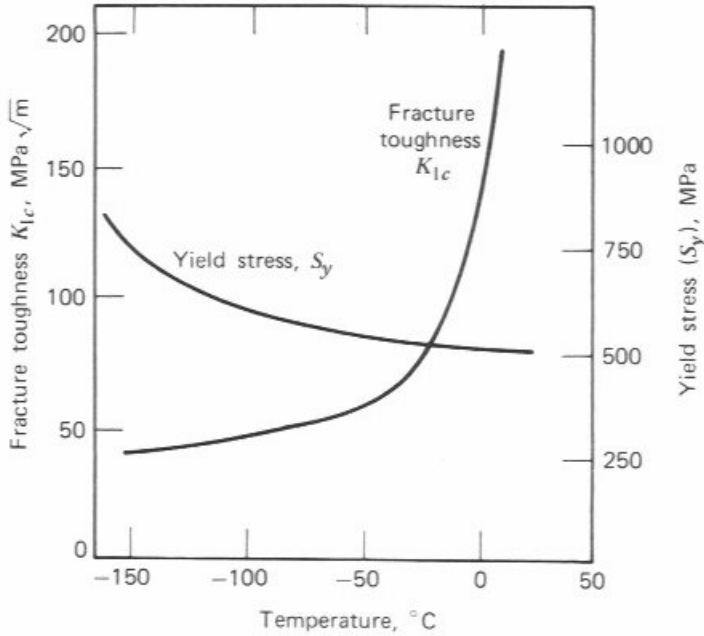


Figure 2.6: How strength and toughness varies with temperature [34].

Stress Intensity Factor and Fracture Toughness

Generally, brittle fracture is undesirable and steels are selected to prevent brittle fracture from occurring. Selection is based on design rules, where plastic yield is generally not allowed. A sufficient toughness is selected based on a LAST. In this regard, specified fracture toughness properties, usually based on the stress intensity factor, K , are used [26]. The stress intensity factor for mode I loading (in-plane-opening) is given by Equation (2.2) [24, 35].

$$K_I = \sigma \sqrt{\pi a} f\left(\frac{a}{W}\right) \quad (2.2)$$

The stress intensity factor can also be expressed as in Equation (2.3) where it is evident that K uniquely describes the stress field in front of a crack tip [23, 24].

$$K_I = \lim_{r \rightarrow 0} \sigma_Y \sqrt{2\pi r} \quad (2.3)$$

The stresses in front of a crack tip are determined by σ_Y and the strain hardening properties of a material [26]. Fracture of a material occurs at a critical stress intensity, K_{IC} .

K_{IC} is in that case a measure of the fracture resistance of a material in the LEFM regime and mode I loading, and is furthermore assumed to be a size-independent property [23]. It represents a lower bound toughness at a given temperature and rate of loading when measured in plane strain. In addition, the plastic zone size in front of the crack tip has to be small compared to the crack size, and to specimen dimensions [35, 36]. A valid K_{IC} cannot be obtained within the EPFM regime, as in the LEFM regime. In EPFM, critical values of CTOD or J are often used [22]. If small scale yielding applies, these parameters can be used to estimate K_{IC} .

2.5.4 Applicability to Structures

According to Anderson [23], one of the fundamental assumptions of fracture mechanics is that the fracture toughness, K_{IC} , is independent of size and geometry of the cracked body. This means that fracture toughness values obtained by using small test specimens should be applicable to large structures, provided that the tests are performed according to accepted standards, such as those specified by the ASTM and other professional organizations. Fracture toughness can be recognized as a standard for design and selection of materials since by knowing the value of K_{IC} for a given material; a critical crack length can be estimated at the operating temperature and stress state[22].

Although K_{IC} is generally assumed to be size independent, it can be discussed whether or not this is correct. According to Wallin [26], it is the specimen ligament size, not the thickness, that controls the fracture toughness value, and the plain-strain fracture toughness might therefore not represent a specimen size independent lower bound fracture toughness corresponding to a plane-strain stress state, as defined by ASTM.

2.6 Welding of HSLA Steels

During welding, the microstructure of the welded steel is changed, and many different microstructures can form in the HAZ depending on the thermal cycles during welding and the chemical composition of the steel [37]. This leads to a heterogeneous microstructure and variations in mechanical properties, like toughness [38–41]. The balance between high strength and toughness in HSLA steels can be influenced by thermal cycles experienced during welding, resulting in local poor toughness in the HAZ [12]. Welding can be done in a single pass, or in multiple passes. Multipass weld HAZs of structural steels exhibit a high level of heterogeneity, as the microstructure formed during the first weld pass is further altered [42].

2.6.1 Weldability

The weldability of steels is often expressed in terms of the Carbon Equivalent (CE), a measure of the hardenability of the steel i.e. how easily martensite is formed upon cooling of a given steel. The CE expresses the joint effect of addition of several alloying elements on the martensite transformation by weighing the presence of the alloying elements relative to that of carbon, as if the steel were to be a plain carbon steel. For low alloy steels, the CE can be calculated according to Equation (2.4), where the wt% of the alloying elements are used. For steels with a wt% carbon of more than 18%, the CE, then often called Parameter of Crack Measurement (PCM), or cold crack susceptibility, can, according to International Institute of Welding (IIW) be calculated by using Equation (2.4) [10, 43].

$$CE = C + \frac{Mn}{6} + \left(\frac{Cr + Mo + V}{5} \right) + \left(\frac{Ni + Cu}{15} \right) \quad [wt\%] \quad (2.4)$$

For steels with a carbon content lower than about 18 wt%, the PCM given by the Ito–Bessyo formula in Equation (2.5) provides a more realistic assessment of the weldability [10, 43, 44].

$$CE = C + \frac{Si}{30} + \left(\frac{Mn + Cr + Cu}{20} \right) + \frac{Ni}{60} + \frac{Mo}{15} + \frac{V}{10} + 5B \quad [wt\%] \quad (2.5)$$

A different formula is needed for steels with a lower carbon content as the kinetics of transformation are faster and increasing the alloy content does not affect the hardenability as much. Therefore, Equation (2.4) provides a smaller tolerance to the presence of substitutional alloying elements compared to Equation (2.5) [43]. The PCM formula is obtained for a wider range of steels compared to the CE formula given by IIW [45]. A high CE value is equivalent to a steel having high hardenability, and therefore, low CE values are desired for steels to be considered weldable. A steel is generally considered weldable if the CE of the steel is below 0.45 [43, 46], while the PCM should be less than 0.27% for plates with a thickness less than 45 mm [47], somewhat depending on the steel thickness and structure geometry [46].

2.6.2 Weld Zones

The welded joint can be divided into two main regions, the fusion zone and the HAZ. During welding, the material in the fusion zone is heated up to the melting point followed by rapid cooling. The HAZ represent those areas close to the weld where the microstructure changes without the steel melting [10]. A change in microstructure leads to different mechanical properties in the HAZ compared to the original base material. The HAZ is usually divided into several regions with different microstructural features

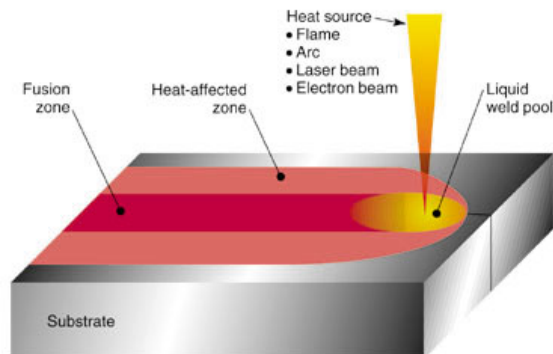


Figure 2.7: Fusion Zone and HAZ [48].

depending on the heat input experienced during one or several weld passes. The peak temperature, T_p , and cooling rate, often expressed as $\Delta t_{8/5}$, the time to cool the material from 800-500 °C, are important weld parameters that determines the final microstructure. T_p and the heating rate decreases with distance from the fusion boundary, while the

cooling rate, $\Delta t_{8/5}$ is less sensitive to this distance. The nature of the thermal cycle at a given position from the fusion line, x , within the HAZ is given by T_p and $\Delta t_{8/5}$. They both increase with the heat input, q , according to Equation (2.6) and (2.7), respectively [10], where the value of n is either 1 or 2 depending on the heat flow being two or three dimensional.

$$T_p \propto \frac{q}{x} \quad (2.6)$$

$$\Delta t_{8/5} \propto q^n \quad (2.7)$$

By knowing the T_p and the cooling rate, a Continuous Cooling Temperature (CCT) diagram for the given steel can be used to predict the final microstructure, like the one presented in Figure 2.8 for a HSLA 100 steel. Addition of alloying elements will influence the position of the ferrite and bainite noses, usually shifting the curves to longer times [14].

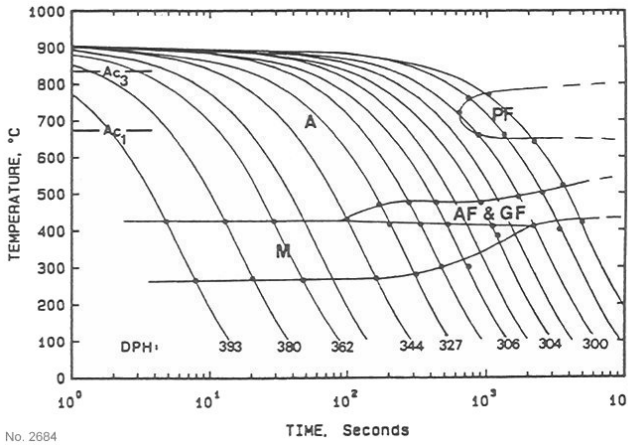


Figure 2.8: CCT diagram of HSLA 100 steel with composition 0.06% C, 0.83% Mn, 0.37% Si, 3.48% Ni, 0.58% Cr, 0.59% Mo, 1.66% Cu and 0.28% Nb given in wt % [49]. A = Austenite, AF = Acicular Ferrite, M = Martensite, GF = Granular Bainite, PF = Proeutectoid Ferrite, DPH = Diamond Pyramid Hardness.

2.6.3 The Heat Affected Zone Formed During Single-Pass Welding

The HAZ of a single-pass weld can be divided into four characteristic regions, depending on the T_p experienced during the weld thermal cycle: Coarse Grained Heat Affected Zone (CGHAZ), the Fine Grained HAZ (FGHAZ), the Intercritical HAZ (ICHAZ), and the Subcritical HAZ (SCHAZ) [50] (Figure 2.9). Figure 2.10 relates the T_p to the resulting zones and microstructures obtained in a weld after cooling to the phase diagram of steels.

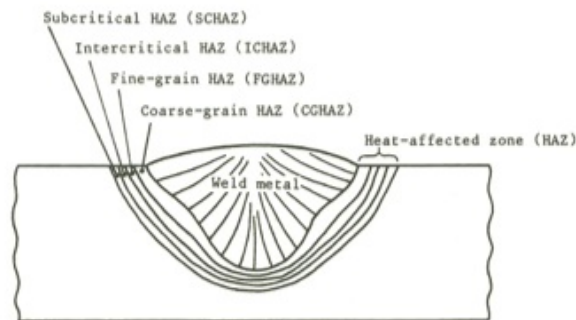


Figure 2.9: Illustration of the location of the different HAZ zones in a single pass weld [51].

The zone closest to the fusion line is heated above the A_3 temperature, where the microstructure fully transforms to austenite. This is the coarse grained HAZ, where the microstructure consists of large grained austenite due to annealing during heating beyond A_3 . During cooling, martensite and MA constituents may form here. As the distance from the fusion line increases, the grain size of the austenite decreases. This zone is often referred to as the fine-grained zone (FGHAZ), and usually exhibit good mechanical properties compared to the CGHAZ.

Further away from the fusion line, the microstructure is only partially transformed to austenite, as the T_p obtained in this region lies between the A_1 and A_3 temperatures. The austenite that forms here has a high carbon content, as the solubility of carbon in austenite increases with decreasing temperature. The parts of the HAZ that does not transform fully or partially to austenite are tempered [10, 42]. When the weld is cooled at high cooling rates, the CGHAZ consists of mainly martensite and bainite.

At lower cooling rates, MA-constituents may form and the microstructure typically consists of lower and upper bainite, MA-constituents and bainitic ferrite. With further decrease in cooling rate, the amount of upper bainite, MA-constituents and bainitic ferrite increases, as the amount of diffusion increases with decreasing cooling rate [52].

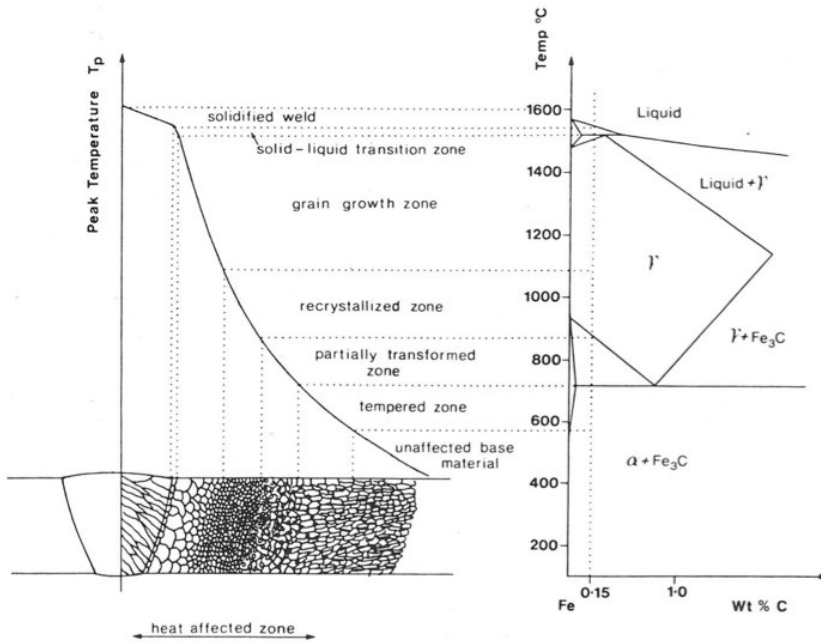


Figure 2.10: Weld zones in single-pass welds [10].

2.6.4 The Heat Affected Zone Formed During Multi-Pass Welding

During two cycle welding, the HAZ microstructure formed in the first weld pass is further altered, and Local Brittle Zones (LBZ), like MA constituents, consisting of martensite and retained austenite, may form [41]. After the second weld pass, the CGHAZ regions that retain a coarse grained structure are defined as the Intercritically Reheated Coarse Grained Heat Affected Zone (ICCGHAZ) and the Subcritically Reheated Coarse Grained Heat Affected Zone (SCCGHAZ) [37, 41, 51]. The ICCGHAZ forms during the second weld pass when the CGHAZ from the first weld pass is reheated to a temperature in the two phase area between A_{c1} and A_{c3} in the phase diagram. Here, austenite forms at previous austenite grain boundaries or between laths of ferrite or martensite sideplates [38, 39].

Since the time for carbon diffusion is limited during welding, and the supply of carbon from the ferrite matrix is high, the austenite will contain a high level of carbon. When the steel is cooled rapidly from the austenite area, the austenite will only partially transform to martensite, resulting in a final microstructure of a mixture of martensite and retained austenite [41]. Due to the high carbon content in the austenite, twinned martensite will form [25, 39]. At lower cooling rates both bainite and martensite may form in addition to martensite [52].

The unchanged CGHAZ, the ICCGHAZ, and the SCCGHAZ regions are normally associated with the lowest HAZ toughness in steels, and are often termed LBZs due to brittle MA regions and other brittle phases found in nearby regions [41]. The different weld zones formed during single and two cycle welding are shown in Figure 2.11.

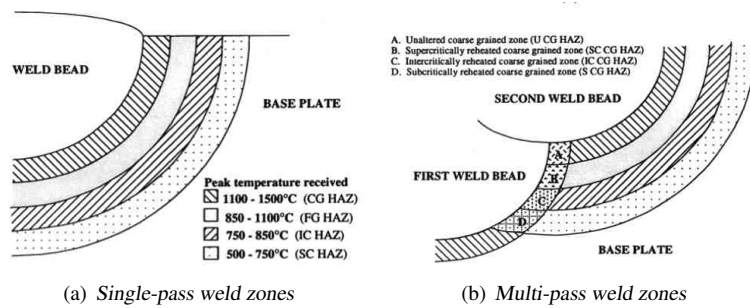


Figure 2.11: Schematic figure of the HAZ zones developed during:(a) single-pass welding and b) multipass welding [41].

2.7 Local Brittle Zones

The degradation of the fracture toughness of HSLA steels after welding has been associated with the formation of (LBZ), like MA-islands in the HAZ [42, 50, 52]. The ICGHAZ, CGHAZ and SCCGHAZ are considered to be possible LBZs [37], where especially the coarse grained regions closest to the fusion boundary tend to have lower toughness than other parts of the HAZ [50]. Several metallurgical factors contribute to the low toughness of LBZs, including a matrix microstructure of upper bainite, micro-alloy precipitation, large prior austenite grain size and martensite islands, most commonly formed at prior austenite grain boundaries in the CGHAZ [42]. Embrittlement of the ICCGHAZ can occur when pearlite decompose during the first weld cycle and later re-transforms from austenite to martensite upon cooling, and is closely related to the formation of twinned martensite during the weld thermal cycle [39].

2.7.1 The MA Region

MA constituents are one of the most studied LBZs. MA constituents, or MA islands, are regions composed of high-carbon martensite and retained austenite surrounded by a bainitic ferrite matrix. These constituents are formed during heat cycles with medium cooling rates from high temperatures, where high strength steels consist of austenite [53, 54]. The morphology of the MA constituents formed during welding is dependent on the cooling time [55]. MA constituents primarily appear with two distinct morphologies [17, 25, 41, 56]:

1. *Blocky particles* that form at prior austenite grain boundaries, often referred to as MA islands [25]. These particles are usually of the order of 3 to 5 μm in diameter [41]. These are formed at longer cooling times.
2. *Elongated stringer or lath-type particles* that develop between bainite or martensite laths. These particles are observed to be about 0.2 to 1 μm wide and several microns in length [41]. They are formed at short cooling times, where the thickness is seen to increase with increasing cooling times. The lath shaped islands are parallel and possess directionality [17].

In addition, the MA constituents can be described as connected or nearly connected MA particles and Martensite-Austenite-Carbide (MAC) structures, where a second phase, like carbide and ferrite is present in addition to the MA constituents [25]. These MA morphologies form at higher cooling rates than the two types described above.

The amount of MA constituents formed increases with increasing cooling times to a certain maximum time is reached. Further increase in the cooling time will lead to a reduction in the amount of MA constituents present, since the formation of austenite, ferrite and carbides become possible at longer cooling times 2.3 [55]. Retained austenite can be present in the martensite constituents, if the M_f temperature of the steel lies below room temperature [39].

MA constituents are brittle due to their high carbon content, and are therefore usually not desired. The shape, size and distribution of the MA region will affect properties of the weld zones in which it appears [40], like toughness and the transition temperature. The toughness tends to decrease with increasing amount of MA constituents present in the material [54]. The presence of MA constituents increases the transition temperature of the steel, so that fracture may occur by a brittle fracture mechanism at higher temperatures [55].

Longer cooling times makes the MA regions less harmful, as less volume of MA constituents are formed. In addition, the formed MA constituents contains less carbon if the cooling time increases, as some carbon may be able to diffuse out of the austenite. This makes the tetragonality of the BCT cell less pronounced, leading to less mismatch and smaller strains at the interface between the matrix and the MA constituents.

MA constituents are commonly studied using optical light microscopy and scanning electron microscopy, where the identification of the constituents is not always straight forward since their occurrence in samples etched with the commonly used etchant for steels, Nital, is often misinterpreted as carbides of ferrite-carbide aggregates [54].

2.7.2 Toughness in the CGHAZ and ICCGHAZ

The toughness drop in welded steel has been observed to be lowest in the CGHAZ and in the ICCGHAZ of multipass welded joints [9, 37, 38, 41, 50, 52, 57–59]. It has been reported that the toughness values are lowest in the ICCGHAZ, followed by the CGHAZ. The ICCGHAZ has a low toughness since it is the most embrittled region in weldments of structural steels, mainly due to the formation of coarse martensite islands [37]. The fracture toughness has been seen to decrease with increasing T_p in the CGHAZ [39].

Research has shown that the presence of MA constituents is not necessarily detrimental to toughness alone. There must be a particular distribution, morphology and hardness difference between the MA constituents and the matrix microstructure of the steel in order to generate a significant reduction in toughness [12, 41]. This also leads to the DBT being shifted to higher temperatures. It has been shown that the elongated MA constituents are more detrimental to toughness than the blocky ones [40].

2.7.3 Fracture Associated With Local Brittle Zones

The embrittlement of the ICCGHAZ in HSLA steels has been associated with the development of both twinned martensite and MA constituents. MA constituents can act as crack initiation sites and promote crack propagation[40].

There are four proposed mechanisms for cleavage initiation due to the presence of MA particles [25, 41, 56]. These are illustrated in Figure 2.12 and include:

1. *The MA particles are brittle and crack easily. This causes microcracks and cleavage to initiate in the surrounding ferrite matrix.*

MA particles can act as crack initiation sites as well as assist crack propagation. Cracking of MA particles are observed in both block and stringer constituents. At low temperatures, the presence of blocky MA constituents are believed to increase the matrix stresses close to the interface between the matrix and the MA constituents, which may lead to cleavage crack initiation. The stringer particles are not effective obstacles for crack propagation, as they crack more easily than the blocky particles [25].

2. *Transformation induced residual stress is produced in the surrounding ferrite matrix during formation of MA constituents, assist cleavage fracture.*

The volume increase associated with the transformation from austenite to martensite generates elastic plastic strains in the ferrite matrix, which assists cleavage fracture. This effect is magnified when transformation induced stress fields originating from several closely spaced blocky MA constituents overlap.

3. *MA particles have higher hardness than the ferrite matrix, which induces stress concentrations in the neighbouring ferrite matrix. These stresses assists cleavage fracture.*

The difference in hardness between the MA constituents and the matrix increases the stress concentration during deformation. When subjected to high loads, the matrix starts to deform plastically and stress can be generated in the matrix close to the MA constituent. As large stresses can develop across the interface between the MA constituent and the matrix, this may lead to debonding of the MA particles from the matrix, if the stresses developed are high enough. In addition, if the interface is weakened by carbon segregation, this mechanism is more likely to occur.

4. *Microcracks can be formed at the interface between MA particles and the ferrite matrix due to particle debonding followed by brittle propagation or linking with other debonded regions.*

Micro cracks can initiate when the MA particles debond from the matrix and propagate in a brittle manner or by linking of other debonded regions. The stringer type particles debond more easily due to lower interfacial energy compared to that of the blocky particles. While stringer formed particles more readily debond, the blocky particles are more prone to cracking.

The degree of embrittlement and the size and location of the coarse-grained HAZ regions depend on the steel chemistry, the heat input (cooling rate and thermal cycle), the angle of attack between the electrode and the preparation edge, and the degree of weld bead overlap [50].

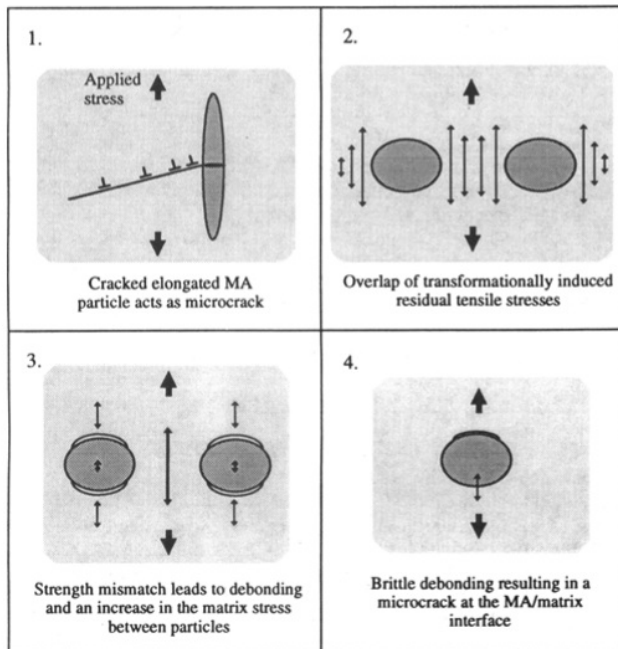


Figure 2.12: Schematic presentation of the four proposed initiation mechanisms [41].

2.8 Fracture Toughness Testing

The aim of fracture toughness testing is to measure a critical value of the stress intensity, K , at the crack tip necessary to cause plane strain unstable fracture [60]. The aim of fracture toughness testing is to obtain a reproducible value of the lower bound critical toughness, K_{IC} , of a material [24]. The K_{IC} , can be determined by quasi-static testing, where measures can be done directly, as a critical stress intensity factor if failure occurs within the LEFM regime.

When measuring K_{IC} , certain specimen requirements apply in order for a result to be considered valid in the given environment and for the given test temperature and loading rate. A plane strain lower bound K_{IC} is only obtained for specimens with thickness above a critical value, where the crack tip deformation is not affected by the structure geometry. This means that the plastic zone size in front of the crack tip must be much smaller than the thickness of the specimen. In addition, the crack length has to be much smaller than the thickness in order to obtain a single value of K_{IC} [24, 61]. K_{IC} variation with specimen thickness can be seen in Figure 2.13.

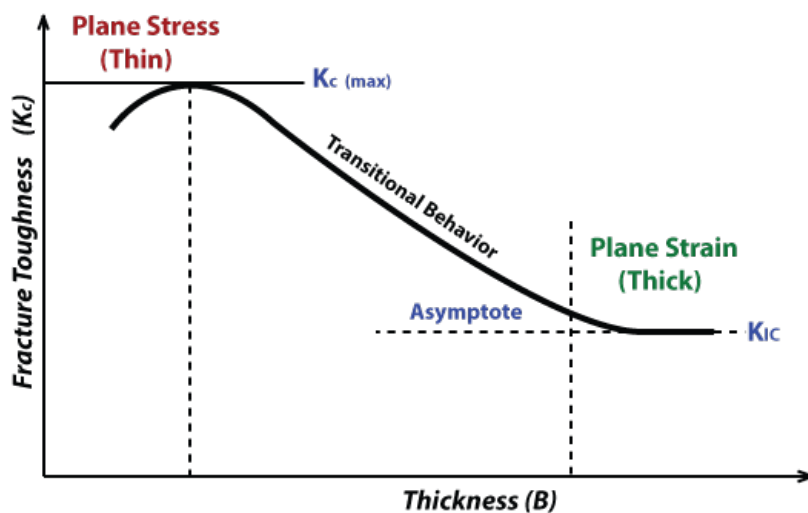


Figure 2.13: Illustration of how the measured fracture toughness is dependent on the thickness of the test specimen. A lower bound fracture toughness, K_{IC} , is obtained when the specimen fractures in plane strain where the stress intensity factor reaches a critical level. The stress state is that of plane stress when using thin specimens and plane strain when specimens of greater thickness are used. Figure redrawn after [26, 34, 62].

The size requirements according to ASTM [35, 61] are that the specimen thickness, B , must be greater than the value given by Equation (2.8) for LEFM and SSY and the crack length, a , width, W , as well as the specimen ligament size, $(W - a)$, has to be smaller than the value given by Equation (2.8). These requirements must apply in order to assure plane strain conditions [24, 63] and conservative results.

$$a, B, (W - a) \geq \left(\frac{K_{IC}}{\sigma_y} \right)^2 \quad (2.8)$$

However, if yielding occurs before fracture, K_{IC} can be measured by means of the J-integral or CTOD [26, 61, 64]. The equations relating CTOD to the fracture mechanical parameters, K , J and CTOD are listed below [22, 23, 65, 66].

$$CTOD = \frac{K^2}{\lambda E' \sigma_Y} \quad (2.9)$$

$$J = \lambda \sigma_Y CTOD \quad (2.10)$$

$$K_J = \frac{JE}{1 - \nu^2} \quad (2.11)$$

The constant λ is usually set equal to 2 in plane stress and 1 in plane strain. E' equals Young's modulus, E , in plane stress, and $\frac{E}{(1 - \nu^2)}$ in plane strain, where ν is the Poisson's ratio. For all developed correlations, caution should be applied when used with the purpose of safety assessment welded joints. Therefore, safety factors should be included and correlations should be validated by fracture mechanics testing of data from the literature [65].

2.8.1 The CTOD Test

In tough materials, e.g. in steels above the DBTT, plastic deformation leads to blunting of a sharp crack prior to fracture. The degree of crack blunting increases in proportion with the toughness of the material. Hence, the opening at the crack tip, the CTOD, often designated δ , can be regarded a measure of the fracture toughness of a material [23]. There are several definitions of the CTOD, where the two most common definitions are

the displacement at the original crack tip and the 90° intercept from the blunted crack tip to the sides of the crack, as illustrated in Figure 2.14. The methods are equivalent if the crack blunts in a semicircle. The use of CTOD as a measure of fracture toughness was

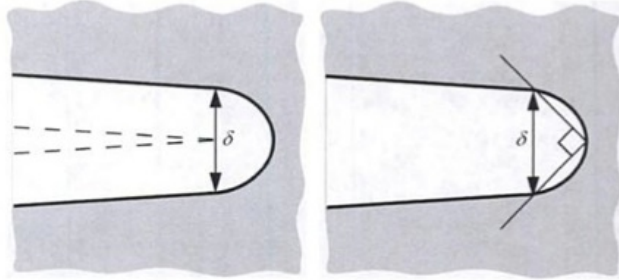


Figure 2.14: Two definitions of the CTOD [23].

first suggested by Wells, and can be used as a fracture toughness parameter for materials too tough to be characterized by LEFM, i.e. when LEFM is no longer valid. It describes the crack tip conditions in elastic-plastic materials, and represents a failure criterion in EPFM, just like K_{IC} in the case of LEFM [23].

The CTOD test is usually performed using a pre-cracked specimen loaded in three point bending. During a CTOD test, the specimen is subjected to increasing load and the crack tip plastically deforms until a critical point is reached, where a drop in the applied load occurs. The CTOD corresponding to the point of maximum applied load and is used as a measure of the fracture toughness.

As it is difficult to measure the exact CTOD, the displacement at the crack mouth, the Crack Mouth Opening Displacement (CMOD), is often measured using strain gauges attached to a clip placed at the mouth of the machined notch [61]. The CTOD can then be found from geometrical considerations. Full-thickness testing is commonly performed, where the specimen geometry is set by standards. The test is often performed at the minimum design temperature in order to obtain a conservative value of K_{IC} . A typical test set-up and specimen geometry and dimension requirements are shown in Figure 2.15(b) and 2.15(a), respectively.

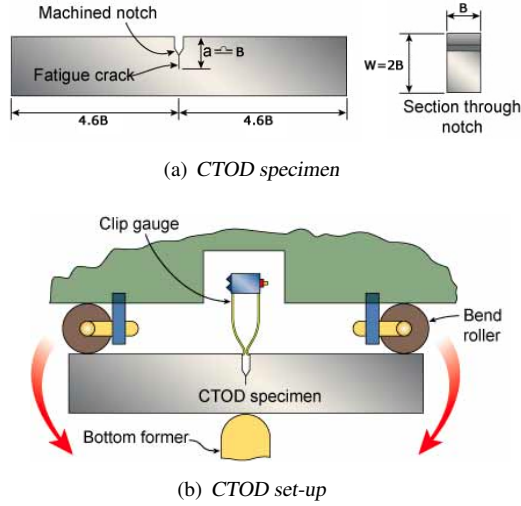


Figure 2.15: The CTOD test using SENB test geometry: (a) The CTOD specimen geometry and (b) the CTOD set-up [67].

In order to calculate the K_{IC} from the CTOD, the load at fracture and the amount of crack opening at the point of propagation is needed, like in Equation (2.12),

$$K_i = \left(\frac{P_i S}{(B B_N)^{\frac{1}{2}} W^{\frac{2}{3}}} \right) f\left(\frac{a_i}{W}\right) \quad (2.12)$$

where S is the specimen span (the distance between specimen support), B is the specimen thickness (B equals B_N if the sample does not have any side grooves), W is the width of the specimen and a specific applied load, P_i . The K_{IC} can also be estimated using Equation (2.9).

2.8.2 Fracture Toughness Testing and the Charpy Notched Impact Test

Direct determination of the fracture toughness by quasi-static testing can be costly and require a large material volume, hence the Charpy V-notch impact test is often used to estimate the fracture toughness of a material. According to BS7910:2005 [66], direct determination of fracture toughness by testing is always preferable, but where this is not possible an estimation of K_{IC} , denoted K_{mat} or K_{JC} , may be obtained from correlations with Charpy V-notch impact test data taken from material of the same general

microstructural type (e.g. weld metal, HAZ, parent material) in which the flaw is situated. The orientation of the Charpy V-notch specimens should be such as to produce the fracture path that would result from the flaw under consideration.

In addition to estimate K_{mat} , the CVN test can be used when estimating the transition temperature, T_{trans} , from fracture mechanical tests, where it is recommended that testing is performed as close to T_{trans} as possible. In this respect, the CVN test is often used to estimate an initial start temperature from where testing should be performed.

2.9 The Charpy Notched Impact Test

The Charpy notched impact test is a dynamic fracture test used mainly for design of structures or components that must handle dynamic loads. It represents one of the early tests used to evaluate the effects of low temperature upon the behaviour of metals [15]. During the test, the notch toughness of a metal is indicated by the measured amount of energy absorbed in fracturing a test specimen, C_V . The Charpy test can be used to predict whether a certain steel will fracture by a ductile or brittle fracture mode at a given temperature. A brittle material will absorb little energy while a ductile material will absorb a larger amount of energy when a Charpy test is performed [68].

Because the Charpy test is simple and inexpensive [64], it has been used to measure the notch toughness in materials for quality control and ranking purposes. The test is also cheaper to perform and require less equipment and experience than quasi-static testing, and is often used when it is impossible or impractical to perform an actual fracture toughness test. It is the most commonly used standard test to evaluate the fracture properties of a material [26].

2.9.1 The Charpy Specimen

The standard Charpy specimen is a simple notched beam impacted in three-point bending [23]. According to the standard ASTM E23-12c [29], the standard Charpy-V Notch (CVN) specimen should have dimensions as given in 2.16, with a length of 55 mm and height and with both of 10 mm with a notch depth of 2 mm, an angle of 45° and a radius of curvature of 0.25 mm. If the plate thickness is less than 10 mm, sub-sized specimens can be used, where all the specimen dimensions are reduced equivalently. However, extrapolating results from sub-sized specimens to correspond to standard specimens is difficult [26].

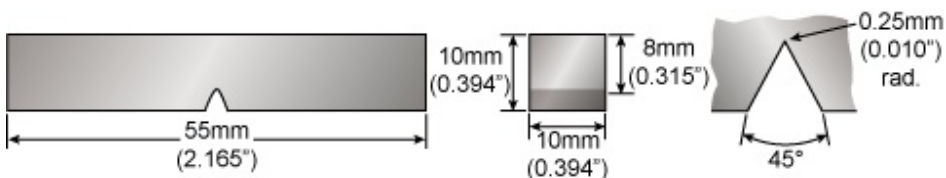


Figure 2.16: The standard Charpy specimen [69].

2.9.2 Charpy Test Data and Procedure

During a conventional Charpy test, the notched specimen is supported at the ends and struck in the notch by a pendulum. The C_V is calculated from the measured height difference of the pendulum before and after the test is performed. Normally, each set of Charpy impact tests consists of three specimens tested at the same temperature, and the values are averaged to obtain a single energy value [23, 65, 68].

In addition to the impact energy, Lateral Expansion (LE), which defines the specimen deformation, as well as the percentage crystallinity of the fracture surfaces [70], also known as the Percent Shear Area (SA), which describes where in the DBT region the test result is situated [26], can be determined from the Charpy test. The fracture surface of the Charpy specimen can be divided into different zones relating to the fracture initiation region, shear lips, and final fracture region, as shown in Figure 2.17.

The SA is determined based on the proportional amount of ductile crack growth (d_{cg}) and shear fracture areas (s) (fracture initiation region, shear lips, and final fracture region, defined in Figure 2.17), divided by the total fracture surface area, times 100 as in Equation (2.13) [26, 71]. The total area minus the unstable fracture area, or cleavage fracture area (c), on the total fracture surface area gives the same result.

$$\%SA = \frac{\Sigma A_{d_{cg}} + \Sigma A_s}{\Sigma A_{d_{cg}} + \Sigma A_s + \Sigma A_c} \cdot 100\% \quad (2.13)$$

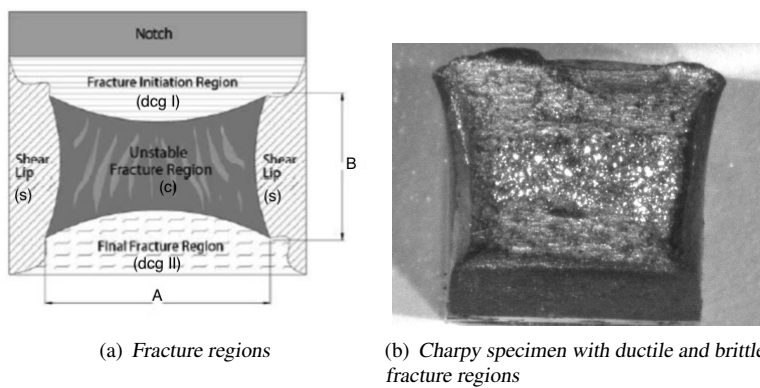


Figure 2.17: (a) The various fracture regions in a Charpy specimen. A and B are average dimensions [29] and (b) fractured specimen with crystalline and ductile regions [71].

When performed over a range of temperatures, the Charpy test can be used to obtain a DBT curve for a given metal from which an estimate of the T_{trans} can be determined. A typical shape of a DBT curve can be seen in Figure 2.5, where the middle of the transition region serves as a rough estimate of T_{trans} . A SA of 100% indicates that the C_V lies within the upper-shelf region. In the transition region, the SA is typically between 30% and 60%, where the C_V is extremely sensitive to temperature changes [26].

2.9.3 Charpy Data Report Methods

The C_V values can be reported in four different ways [65]:

1. Reporting that the Charpy requirements for the particular level of energy and a certain temperature have been met.
2. Reporting the actual C_V at the test temperature. Normally three tests are taken at the test temperature.
3. Reporting a C_V like as in the previous point together with the per cent crystallinity value (or SA).
4. Report of a full C_V impact transition curve. The per cent crystallinity values or curves may be added.

Usually, the last reporting method is preferred.

2.9.4 Stress State

When a notched specimen is subjected to loading, a normal stress acts across the base of the notch, which tends to initiate fracture. In the case of cleavage, fracture is prevented as long as the cohesive strength of the material is higher than the local normal stresses [23]. In test specimens, it is common for plastic deformation to occur before fracture. In this case, the applied force also sets up a shear stress in addition to the normal stress, at an angle of about 45° to the normal stress. The elastic behaviour of the material terminates as soon as the shear stress exceeds the shear strength of the material, where deformation i.e. plastic yielding starts. This is the condition for ductile failure [29], as previously described.

2.9.5 The Instrumented Charpy Test

The instrumented Charpy test provides additional data compared to the conventional Charpy test. During an instrumented impact test, the load-time history of the striker is recorded. This can be used to obtain a load-deflection curve and to calculate fracture initiation and propagation energies [9].

The instrumented Charpy test can be considered a miniature dynamic fracture toughness test [9, 23], and pre-cracked specimens can be used in this regard [72]. The dynamic fracture toughness, K_{ID} , is usually lower than the static fracture toughness, K_{IC} [9]. In addition to the K_{ID} and C_V , four distinct points on the load-deflection curve can be identified, as shown in Figure 2.18. These are F_{gy} , F_m , F_u and F_a , representing the force at the beginning of general yield, the maximum force, the force at the onset of brittle fracture and the force at brittle fracture arrest respectively [26, 73]. By using these four force parameters, it is possible to divide the impact energy into several regions and estimate the energy needed for distinct fracture events.

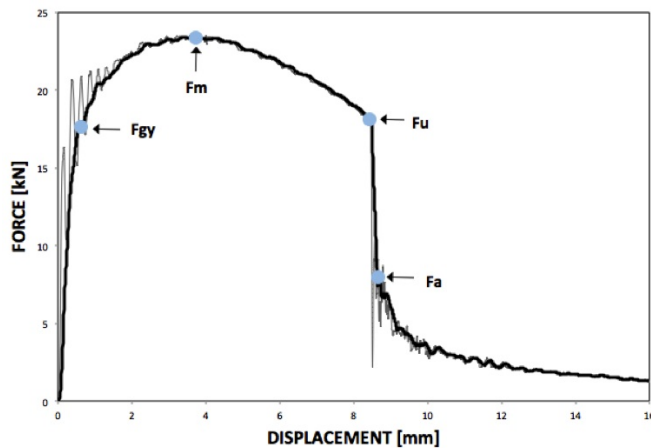


Figure 2.18: Typical curve obtained during an instrumented Charpy impact test of a ductile material. The different force parameters, as defined in [26], the force at general yield, F_{gy} , at maximum load, F_m , at the onset of brittle fracture, F_u and at the beginning of brittle crack arrest, F_a , are shown [74].

Certain conditions should be met when conducting an instrumented Charpy test. One criterion is that the impact velocity must be sufficiently low so that inertia effects are dissipated before load and time measurements of importance are made. A criterion suggested to overcome this challenge is that the time-to-fracture must be greater than three times the apparent specimen oscillation period (3τ criterion). Especially when testing within the lower shelf region, inertia effects may influence the measurements of the fracture load as fracture may occur without satisfying the 3τ criterion. Using strain gauges might help in overcoming this problem [75]. When testing at highest temperatures, the oscillations are usually damped out by plasticity before maximum force is reached [76].

2.9.6 Fatigue Pre-Cracked Charpy Specimens and Measured Energy

Pre-cracked specimens can also be used during instrumented Charpy testing [72]. Because the root of the notch in a Charpy specimen is blunt and not as sharp as assumed in classical fracture mechanical theory, there has been a trend toward using standard Charpy specimens with a fatigue crack at the tip of the conventional V-notch [9, 26].

During a standard non-instrumented CVN test, the total energy needed for both the crack initiation and crack propagation is included in the energy measured. Due to the large amount of energy needed to generate a crack at a blunt notch, the initiation energy can be larger than the energy needed for crack propagation, especially for low toughness/brittle conditions, and separating the initiation energy from the propagation energy is challenging, and impossible when not instrumented. When an instrumented test is performed, separating the different energies can be hard due to inertia effects that may make the resulting load-deflection curve hard to read. Therefore, the total energy absorbed by a specimen from a standard CVN test may not predict the conditions of a situation where an existing crack in a material propagates, which may lead to wrong conclusions [77].

The energy needed to re-initiate a sharp crack already present in a material may be quite low. Therefore, in theory, using fatigue pre-cracked Charpy specimens may in some cases allow for isolated measures of the load used to propagate a crack, as pre-cracking reduces

the energy required to initiate crack propagation [26, 78]. Introducing a fatigue pre-crack is also a method of increasing the constraint in the Charpy specimen. A sharp crack increases the level of tensile stress below the notch [78], which influences the fracture mechanism.

2.10 Fracture Testing of the HAZ

It has been shown that the measured CTOD value is strongly affected by the presence of LBZs at the fatigue crack tip, and the different microstructures found in the HAZs leads to variations in critical measured CTOD values. Low values are often observed if the fatigue crack tip samples a LBZ, where both the size and microstructure of the LBZ affects the measured CTOD. The CTOD are seen to decrease with increasing LBZ size. For the same LBZ size, ICCGHAZ testing generally result in lower CTOD values than when CGHAZ samples are tested [37].

In the case of fracture toughness testing of the HAZ, the location of the fatigue crack is very important, as an incorrectly positioned fatigue crack may not sample the a critical flaw, making the test invalid. When fracture testing is performed, it is important that the weak link in the material is sampled. The distance between the fatigue-crack tip and the weak link as well as the orientation of the weak link is important in this regard. The weak link should be well oriented with respect to the fatigue crack tip, the process-zone stresses, and the cleavage plane of the neighbouring microstructure [42]. In order to make sure that the crack tip is located in the correct region, polishing and etching followed by metallurgical examination must be carried out before the notch is machined and the fatigue crack is made.

For Charpy specimens, the notch has to be carefully positioned or a large number of specimens have to be tested in order to make sure that the brittle zones in the material are sampled in order to make sure that conservative results are obtained. For welded structures, this is difficult, as the microstructure in the heat-affected zones may vary notably with position [70].

2.11 Weld Thermal Simulation

The brittle HAZ microstructures can be derived using weld thermal simulation. This allows for investigation of homogeneous samples from different regions of the HAZ and can be used to provide input on fracture toughness in brittle microstructures and the effect of welding in real materials, as the microstructure of interest can be obtained over a larger region [16]. In real welds, the HAZ may be very narrow, making testing difficult and unreliable. The method is also reproducible, so that a large number of specimens with the same microstructure can be made.

Weld simulation produces a brittle homogeneous microstructure, which may result in too conservative test values during fracture toughness testing, due to the fact that only one microstructure is sampled, whereas a microstructural gradient is usually present in real weld HAZs. Nevertheless, it has been stated that toughness values obtained for weld simulated material and real welds are comparable [12, 41]. Another difference of significance is that weld thermal simulation does not take residual and thermal stresses into consideration. Therefore, weld simulation is valuable only for general characterisation, toughness measurements and failure analysis [41].

2.12 Crack Arrest

The concept of crack arrest provides a supplementary approach to conventional structural assessment, where the initiation of cracks should be prevented. Crack arrest occurs when crack extension starting in a region of high stress or in local brittle zones is arrested due to sufficient resistance in the surrounding material [79]. The crack arrest properties of a material can vary locally, depending on local stress concentrations, residual stresses and local brittle zones formed during welding.

High crack arrest properties can be found for example at grain boundaries. Local crack arrest can be seen as an unbroken ligament on the fracture surface. Macroscopic crack arrest occurs when a sufficient part of the crack front has arrested [26]. The stress intensity can be used in describing arrest properties of a material, where arrest occurs when the local crack driving force at the crack tip decreases below the local arrest toughness, K_{Ia} , over a sufficiently large area from the crack front.

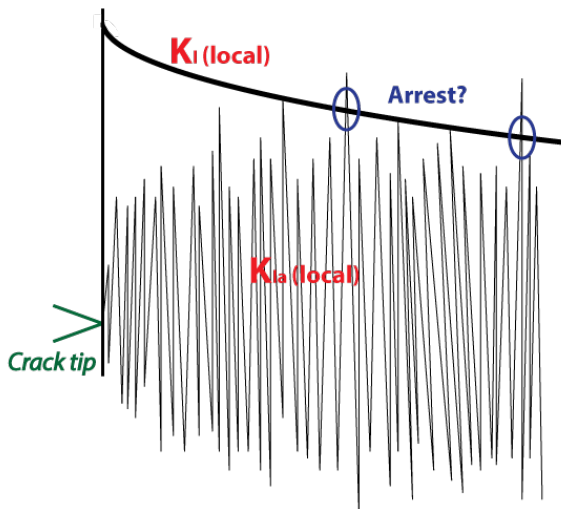


Figure 2.19: Schematic representation of the reason for scatter in crack arrest toughness. Redrawn after Wallin [26].

The true dynamic crack arrest toughness K_{IA} , represents the value of the dynamic stress intensity factor, K_{ID} , at crack arrest, where K_{ID} increases with increasing crack velocity and initiation toughness. K_{IA} considered to be a material parameter, representing the minimum dynamic fracture toughness of a material. The fracture arrest toughness based on static analyses, K_{Ia} , is often used in determining K_{IA} . If the crack driving force, K_I , is less than K_{Ia} , the crack will arrest, and fracture will not occur. Although static analyses are commonly used to estimate K_{Ia} , the dynamic and static arrest toughness are usually not equal. However, static tests provide a conservative estimate of the toughness, and are therefore commonly used for obtaining estimates of the toughness [26].

3 Previous Work

This master's thesis is a continuation of parts of a project thesis written by the author in cooperation with DNV GL and the Arctic Materials Project in SINTEF during the fall of 2013 [74]. The main focus of the project was the Charpy impact test and possible correlations between Charpy and fracture toughness values, like K, J and CTOD. As Charpy testing continues to be widely applied both for quality control measures and is often performed as a substitute for quasi-static fracture mechanical testing due to lack of material and high costs associated with these tests, it is important to continue the research on the correlations between the tests.

The work performed connected with the project thesis was twofold, and included the following parts:

1. A literature study on the physical differences between the Charpy test and quasi-static fracture mechanical tests and the correlations between data obtained in the two tests presented in earlier literature. The differences between the CVN test and quasi-static fracture mechanical test methods were studied as they affect the correlativity between the data obtained from the two tests [65].
2. A comparison of data obtained during instrumented Charpy testing of specimens with a conventional notch and with a sharp crack at different temperatures. This was done in order to get a better understanding of the effects of the blunt notch used in conventional Charpy testing.

The 420 MPa steel studied was the same as the steel studied in the present master's thesis. Both weld simulated CGHAZ and base material were investigated in order to see how welding of the steel affected the data obtained. A fracture surface examination was carried out in a Scanning Electron Microscope (SEM) in order to get a better understanding of the results from the instrumented Charpy tests performed and the differences between a sharp

and a blunt crack. The findings from the project thesis of most importance in relation to this master's thesis are presented subsequently, mainly with focus on parts and findings relevant for low temperature applications and the lower shelf of the transition curve. Some additions has been made to better the relation to the work performed in the present thesis.

3.1 Physical Differences Between the Charpy Impact Test and Quasi-Static Fracture Mechanical Tests

The main factors making simple relationships between qualitative and quantitative measures of fracture toughness difficult are described in the following sections. These include various root radius (ρ), specimen size, loading rate and the differences in actual measured data [28]. An overview of the most important differences between the tests are listed in Table 3.1.

Table 3.1: Physical differences between the Charpy impact test and quasi-static fracture mechanical tests, where K_{IC} is the fracture toughness for mode I loading, σ_Y is the yield strength, B is the specimen thickness and ρ is the root radius [60, 80].

Feature	Charpy test	K_{IC} tests
Specimen size	$10 \cdot 10 \cdot 55 \text{ mm}^3$	$B \geq \left(\frac{K_{IC}}{\sigma_Y} \right)^2$ Full thickness test often required
Loading rate	Dynamic $10^5 - 10^6 \text{ MPa}\sqrt{\text{mm/s}}$	Static $< 3 \text{ MPa}\sqrt{\text{mm/s}}$
Flaw geometry	Short blunt notch $\rho = 0.25 \text{ mm}$	Deep crack $\rho \rightarrow 0$
Event described in test	Fracture initiation and propagation	Fracture initiation

3.1.1 Specimen Size

Fracture mechanical test specimens are generally much larger than Charpy specimens, as full thickness tests are often performed [65]. Standardized fracture toughness testing require sufficient specimen thickness to ensure plane-strain conditions at the crack tip as well as a crack depth of at least half the specimen width. Plane strain condition at the crack tip is needed in order to obtain a lower-bound K_{IC} [81]. In Charpy specimens, plane-strain conditions are generally obtained only at low temperatures in the lower shelf regime [70].

The specimen size is especially important in the case of brittle fracture and for lower shelf correlations, i.e. at temperatures below the DBTT, as it is more likely to sample a locally brittle microstructure or a “weakest link” in the material in front of a crack tip in a large specimen, due to the larger crack front. The probability of fracture is highly related to

the likelihood of finding a critical defect in the material in front of a crack tip, a weak link in the material, where the stresses are high [82]. Therefore, the fracture probability increases with increasing specimen size, and also increases the probability of measuring a lower bound K_{IC} . Therefore, the transition temperature tends to increase as the specimen size increases, i.e. the DBT is shifted to higher temperatures [22, 24, 26]. The specimen size also affects the level of constraint in the specimen, leading to a relative shift in the transition temperature curves for the different specimens [65].

3.1.2 Flaw Geometry

It has been shown that the stress state in front of the notch in the CVN specimen is plane strain at fracture initiation, which is equal to the stress state in a K_{IC} specimen [83]. However, as crack initiation is a function of the stress intensity at the crack tip, direct comparison between initiation in Charpy and fracture mechanical specimens is difficult [70].

The stress state in front of a blunt notch is different from that of a sharp crack, where the stresses are generally higher in the case of a sharp crack [23, 84]. As the flaw geometry affects the stress state at the crack tip, it also affects the fracture behaviour of the specimen. The different stress state close to a notch and a sharp crack affects the likelihood of brittle fracture to occur in the specimen, and will also affect the shape of the transition curve [70]. The stresses are higher in front of a sharp crack, which increases the likelihood of brittle fracture to occur.

Whether a material shows brittle or ductile behaviour, depends on whether the normal stress exceeds the cohesive strength before the shear stress exceeds the shear strength of the material, where shear stresses are set up by the applied force in an angle of about 45° relative to the normal stresses. The fracture is brittle if the cohesive strength is exceeded by the normal stresses without deforming the specimen, while the fracture is ductile when the shear stress exceeds the shear strength of the material and plastic yielding sets in [29]. Therefore, brittle fracture is more likely to occur if the root radius of the notch or crack is sharper, as the normal stress at the root of the notch will increase relative to the shear stress with decreasing root radius [29, 85].

The difference in stress state near the crack tip in notched and pre-cracked specimens makes it difficult to compare data from Charpy and fracture mechanical tests, especially in the lower shelf region [85]. As the conditions in front of a crack tip and a notch are approximately the same when a crack propagates by ductile tearing, regardless of how it was initiated, the effect of different root radius is not as evident on the upper shelf region as on the lower shelf. Therefore, it is no direct link between test results on the upper and lower shelf as well as the lower transition region [84]. Classical fracture mechanics is only valid for singular stress fields, which is not initially the case in a Charpy test.

3.1.3 Strain Rate

Fracture toughness tests are usually performed quasi-statically and the material experiences slow strain rates, whereas the Charpy energy is measured under impact loading [65], where the strain rates are experienced can be several (6-7) orders of magnitude higher than that of a fracture test [60, 84]. The loading rate in a Charpy test tends to be faster than real loading, while a traditional CTOD test tends to be slower [82] than the load situation experienced in real structures. This means that the results obtained from testing does not always mirror the conditions that real structures are subjected to, which must be taken into account when using values obtained from tests for structural assessment purposes [28].

The fracture toughness is sensitive to the strain rate as the yield strength of steels normally increases with increasing loading rate, where the strain rate sensitivity is greater for lower strength steels than for high strength steels [86]. Depending on the fracture mechanism, the effect of different strain rate on the toughness can be either positive or negative. In case of brittle (lower shelf) fracture, where fracture is stress controlled, a high strain rate decreases the toughness as high stresses promotes cleavage. The opposite is true for ductile fracture, where fracture tends to be strain controlled.

The plane strain fracture toughness of BCC materials, is sensitive to loading rate, and may decrease as the loading rate increases [36]. Consequently, the different strain rates experienced in Charpy and fracture mechanical testing of steels can give rise to a shift in the transition curves obtained from data from the two test procedures relative to each other. Higher strain rates tend to shift the transition curve of a specimen or a structural component to higher temperatures [22, 26, 65].

3.1.4 Event Described During Testing

During a quasi-static fracture toughness test, primarily only the initiation energy is measured, while both the initiation and propagation energies of fracture are included in the measured C_V . This can be explained by the fact that the presence of a sharp crack reduces the energy required to initiate crack propagation, as a sharp crack is already present, and therefore leads to lower upper shelf energies as well as shifting the transition temperature to higher values [26, 85].

As crack initiation is sensitive to local inhomogeneities, fracture toughness data are more sensitive to microstructural variations compared to CVN data due to the sharpness of the crack compared to the blunt notch and the larger specimen size commonly used where a larger material volume is sampled in front of a crack. This can give rise to variations in the measured events and the measured toughness [65], and has to be taken into consideration when developing correlations.

3.1.5 Level of Constraint

The level of constraint in a Charpy specimen and fracture mechanical test specimens may be different due to different size and root radius. When developing correlations between the Charpy test and fracture mechanical tests, it is important that the constraint levels are comparable, and that the right amount of energy is used when making correlations. It has been shown that maximum constraint exists at the tip of the notch in the CVN test specimen, so that it is to expect that the state of stress in the C_V and K_{IC} test specimen is similar [83, 87]. Changing the level of constraint can impose a shift in the transition temperature obtained from test data [82]. Fatigue pre-cracking is one method of increasing the constraint in the Charpy specimen when it deforms.

3.2 Charpy and Quasi-Static Fracture Mechanical Test Correlations

From the literature study [74], it was evident that a direct correlation between the Charpy impact test and quasi-static fracture tests cannot be obtained due to the many fundamental differences between the two. However, empirical relations used to estimate conservative values of the fracture toughness can be obtained. Also, the Charpy specimen or the specimen used in classical quasi-static fracture tests can be modified in order to predict the loads experienced by real structures in a better way and in addition reduce costs associated with fracture toughness testing.

One direct correlation between Charpy data and fracture mechanical parameters, such as K_{IC} , J and CTOD cannot be obtained over the full transition curve. Direct correlations will give good results only for a certain range of the transition curve (i.e. certain toughness ranges). Therefore, most of the developed correlations can for this reason be classified as applicable for the lower shelf, transition region or the upper shelf only. However, there are developed correlations based on a temperature shift approach that avoid this restriction [65].

The previously studied correlations mainly fall into two categories:

1. *Direct relationship between C_V and a fracture mechanical parameter.*

Examples are the Barsom and Rolfe [87] and Rolfe and Novac [63] correlations as well as the correlations for the upper and lower shelf in the SINTAP method [26, 65, 86]. The lower bound fracture toughness estimate described in the SINTAP procedure for lower shelf behaviour is also a part of BS7910 [66], and can be seen in Section 4.8 [66, 88].

2. *Relationships between transition temperatures corresponding to specific levels of C_V or fracture toughness.*

Examples are the Marandet and Sanz correlation [89] and the MC method developed by Wallin [26].

The Master Curve (MC) method developed by Wallin is important in the progress of finding good C_V - K_{IC} correlation. The MC approach is based on the theory that scatter in fracture toughness data in the transition region follows a characteristic statistical distribution, a three-parameter Weibull distribution with a slope of four, that is similar for all ferritic steels, where the shape of the fracture toughness versus temperature curve is suggested to follow the same function for all ferritic steels in the transition region. The only difference between steels is the absolute position of the curve on the temperature axis given by a reference temperature, T_0 , defined as the temperature at which the median fracture toughness is $100 \text{ MPa}\sqrt{m}$ in a 25 mm thick specimen. This means that if T_0 is known, the position of the transition curve is determined, where the function in the MC is the same for ferritic steels [26, 90].

The MC method accounts for temperature and size dependence of fracture toughness and the fracture probability for brittle fracture to occur. The range of applicability of the MC is limited to macroscopically homogeneous steels with uniform tensile and toughness properties [91] and to temperatures within the range of ± 50 celsius. The approach is based on the assumption that the features characteristic of cleavage fracture initiation and propagation control the fracture event [92]. A typical MC is shown in Figure 3.1, where the definition of T_0 can be seen graphically. The curve does not have a sharp increase in K_{JC} values at the T_0 temperatures as transition curves usually have.

The MC approach is included in the SINTAP procedure, where one approach for the three distinct regions of the transition curve are included, and has been standardized in ASTM-E1921 [90] and is also a part of the British Standard BS7910 [66]. The range of applicability of the MC testing standard ASTM E1921 is limited to macroscopically homogeneous steels with uniform tensile and toughness properties [91]. Data falling below the 2 % confidence limit or above the 98 % confidence limit curves are invalid and may indicate material inhomogeneity [91]. The equations used to link Charpy data to T_0 and the fracture toughness, K , in the MC approach are included in Section 4.8.

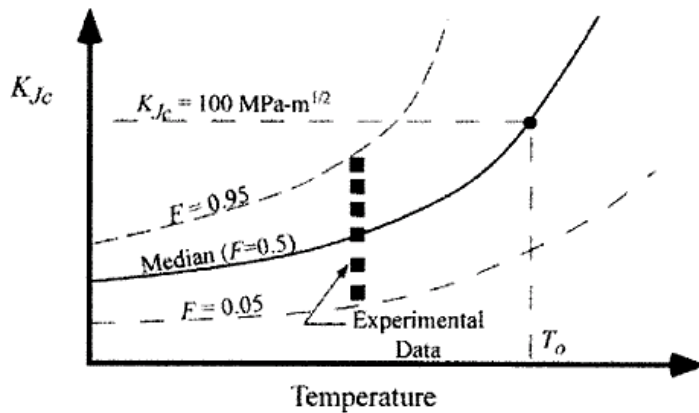


Figure 3.1: Schematic presentation of the Master Curve including the position of the defined reference temperature, T_0 , and tolerance bounds [23].

Furthermore, some of the later developments make alternative approaches in obtaining a good correlation, like using the Percent Shear Area (SA) and uses the SA and measured C_V to estimate J [84]. Also, the Accurate Fracture Substantiation Method (AFSuM) that focuses on changing the test specimens and procedures rather than obtaining a direct correlation should also be mentioned [82]. The idea is that by changing the specimen features and test procedures, the effects of the physical differences between Charpy and quasi-static fracture mechanical tests can be minimized, as well as making the tests predict failure under similar conditions as the one real structures are subjected to.

3.2.1 Correlations for Welded Materials

Most of the previous correlations are developed using homogeneous steels with uniform tensile and toughness properties, like the MC method, and only a few correlations use HAZ-material in obtaining correlations. Developing correlations for welded structures is difficult due to the microstructural complexity of welded joints. Since toughness measurements for welded material in addition to microstructure is affected numerous factors including notch position, joint configuration as well as thickness and crack size, the test data obtained for welded structured tends to be scattered, due to the many contributing factors. This makes obtaining correlations between C_V and K for weld microstructures difficult, especially for ferritic steels due to the ductile-brittle transition [65].

3.3 Scatter in Fracture Toughness Measurements Related to Fracture Mechanism

The scatter in measured data is a parameter that affects the development of reliable C_V and K_{IC} correlations. In the case of cleavage fracture, fracture toughness is not a simple material property [65]. As cleavage fracture initiation toughness is affected both by changes in the stress distribution and the probability of finding a local critical crack initiator, like LBZs, voids and cracks, this property is associated with the data being scattered.

Cleavage fracture initiation also shows a characteristic statistical size effect related to the length of the crack front that will affect the measured toughness. In the case of ductile fracture, the fracture resistance is determined by the mean toughness properties of the material, as the plastic zone is much larger compared to the plastic zone size when failure occurs within the lower shelf region. Therefore, the upper transition and upper shelf regions are associated with less scatter [65].

Due to the scatter associated with cleavage fracture, it is desirable to use large data sets to obtain a good estimate of the probability distribution and to obtain reliable data valid globally for the whole material. As fracture toughness specimens are usually larger than Charpy specimen and have a sharper crack, the data scatter will be different for the two tests as well. The varying data scatter sensitivity along the transition curve affects the reliability of the developed correlations, and makes a single correlation for the whole transition curve difficult.

3.4 Results From Instrumented Charpy Testing

3.4.1 Transition Curves

The transition curves obtained from the instrumented Charpy tests results (Figure 3.2) showed that the transition curves for the pre-cracked specimens were shifted to higher temperatures compared to the standard notched specimens. In addition, the transition region occurred over a more narrow temperature interval and the upper shelf was reached at lower measured energies for the pre-cracked specimens. The transition region was also shifted to higher temperatures for the weld-simulated CGHAZ material compared to the curves for base material, and the upper shelf was obtained at lower measured energy values. Furthermore, the ductile-to-brittle transition region seemed to be wider for welded material than for base material.

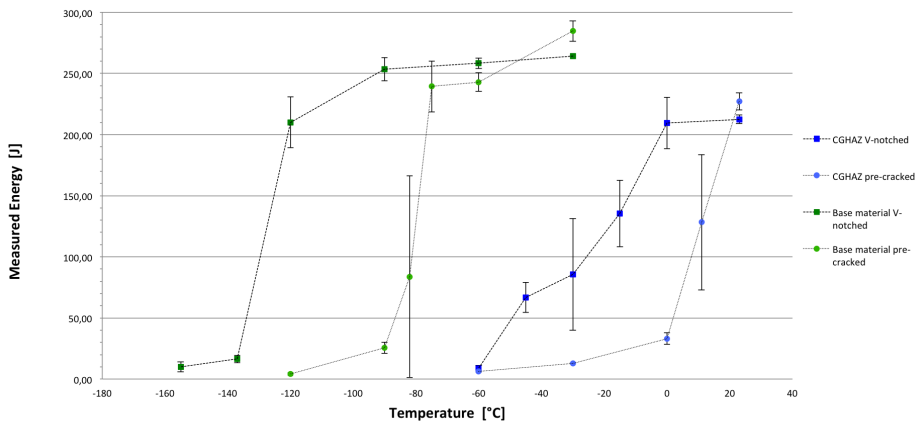


Figure 3.2: Transition curves obtained from measured energies during instrumented CVN testing of weld simulated CGHAZ (blue) and base material (green). Curves for both pre-cracked and conventional V-notched specimens are shown [74].

The lower shelf was obtained at comparable values for all the four specimen combinations, base material and weld simulated samples with both pre-crack and notch.

3.4.2 Curve Classes Obtained During Instrumented Charpy Testing

During an instrumented Charpy test, load-time curves are recorded, from which the load-deflection curves can be found by integration. These curves had different shapes, and an attempt was made to divide the curves into five distinct classes based on their shape that relates to how the measured load varies. Three different curve shapes are previously described in ASTM E23 [29], and six different curve types are described in ISO 14556 [73] and are included in Figure 3.5. The shape of the curves of the five different curve classes can be seen in Figure 3.3.

An attempt of making curve classes was made as the shape of the curves may be used to suggest the fracture mode and arrest properties of a tested specimen. All curves are included in Appendix C. Some of the curves have been revised in terms of curve class in the present master's thesis compared to class they were designated in the project thesis. The different loads that can be identified on the curves is defined in Figure 2.18, and is also given in Figure 3.5. Examples of fractured specimens from instrumented Charpy testing representing each of the curve classes can be seen in Figure 3.4. The anticipated location of the different curve classes on the Charpy transition curve can be seen in Figure 3.6.

3.4. Results From Instrumented Charpy Testing

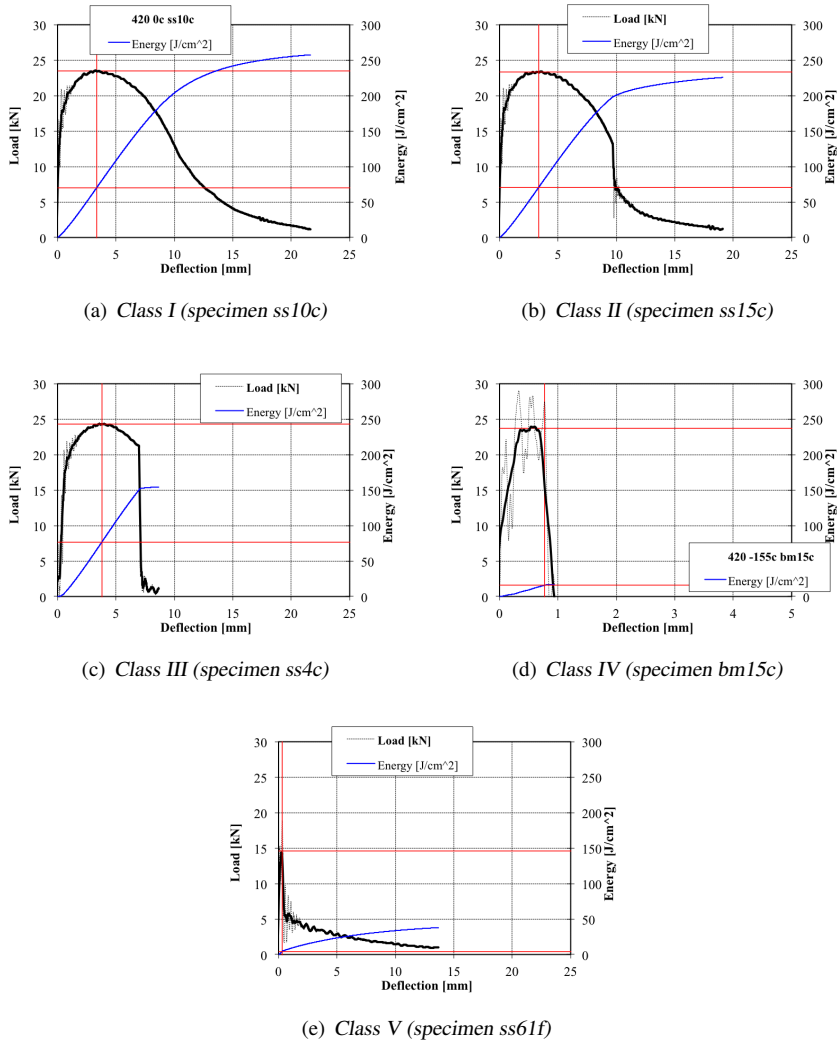
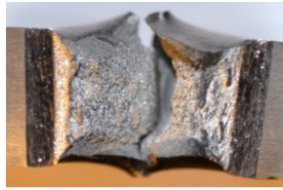


Figure 3.3: Examples of the different curve classes obtained during instrumented Charpy testing: (a) Class I (notched CGHAZ specimen tested at 0 °C), (b) Class II (pre-cracked CGHAZ specimen tested at 11 °C), (c), Class III (notched CGHAZ specimen tested at -30 °C) (d) Class IV (notched base material specimen tested at -155 °C) and (e) Class V (pre-cracked CGHAZ specimen tested at 0 °C)[74]. The different force parameters that can be identified on the curves are shown in Figure 2.18.



(a) Class I (specimen ss10c)



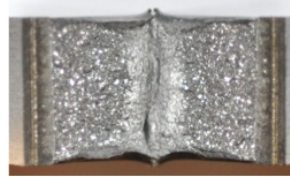
(b) Class II (specimen ss66f)



(c) Class III (specimen ss4c)



(d) Class IV (specimen ss9c)



(e) Class V (specimen ss61f)

Figure 3.4: Examples of the fracture surfaces of different curve classes obtained during instrumented Charpy testing.

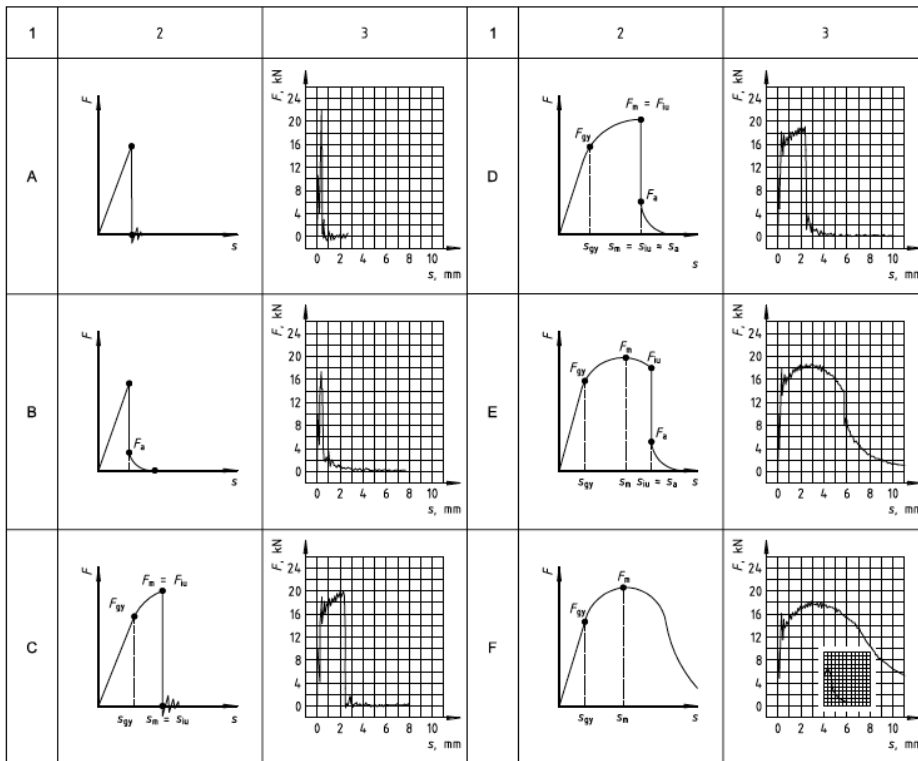


Figure 3.5: Six curve types given by NS-EN ISO 14556. Force parameters are shown.

Characteristics of the Different Curve Classes

Class I - Ductile Behaviour

Curves with a steep increase in load followed by a large area with plastic deformation, where the curve reaches a maximum load, F_m , before the load decreases gradually. Plastic deformation occurs, and both initiation and propagation processes contribute to the total measured energy. This type of curve is predominant at higher temperatures, i.e. in the upper transition region and on the upper shelf. These curves can be associated with ductile fracture.

Class II - Ductile Behaviour Followed by Arrest

The Class II curves can also be associated with a ductile fracture mode, followed by fast propagating brittle fracture before arrest at a quite high deflection value. The shape is similar to the Class I curves, but include a small load drop at the onset of brittle fracture, F_u , at a deflection value a more than double of the deflection at F_m . After F_m is reached, the load decreases gradually until F_u is reached, followed by arrest, seen as a load drop to the load at arrest, F_a . The difference between F_u and F_a is not very large. Most of the energy measured in specimens with a curve in Class II comes from crack initiation processes, although some energy is measured after initiation and also after brittle crack arrest has occurred.

Class III - Semi-Ductile Behaviour

In specimens with a Class III curve shape, some yielding occurs and a significant load drop followed by arrest right after F_m is reached can be seen. The shape is similar to the Class II curves, but with a larger load drop and at arrest and a lower decrease in load between F_m and F_u . As the load increases only a small amount after F_{gy} before F_m is reached, only some plastic deformation occurs. The load decreases only a small amount after F_m before arrest occurs, commonly at a deflection maximum two times the deflection at F_m . Hence, the energy needed to break and deform the specimen before arrest occurs, i.e. the crack initiation energy, is the main contributor to the energy measured during the instrumented Charpy test of a specimen with Class III behaviour.

Class IV - Brittle Behaviour

In the Class IV curves, F_m is reached quickly, at small deflection values. The load does not decrease before the load drops to F_a , as is the case for the Class II and III

curves. Consequently, F_m is reached at a sharper peak rather than as a point of inflection on a gently curved area. As the load drop at arrest starts from F_m , this value can also be described as F_u . Brittle fracture occurs before the sample experiences any significant plastic deformation, as F_m is reached shortly after F_{gy} . When arrest occurs, the load drops almost to zero at once, and the energy measured for samples with Class IV behaviour therefore mainly include the energy required to initiate a crack, and the fracture behaviour is brittle.

Class V - Brittle Behaviour With Gradually Decreasing Load

In the Class V curves, a low F_u is reached (F_u is also F_m in this case) at small deflection values. No yielding occurs, as F_u is believed to be lower than F_{gy} . After reaching F_u , a small, somewhat unclear, load drop occurs before the load continues to decrease gradually. The small load drop is believed to be a form of arrest, although the load drop is small and the load continues to decrease after F_a . The gradually decreasing load might be a consequence of the fact that brittle fracture initiation occurs quickly, followed by a form of arrest. Most of the samples in this class include a lot of oscillations during the gradual load decrease. As the onset of brittle fracture occurs early, specimens with a Class V curve reach arrest at an early stage, at a point where little energy is stored in the specimen. The Class V curves have a large tail, and therefore, most of the measured total energy is obtained after F_a is reached. Hence, the initiation energy is not the main contributor to the total measured energy, as is the case for the lower curve classes.

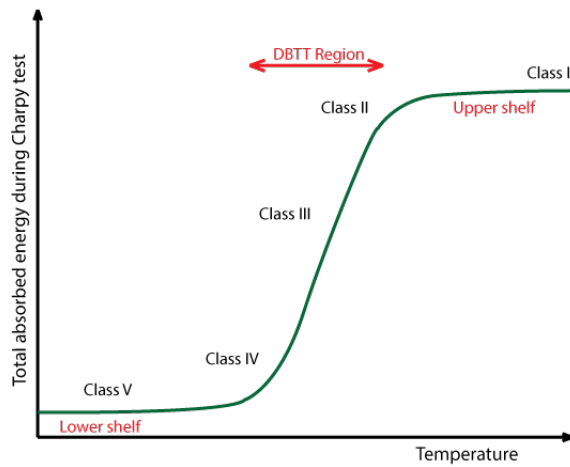


Figure 3.6: Location of the different curve classes on the Charpy transition curve. Redrawn after sketch in [93].

It was found that curve class V was not obtained for any of the notched specimens, neither for welded nor base material. The studied fracture surfaces did not show one particular fracture appearance for each of the five types of curves obtained. As the curve classes were not found to necessarily mirror the fracture mechanism observed by examination in SEM, relating the curve class to a specific fracture mode is generally not straight forward.

3.5 Fracture Surface Investigation

Six samples with C_V values in the lower shelf region were investigated in a SEM. As more samples have been investigated when working on the present master's thesis and some of the samples have been studied further, a representative collection of micrographs from all the imaged samples is included in Section 5.6 to give a better general picture of the fracture surface appearance for the samples all together.

4 Materials and Experimental Procedures

The experimental work performed in this master's thesis consist of several parts that relate to each other; an investigation of fracture surfaces of Charpy specimens using SEM and OLM, obtaining transition curves from measured Charpy data, plotting and calculating parameters obtained from the instrumented Charpy test and making plots to allow for investigation of the degree of correlation of two different correlation methods used in K_{IC} estimation.

The Charpy and CTOD testing and microstructural investigations have been performed at NTNU in Trondheim, Norway, while the fracture surface investigation has been carried out at UC Berkeley in California, USA.

4.1 Material

A 420 MPa steel plate with chemical composition as given in Table 4.1 has been tested in the experimental work performed.

Table 4.1: *Chemical composition of investigated steel.*

Element	C	Si	Mn	Cu	Ni	Nb
Wt%	0.09	0.19	1.54	0.28	0.7	0.013

4.2 Weld Simulation

Test specimens with microstructures corresponding to the CGHAZ and the ICCGHAZ were produced using thermal weld simulation with a one and two cycle process, respectively. The parameters used are listed in Table 4.2 and shown schematically in Figure 4.1. The CGHAZ microstructure was simulated in a single cycle process using a

Table 4.2: Applied parameters for the thermal weld simulation process.

Cycle	T_p [°C]	$\Delta t_{8/5}$ [s]	$\Delta t_{6/4}$ [s]	Clamp distance [mm]	Uprate limit [°C/s]
1	1350	15	-	21	150
2	780	-	17.4	21	150

T_{p1} of approximately 1350 °C , and a cooling time, $\Delta t_{8/5}$ of approximately 15 seconds. The ICCGHAZ microstructure was simulated in a two cycle process, where the first cycle was performed with the same parameters as for the CGHAZ. During the second cycle, a T_{p2} of approximately 780 °C and a $\Delta t_{6/4}$ of approximately 17.4 seconds was used. A $\Delta t_{8/5}$ was not used for the second cycle, as T_{p2} was below 800 °C. The $\Delta t_{6/4}$ was chosen as to give the same effect as a $\Delta t_{8/5}$ of 15 seconds used in the first cycle. The samples were resistance heated to the respective T_p using an uprate limit of 150 °C/s.

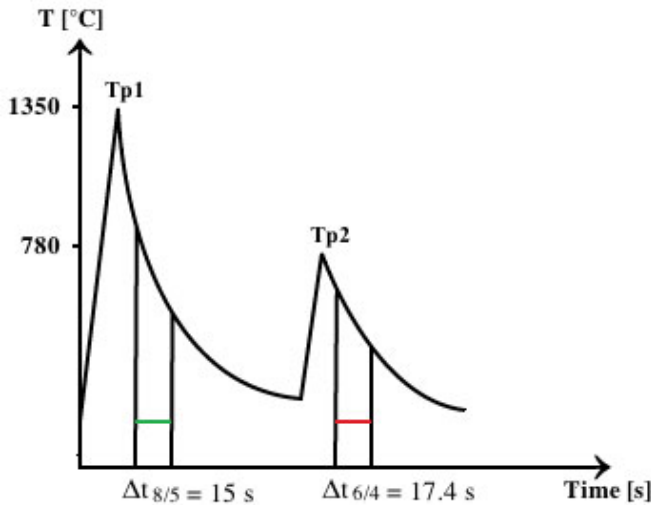


Figure 4.1: Schematic representation of the weld simulation procedure used to simulate the CGHAZ and the ICCGHAZ.

During weld simulation, specimens with 11 · 11 mm² cross section and 100 mm length were used. After weld simulation, machining was performed to produce specimens with standard Charpy dimensions of 55 mm length and 10x10 mm² cross section and CTOD samples of 80 mm length and 10x10 mm² cross section.

4.3 Instrumented Charpy Impact Testing

Instrumented Charpy impact testing was performed on specimens using base material and weld simulated CGHAZ and ICCGHAZ microstructures with both conventional V-notched and fatigue pre-cracked specimens. Each specimen had a standard Charpy geometry with width, height and length of 10 mm, 10 mm and 55 mm respectively. The notch and pre-crack was made through the thickness of the plate (Figure 4.2). The V-notched samples were made with a notch depth of 1.98 mm, while the fatigue pre-cracked specimens were made with an Electro Discharge Machined (EDM)-notch of 1 mm and a fatigue crack of approximately 1 mm. The depth of the final fatigue crack, including the EDM-notch, a_0 , was 1.97 ± 0.09 mm, determined as the average of three measurements along the crack ligament, at 2.5, 5 and 7.5 mm from one of the edges of the specimens.

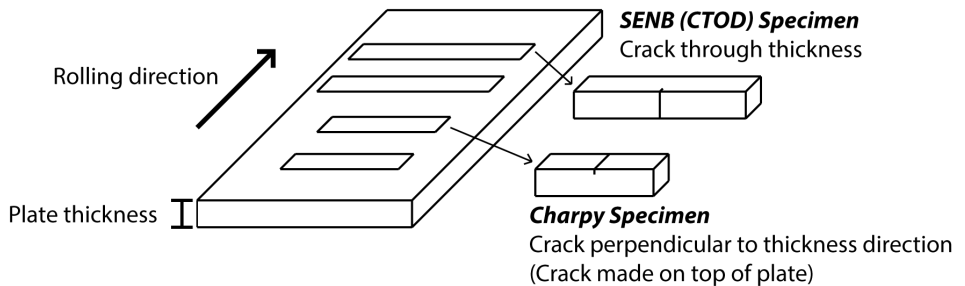


Figure 4.2: Figure illustrating the position of the notch and pre-crack in Charpy and SENB specimens relative to the original steel plate.

Testing was performed according to NS-EN ISO 14556 [73]. The test specimens were cooled down in a bath containing rectified alcohol for tests performed at temperatures above -90 °C and in a chamber with circulating nitrogen gas for tests performed at temperatures below -90 °C. The specimens cooled down in the alcohol bath were immersed in the liquid for 5 minutes, 0.5 minute per mm specimen thickness. When nitrogen gas was used, the specimens were inserted in the chamber for 20, 2 minutes per mm specimen thickness. After sufficient cooling, the specimens were inserted directly into the test machine and tested. The test machine and set-up can be seen in Figure 4.3.



Figure 4.3: Charpy machine and test set-up used during testing [93, 94].

During some of the tests, a Teflon sheet was used between the rolls in the hammer to prevent premature triggering at the lowest test temperatures. Tests where teflon was used is indicated in Appendix A, where data from each of the tests performed is included. One of the tests were also performed using led to prevent excessive oscillations, especially in the beginning of the test.

The measured total energy, C_V , the energy given by the instrumented Charpy instrument, and the load-time history of each test were recorded. The measured C_V values were obtained from the test instrument were multiplied with 1.05, a calibration factor for the specific instrument used. For most of the temperatures, three tests were performed. An overview of the tests performed can be found in Table 4.3.

From the load-time history recorded, load-deflection curves were obtained. Due to oscillations arising from interaction between the instrument striker and the test piece, vibrations were superimposed using a fitted curve through the oscillations according to the standards. The test piece bending displacement was calculated by double integration using Equation (4.1) and (4.2) [73], given an assumed rigid pendulum of effective mass, m , initial impact velocity, v_0 , and the time at the beginning of the deformation, t_0 . Here,

$v(t)$ and $v(t)$ are the pendulum speed and displacement at a given time, t , respectively.

$$v(t) = v_0 - \frac{1}{m} \int_0^t F(t) dt \quad (4.1)$$

$$s(t) = \int_{t_0}^t v(t) dt \quad (4.2)$$

The total energy was, in addition to be measured by the test instrument, calculated as the total area under the load-deflection curve by using Equation (4.3)

$$Energy = C_V = \int_{t_0}^t F(t) \cdot v(t) dt = \int_{s_0}^s F(s) ds \quad (4.3)$$

The total area under the curve is dependent on the measure points included, where the point at where the data is cut determines the final calculated C_V , $C_{V,c}$, obtained. The $C_{V,c}$ has been determined by a cut-off when the load has decreased to a value of 5 % of the maximum load measured, F_m .

In addition to the total energy, the portion of the total energy obtained before the onset of brittle fracture, $C_{V,f}$, the energy obtained up to maximum load, $C_{V,m}$ and the corresponding deflection, s_m , was calculated. These values were estimated by integration up to the point of F_u , the load at brittle fracture initiation and F_m , respectively. For (Class IV and V), F_m equals F_u , so that $C_{V,m}$ is equal to $C_{V,f}$. For tests where the fracture path was shown to be fully ductile (class I), $C_{V,m}$ has been set equal to $C_{V,f}$, as brittle fracture initiation does not occur.

The fraction of energy calculated before brittle fracture initiation, $C_{V,f}$, of the total calculated energy, $C_{V,c}$ was calculated.

It should be noted that oscillations may influence the final result when estimating $C_{V,c}$ and $C_{V,f}$ values from the area under the load-deflection curve.

All data obtained for all of the instrumented Charpy tests performed are included in Appendix A.

4.4 Transition Curves

From the measured C_V values, Charpy-transition curves were constructed using average C_V values calculated at each test temperature. A trend line using a moving average of period two was included between the data points at each test temperature to indicate the shape of the curve, and error bars showing the standard deviation was added to include the scatter in the measured data. The transition curves can be seen in the result section, Section 5.3.

Table 4.3: Charpy test performed.

Microstructure	Flaw Geometry	Temperature °C	Tests Performed
Base material	Notch	-30	3
		-60	3
		-90	3
		-120	3
		-137	3
		-155	4
Base material	Pre-crack	-30	3
		-60	3
		-75	3
		-82	6
		-90	3
		-120	3
CGHAZ	Notch	23	3
		0	3
		-15	3
		-30	3
		-45	3
		-60	3
CGHAZ	Pre-crack	23	3
		11	3
		0	3
		-30	3
		-60	4
ICCGHAZ	Notch	23	3
		0	3
		-30	2
		-60	3
ICCGHAZ	Pre-crack	23	3
		0	3
		-30	2
		-60	3

4.5 CTOD Testing

CTOD testing was performed on both weld simulated CGHAZ and ICCGHAZ specimens with a cross section of $10 \cdot 10 \text{ mm}^2$ and a length of 80 mm. A SENB specimen configuration with an initial crack depth, a_0 of 5 mm was used. The initial crack was made with a 3.5 mm deep EDM-notch followed by a 1.5 mm fatigue pre-crack, machined according to BS7448 [95]. The crack was made on top of the plate, perpendicular to the plate thickness (Figure 4.2).

The specimens were cooled down to the different test temperatures in a chamber with circulating nitrogen gas. As for the Charpy specimens, the specimens were inserted in the chamber for 20 minutes, 2 minutes per mm specimen thickness. The tests were performed directly after sufficient cooling was performed. Table 4.4 gives an overview of the number of samples tested at the different test temperatures.

Table 4.4: *CTOD test performed.*

Microstructure	Temperature °C	Tests Performed
CGHAZ	0	10
	-30	10
	-60	10
	-90	10
ICCGHAZ	0	10
	-30	10
	-60	10
	-90	9

4.6 Microstructural Investigation

Three specimens, one for each of the microstructures investigated (base material, CGHAZ and ICCGHAZ) were studied in an optical light microscope. The samples were cut to approximately 10x10 mm² pieces before surface preparation and imaging was performed.

4.6.1 Moulding and Specimen Preparation

The samples were embedded in moulds of 30 mm diameter for better grip during grinding and polishing. The moulds were greased with high vacuum silicon grease before being filled with epoxy. *Struers EpoFix* was used, made by mixing a weight ratio of 25 parts resin and three parts hardener. The mixture was stirred for two minutes before the moulds with the samples were filled and the moulds were set to cure.

Surface preparation was carried out on the three samples simultaneously by using automated machines. Grinding was performed using an automated *Struers RotoForce-4* machine, while polishing was carried out using a *Struers TegraPol-31* machine. In the grinding process, silicon carbide (SiC) grinding paper with decreasing roughness were used. Polishing with decreasing roughness was performed subsequently in a three step procedure, first using an abrasive disk before two Diamond Paste (DP) abrasives with decreasing roughness were used.

The grinding papers and polishing equipment used are listed in Table 4.5 together with the grinding and polishing sequence performed. After grinding and polishing, one base material, CGHAZ and ICCGHAZ specimen were etched with 2 % Nital and LaPera etchants.

Table 4.5: Sample preparation sequence for investigation in OLM. All equipment from Struers.

<i>Grinding</i>			
Step	Equipment	Grit number	Time
1	Struers SiC paper	80	2.5 min
2	Struers SiC paper	320	2.5 min
3	Struers SiC paper	500	2.5 min
4	Struers SiC paper	1200	2.5 min
5	Struers SiC paper	2000	2.5 min
<i>Polishing</i>			
Step	Equipment	Roughness	Time
1	MD Allegro grinding disk	9 μ m	5 min
2	MD Mol Cloth and DP products	3 μ m	5 min
3	MD Nap Cloth and DP products	1 μ m	5 min

4.6.2 Etching

The following etching procedures were used:

1. 2 % Nital

Etching with 2 % Nital (%HNO₃ and 98 % C₂H₅OH) was performed by immersing the samples in the liquid for 12 seconds followed by rinsing the samples with ethanol and drying in hot air immediately after etching was performed. When using Nital, the ferrite appears white, ferrite grain boundaries dark, while martensite gets a brown tint in the microscope.

2. LaPera

The LaPera etchant was made by mixing the following two solutions in a 1:1 proportion [54]:

- (a) 1 g sodium meta-bi-sulphite (Na₂S₂O₅) 100 mL distilled water
- (b) 4 g picric acid 100 mL pure ethanol.

To better reveal possible MA constituents present, the samples were also etched with LaPera reagent. The samples were immersed for 20 seconds in the etchant before they were cleaned with ethanol and dried with hot air. MA constituents and carbides becomes white in the microscope when etched with LaPera reagent, while the ferrite becomes dark [96].

4.6.3 Imaging

A *Leica MeF4M* microscope attached to a *JENOPTIK ProgRes C10 plus* digital camera and a computer with the image processing program *ImageAccess EasyLab* was utilized to acquire images of the samples etched with Nital. A *Leica DMI 5000 M* with a *CTR 6000* electronic box and image program *Leica Application Suite LAS V3.8* was used when imaging the samples etched with LaPera. Micrographs were taken within a distance of 1 mm away from the fracture surface, as illustrated in Figure 4.4, with 50X and 100X objectives.

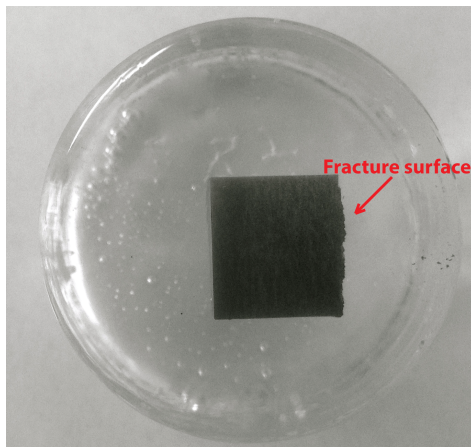


Figure 4.4: *Sample studied in OLM. Fracture surface is seen to the right.*

4.7 Fracture Surface Investigation

The fracture surfaces of four CGHAZ and five ICCGHAZ weld simulated samples were studied in a *FEI Nova NanoSEM 650* microscope. The investigated samples were chosen based on their lower shelf C_V values. A list of the investigated samples can be seen in Table 4.6 and shown in Figure 4.5. The samples were cleaned in acetone prior to examination. The samples were investigated using secondary electron imaging with 2.5 kV acceleration voltage and a spot size of 1.5. The working distance varied between 3.4 mm and 5.6 mm. The fracture surfaces were studied close to the notch or the fatigue pre-crack. All the samples are studied and imaged with the pre-crack or notch facing up in the micrographs.

Table 4.6: *The samples investigated in SEM.*

Microstructure	Name	Flaw Geometry	Temperature	Curve Class
CGHAZ	ss4c	Notch	-30 °C	III
	ss7c	Notch	-60 °C	IV
	ss30f	Pre-crack	0 °C	V
	ss27f	Pre-crack	-30 °C	V
ICCGHAZ	ss2.104c	Notch	-30 °C	IV
	ss2.106c	Notch	-60 °C	IV
	ss2.79f	Pre-crack	0 °C	V
	ss2.82f	Pre-crack	-30 °C	V
	ss2.87f	Pre-crack	-60 °C	V

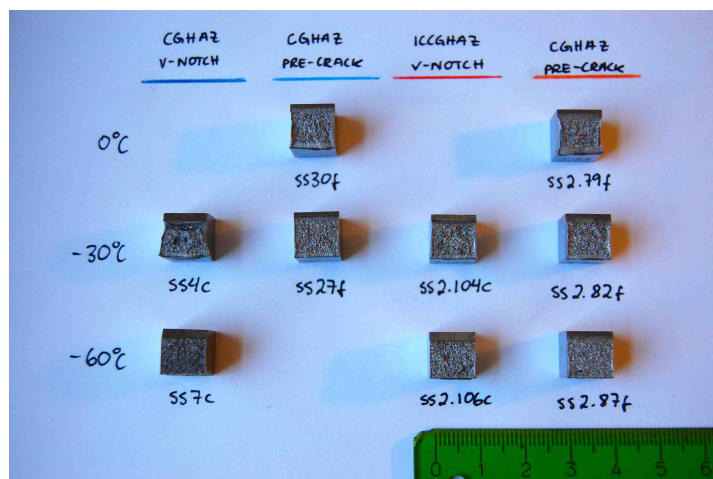


Figure 4.5: *Fracture specimens investigated in a SEM.*

4.8 Correlations Used to Estimate CTOD Values from Data Obtained During Charpy testing

Two different correlation approaches, both developed for lower transitional and lower shelf behaviour, were tested to investigate the correlativity between CTOD values and C_V values obtained during instrumented Charpy testing. The tested correlations are (1) the lower bound relation for lower shelf and lower transitional behaviour after BS7910 (presented in section 4.8.1) and (2) the correlation for lower shelf transitional behaviour based on the Master Curve (MC) (presented in section 4.8.2) included in both ASTM E1921 and BS7910. The correlation based on the MC can be used if Charpy transition curve data is available, while the lower bound relation can be used if Charpy transition curve data is unavailable, but Charpy-data at the service temperature exist.

The two procedures are outlined below. Both standards include equations to estimate fracture toughness values, given as K_{JC} in ASTM E1921 and K_{mat} in BS7910. These values have been converted to CTOD values in order to compare the estimates to data obtained during CTOD testing.

The two correlations were tested using CGHAZ and ICCGHAZ microstructures to evaluate how well the relations might predict CTOD values for these microstructures, although the range of applicability of the MC is limited to macroscopically homogeneous steels with uniform tensile and toughness properties [91]. The thickness value, B , was set to 10 mm, the actual thickness of both the CTOD and the Charpy specimens used during testing, in both of the correlation calculations.

4.8.1 Lower Bound Relation for Lower Shelf and Lower Transitional Behaviour According to BS7910

The fracture toughness, K_{mat} , of ferritic steels at the service temperature can be estimated from Charpy results according to Equation (4.4) given in BS7910, Annex J.2.1 [66].

$$K_{mat} = \left[\left(12\sqrt{C_V} - 20 \right) \left(\frac{25}{B} \right)^{0.25} \right] + 20 \quad (4.4)$$

where

K_{mat} is the estimated toughness in $\text{MPa}\sqrt{\text{m}}$,

B is the thickness of the material for which an estimate of K_{mat} is required in mm and

C_V is the lower bound Charpy V-notch impact energy at the service temperature in J.

The B -term in Equation (4.7) corrects for the difference in size between the Charpy and conventional CTOD test specimens.

CTOD values were calculated from the estimated K_{mat} values using Equation (2.9) in Section 2.8 (also given in Equation (4.9) below).

4.8.2 Lower Shelf Transitional Behaviour Based on the Master Curve

The fracture toughness was also estimated using the Master Curve (MC) according to BS7910, Annex J.2.2 [66] and ASTM E1921 [90]. The following steps were used in obtaining a CTOD estimate using the MC.

1. Determination of T_{CV27J}

The temperatures at a C_V value of 27J, T_{CV27J} , were estimated from the Charpy transition curves obtained from test data (Figure 5.1 presented in Section 5.3). The temperature was determined by finding the temperature corresponding to a C_V of 27 J on the Charpy transition curves formed using trend lines with a moving average of period two between the points at each test temperature.

2. Estimation of the Transition Temperature, T_0

The reference temperature, T_0 was estimated using the following equation,

$$T_0 = T_{CV28J} - C \quad (4.5)$$

According to ASTM E1921 [90] and BS7910 [66], C should be 18 for notched specimens, while for pre-cracked specimens, a C of 50 should be used according to ASTM E1921[90]. In ASTM E1921, the temperature estimated in Equation (4.5) is used to estimate a start temperature when estimating T_0 from quasi-static fracture mechanical testing, while it is used directly as an estimate of T_0 in BS7910, and has been used for this purpose in the present master's thesis.

In addition to Equation (4.5) Wallin has developed an alternative equation that can be used in estimating T_0 . This equation, given in Equation (4.6) [26] uses the upper shelf C_V value, C_{V-US} , in addition to the yield strength and T_{CV28J} value and is developed for both Single Edge Notch Bend (SENB), and Compact Tension (CT) specimens. Equation (4.6) is the version developed for SENB specimens, the specimen test configuration used during testing of the materials in this master's thesis.

Equation (4.6) was used in addition to Equation (4.5), as the BS7910 and ASTM E1921 are not in accordance when it comes to what Equation (4.5) primarily is used for, and the

4.8. Correlations Used to Estimate CTOD Values from Data Obtained During Charpy testing

determination of T_0 from Charpy data is not very well defined by other means. Equation (4.6) is presented below as it appears in [26].

$$T_{0-Est-SE(B)} \approx T_{CV28J} - 87^\circ\text{C} + \frac{\sigma_Y}{12\text{MPa}^\circ\text{C}^{-1}} + \frac{1000\text{J}^\circ\text{C}}{C_{V-US}} \quad (4.6)$$

A C_{V-US} of 220 J was used in the calculations. A fixed upper-shelf value was used for all of the tested microstructures, as some of test parallels do not reach upper shelf values. For the curves where C_{V-US} values were obtained, the upper shelf lies at about 270 J for the base material and 220 J for the CGHAZ curve. The lowest value, 220 J, was used in the calculations, as this is the upper shelf for the weld-simulated materials that are investigated.

3. Estimation of K_{mat}

K_{mat} was estimated using the equation given in BS7910 presented below. In ASTM E1921, the thickness correction term is included as a separate formula that when included in the main equation provides the same equation as Equation 4.7.

$$K_{mat} = 20 + \left[11 + 77e^{\{0.019(T-T_0-T_k)\}} \right] \left(\frac{25}{B} \right)^{\frac{1}{4}} \left\{ \ln \left(\frac{1}{1-P_f} \right) \right\}^{\frac{1}{4}} \quad (4.7)$$

where

- T is the temperature where K_{mat} is to be determined in $^\circ\text{C}$,
- T_0 is the transition temperature in $^\circ\text{C}$ estimated from Equation (4.5),
- T_k is a temperature term describing the scatter in the correlation between Charpy and fracture toughness values. At a SD of 15°C and 90% confidence level, T_k is set to 25, although lower values can be used if supported by experimental data,
- B is the thickness of the material in mm for which an estimate of K_{mat} is required and

P_f is after BS 7910 the probability of K_{mat} being less than estimated [66], and by ASTM E1921 the probability that a single selected specimen chosen at random from a population of specimens will fail at or before reaching the K_{JC} (same as K_{mat} in BS7910) value of interest [90]. A P_f of 0.05 (5%) is recommended by ASTM, unless experimental evidence supports the use of higher probability for a given material.

When having calculated values from step 1 through step 3, Equation (2.9) (also given in Equation (4.9) below) was used to estimate the corresponding CTOD values.

It should be noted that T_k is included in BS7910, while the parameter is not used in ASTM E1921. T_k has been included in the calculations performed in this master's thesis in order to evaluate the effect of this scatter correction parameter.

4.8.3 Validity limits

In order to avoid overestimating the fracture toughness at the service temperature in materials with potentially low C_{V-US} value, an upper limit for K_{mat} is given in BS7910 Annex J.2.3, where the estimated K_{mat} should not exceed the value given by Equation (4.8). This equation applies when K_{mat} is estimated using the lower bound relation given in Equation (4.4) and the MC given in Equation (4.7), and was used in order to evaluate the estimated values obtained from the correlations.

$$K_{mat} = 0.54C_V + 55 \quad (4.8)$$

4.8.4 Procedure to Convert Fracture Toughness to CTOD

CTOD values were obtained using Equation (2.9) [22, 23, 65, 66] given in Section 2.8, assuming plane strain conditions. The equation is repeated below in Equation (4.9).

$$CTOD = \frac{K^2}{\lambda \sigma_Y E'} \quad (4.9)$$

$E' = \frac{E}{(1-\nu^2)}$, $\lambda = 1$ and $E' = E$, $\lambda = 2$ at plane strain and plane stress respectively. As fracture mechanical tests specimens are usually tested in plane strain to provide a lower

bound toughness estimate, the estimates were calculated assuming plane strain conditions. However, a λ value of 1.5 was used, as this value is believed to provide a better fit to the materials investigated [97]. A Young's modulus, E , of 200 GPa, a Poisson's ratio, ν , of 0.3 and a lower yield strength, σ_Y , of 420 MPa were used in the calculations.

4.8.5 Procedure and Parameters Used in Evaluating the Degree of Correlation of the two Investigated Methods

The results from the CTOD calculations using the two correlations were plotted against the real measured CTOD values to allow for evaluation of the degree of correlation of the methods. Average measured C_V values were used in the calculations. This was done as it has been of interest to study how well the correlations predict fracture mechanical test parameters from Charpy data for the specific the microstructures investigated, and not to perform structural assessment evaluations. Average values were considered to provide a good picture of the degree of correlation of the investigated methods. In addition, the scatter is large at some test temperatures, at least for some of the tested microstructures. Therefore, using average values are considered to provide a general image of the degree of correlation.

The value of B was set to 10 mm, the actual thickness of both the CTOD and the Charpy specimens used during testing, in both of the correlation calculations. For the lower bound relation after BS7910, error bars showing the SD obtained during CTOD testing were included.

For the correlation using the MC the T_0 estimated with the different equations was used in order to take a closer look on how this influenced the degree of correlation. For the notched and pre-cracked specimens, a C of 18 and 50 was used in Equation 4.5, respectively. The determination and use of the value of the parameter T_k in Equation 4.7 is not well defined and it was therefore changed in order to be able to say something about how this parameter influence the degree of correlation. The P_f was set to 0.02, 0.632 and 0.98, where the curves with P_f set to 0.02 and 0.98 represent the validity limits for the estimated CTOD values. The curve using a P_f of 0.632 represent a median estimate of the CTOD. Data falling below the 2 % or above the 98 % confidence limit curves are invalid and may indicate material inhomogeneity [91].

5 Results

In this chapter, the results obtained from tests and calculations performed are presented. Results from instrumented Charpy testing and quasi-static CTOD testing are included. Different parameters obtained from the instrumented Charpy test have been processed and are presented both in numbers and graphically. In addition results from estimating CTOD values from Charpy data from two correlations, the lower bound correlation from BS7910 and the Master Curve correlation are presented. Micrographs from both fracture surface investigations of Charpy specimens and microstructural investigations are included. Also, calculations from weldability evaluations of the investigated steel is presented.

5.1 Estimated Carbon Equivalent

The weldability of the given steel has been evaluated using the Ito–Bessyo formula for the Parameter of Crack Measurement (PCM) given in Equation (2.5), and the Carbon Equivalent (CE) formula given in Equation (2.4). As the steel is a low alloy steel with a carbon content below 18 wt%, the PCM is believed to give the most accurate estimate of the weldability, as mentioned in Section 2.6.1.

$$PCM = 0.09 + \frac{0.19}{30} + \left(\frac{1.54 + 0.28}{20} \right) + \frac{0.7}{60} = \underline{\underline{0.199}} \text{ [wt\%]} \quad (5.1)$$

The CE formula given in Equation (2.4) gives the following result:

$$CE = 0.09 + \frac{1.54}{6} + \left(\frac{0.7 + 0.28}{15} \right) = \underline{\underline{0.412}} \text{ [wt\%]} \quad (5.2)$$

As the calculated PCM value is below 0.27, the steel is considered to be weldable. Using IIW's CE formula, the calculated CE is below 0.45, also indicating that the steel can be considered to be weldable.

5.2 Results from Instrumented Charpy Testing

The average measured C_V values are included in Table 5.1 together with the calculated Standard Deviation (SD) and Relative Standard Deviation (RSD). Data for all of the tests performed can be found in Appendix A.

Table 5.1: Average measured C_V values from instrumented Charpy testing with SD and RSD.

Microstructure	Flaw geometry	T [°C]	Average C_V [J]	SD	RSD [%]	No. of tests	
Base material	<i>V-notch</i>	-30	264.0	0.5	0.2	3	
		-60	258.3	4.3	1.7	3	
		-90	253.4	9.6	3.8	3	
		-120	209.9	20.7	9.9	3	
		-137	16.4	3.0	18.4	3	
		-155	10.0	4.1	40.8	4	
	<i>Pre-crack</i>	-30	284.5	8.2	2.9	3	
		-60	242.9	7.5	3.1	3	
		-75	239.3	20.9	8.7	3	
		-82	83.8	82.5	98.5	6	
		-90	25.4	4.6	18.0	3	
		-120	4.1	1.2	29.3	3	
	CGHAZ	<i>V-notch</i>	23	212.5	3.6	1.7	3
			0	209.4	21.0	10.0	3
-15			135.3	27.1	20.1	3	
-30			85.6	45.7	53.4	3	
-45			66.8	12.2	18.3	3	
-60			8.5	2.6	30.7	3	
<i>Pre-crack</i>		23	227.1	7.1	3.1	3	
		11	128.2	55.3	43.2	3	
		0	33.1	4.8	14.5	3	
		-30	12.9	0.4	3.2	3	
		-60	6.2	0.7	11.5	4	
		ICCGHAZ	<i>V-notch</i>	23	207.7	4.7	2.2
0				144.0	34.6	24.1	3
-30				45.3	9.8	21.6	2
-60	12.2			1.9	15.9	3	
<i>Pre-crack</i>	23		76.1	2.8	3.6	3	
	0		45.8	1.9	4.2	3	
	-30		20.9	2.8	3.6	2	
	-60		9.2	2.1	22.3	3	

5.3 Transition Curves From Instrumented Charpy Test Data

The transition curves obtained from energy C_V values measured during instrumented Charpy testing can be seen in Figure 5.1. The curves have been obtained using the average measured C_V values of the parallel tests performed at each test temperature for the six combinations of flaw geometry and microstructure. The Standard Deviation (SD) is included, and can be seen as error bars in the graph. Curves for both pre-cracked and conventional V-notched series are shown. All test data as well as the SD and RSD are included in Appendix A. It is to be noted that only three samples have been tested at most of the test temperatures, whereas the six to eight parallel tests are required in K_{JC} testing according to ASTM E1921 [90], depending on the test temperature.

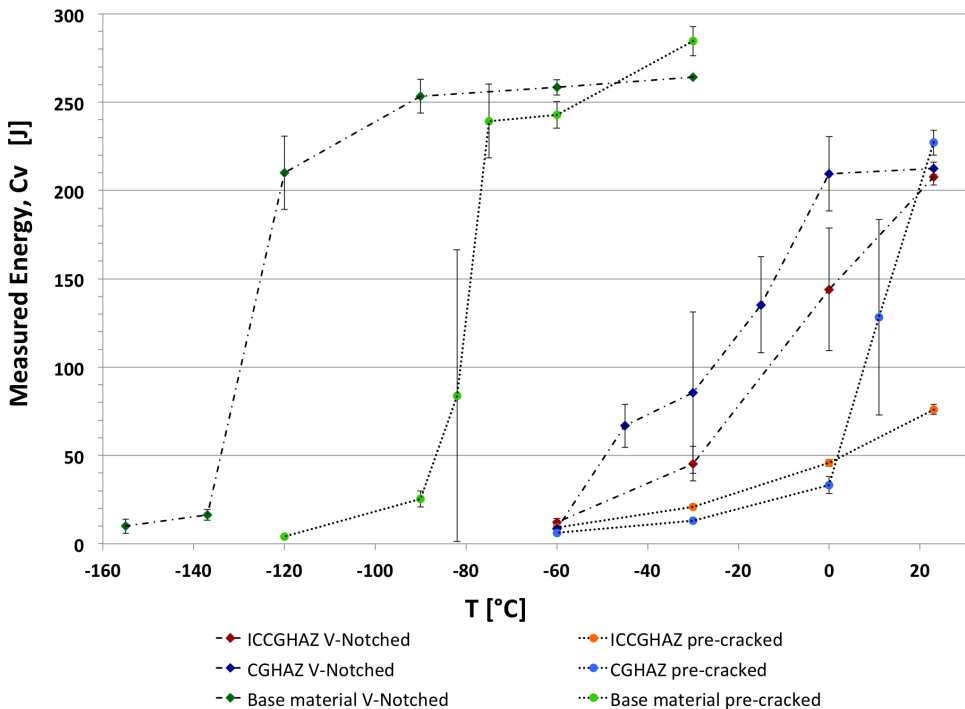


Figure 5.1: Charpy transition curves obtained from measured energies, C_V . Base material (green), weld simulated CGHAZ (blue) and ICCGHAZ (red). Notched series have diamond shaped points and long-dotted lines, notched series have circular points and finer dotted lines.

A transition curve using strictly lower bound values at each test temperature has also been generated, shown in Figure 5.2. It can be seen that the curves using lower bound values and average values are similar.

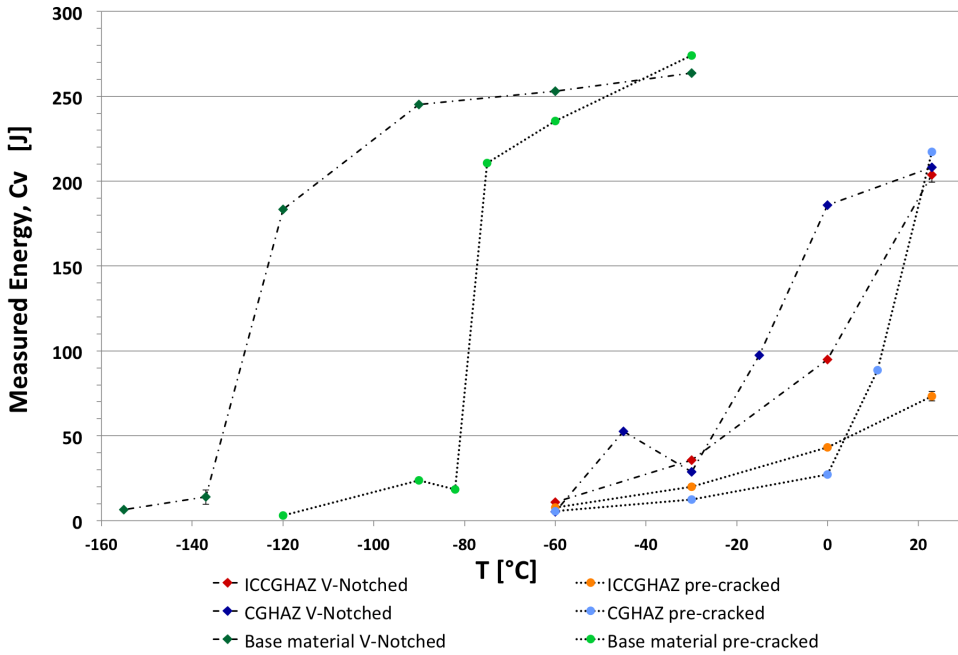


Figure 5.2: Charpy transition curve obtained using lower bound C_V values. Same labelling as in Figure 5.1.

The curves in Figure 5.1 show a clear shift in transition temperature from the base material to the weld simulated CGHAZ and ICCGHAZ. It can also be seen that the transition region is shifted to higher temperature values for the pre-cracked parallels compared to the curves obtained using notched specimens. This is the case for the three microstructures tested. If the transition temperature, T_{trans} , is taken as the temperature in the middle of the transition region, the transition temperatures for the base material can roughly be estimated to be $-130\text{ }^\circ\text{C}$ and $-75\text{ }^\circ\text{C}$ for the V-notched and pre-cracked series, respectively. The corresponding values are approximately $-15\text{ }^\circ\text{C}$ and $10\text{ }^\circ\text{C}$ for the V-notched and pre-cracked CGHAZ parallels, respectively. This shows that the curves has shifted by about $55\text{ }^\circ\text{C}$ for the base material and $25\text{ }^\circ\text{C}$ for the CGHAZ in the transition region by changing the notch sharpness.

The T_{trans} for the pre-cracked ICCGHAZ series can not be determined graphically, as the upper-shelf is not reached. However, if it is assumed that the upper shelf C_V values are approximately the same for ICCGHAZ and CGHAZ, the T_{trans} of the ICCGHAZ curves would have been about 0 °C for the V-notched series, while an estimate of T_{trans} for the pre-cracked series is harder to make, as it appears as though the transition region is not reached in this curve, and the slope of the transition region is unknown.

In addition to increased transition temperature, the curves show a steeper slope within the transition region for the base material compared with the CGHAZ and ICCGHAZ curves for both notched and pre-cracked specimens. It can also be seen that the energy measured at the lowest temperature for the six parallels are comparable. The upper shelf seems to be reached at lower measured energy values when weld-simulated microstructures have been tested. The two ICCGHAZ series together with the pre-cracked CGHAZ series do not seem to reach upper shelf values.

The SD is seen to be large for certain temperatures, generally within the transition range. The SD is seen to be small at the lower shelf for all the six combination of notch configuration and microstructure and is generally smaller for the pre-cracked CGHAZ and ICCGHAZ series compared with the notched series for these microstructures. For the CGHAZ series, the data scatter was found to be largest at -30 °C with a SD and RSD of 45.7 and 53.4% respectively for the notched series, and at 11 °C with a SD and RSD of 55.3 and 43.2% respectively for the pre-cracked series.

For the ICCGHAZ series the largest data scatter was observed at 0 °C with a SD and RSD of 34.6 and 24.1% respectively for the notched ICCGHAZ series. The pre-cracked series does not show one temperature with significant deviation compared to the other curves. Here, the largest data scatter is observed at 0 °C with a SD of 2,1 and a RSD of 22.3%. The SD and RSD are calculated for all test temperatures, and are included in Appendix A, while average data was presented in Table 5.1.

5.4 Charpy Energies and Curve Classes

The load–deflection curves recorded during the instrumented Charpy tests are all included in Appendix C. The location of the different curve classes on the Charpy transition curve can be seen in Figure 3.6. Most of the generated curves are of the lower curve classes, especially when testing weld microstructures. Generally, lower curve classes are obtained during testing at higher temperatures. A general trend can be observed in that higher curve classes and more brittle behaviour become more predominant with an increasing number of weld passes and increasing flaw sharpness.

In the ICCGHAZ microstructure specimens containing a pre-crack, the class V curve is the only curve class obtained during testing, while for specimens containing a notch, curve class IV are predominant at lower temperatures and class II and III at higher temperatures. For pre-cracked specimens with a CGHAZ microstructure, class V are obtained for the lowest test temperatures, while some curves of higher classes are obtained for the higher test temperatures.

For notched CGHAZ specimens, class IV curves are obtained for the lowest test temperatures, while curve class II and III occur when the test temperature is increased. When testing samples of the base material microstructure, class V curves were obtained at the lowest test temperatures Class I are obtained at the highest test temperatures for pre-cracked specimens. For notched base material specimens, curves of class I are obtained at the highest test temperatures, while curves of class IV are obtained at the lower test temperatures.

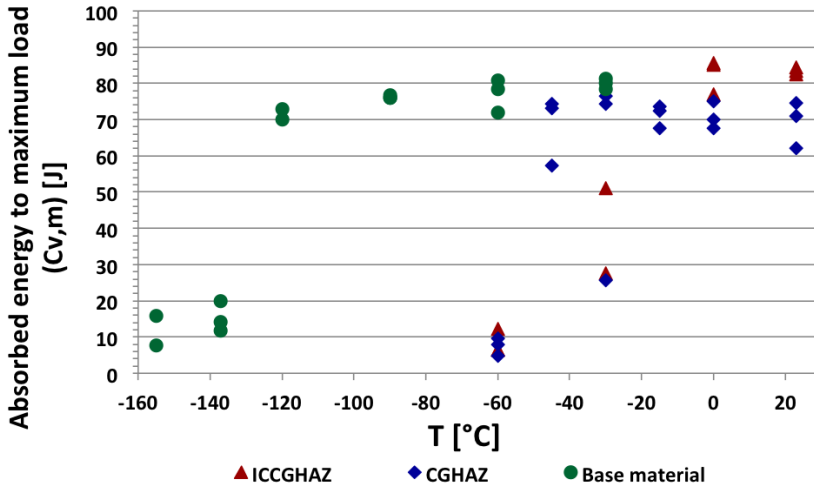
5.4.1 Charpy Energies Absorbed Before Maximum Load and Brittle Fracture Initiation

The calculated value of the absorbed energy up to maximum load, $C_{V,m}$, and to the onset of brittle fracture initiation, $C_{V,f}$ have been plotted against temperature in 5.3 and 5.4. $C_{V,m}$ equals $C_{V,f}$ for curve class IV and V. For both values, a separate plot showing the distribution of the parameters with temperature is given for the notched and pre-cracked parallels.

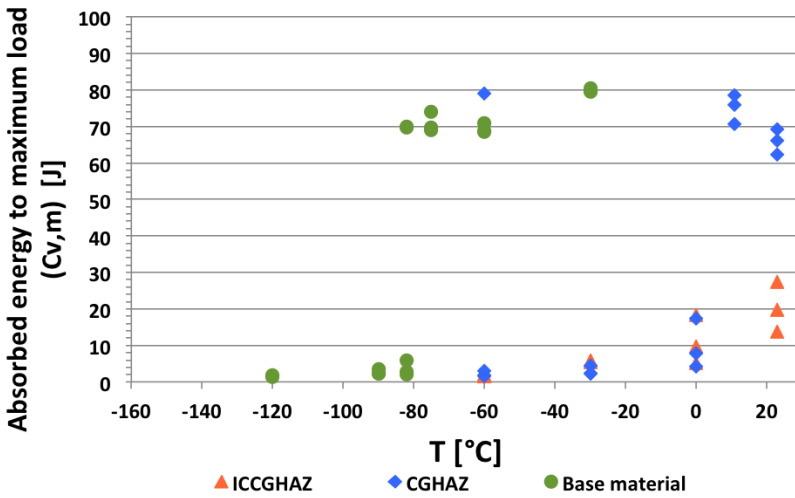
It can be seen that the highest $C_{V,m}$ values are comparable for the three microstructures tested both when notched and pre-cracked specimens are used. The lowest values obtained are somewhat lower for the pre-cracked series compared to the notched series. For the base material, high $C_{V,m}$ values are obtained for one or several parallel tests at most of the test temperatures. At the lowest temperatures the $C_{V,m}$ values are seen to be low for several tests.

For the CGHAZ microstructure tested, most of the tests using notched specimens show high $C_{V,m}$ values. A larger amount of tests have lower $C_{V,m}$ values when pre-cracked specimens are used. The lower values are obtained at the lowest test temperatures for this microstructure as well. The $C_{V,m}$ values obtained from testing of the ICCGHAZ microstructure are low for all tests performed using pre-cracked specimens. For the notched series, the ICCGHAZ series behaves almost like the CGHAZ series with high $C_{V,m}$ values at the highest test temperatures and some lower values at the lowest test temperatures.

The $C_{V,f}$ values are seen to increase with temperature, where the transition from low values occurs more abruptly in the plot showing values obtained using pre-cracked specimens. The values are seen to be more scattered for the notched series compared to pre-cracked series, especially evident for the CGHAZ microstructure. In the $C_{V,f}$ -plots, the curve class I values have been excluded, as these curves show a fully ductile fracture path. It can be seen that the distribution of $C_{V,f}$ values is quite similar to the distribution of $C_{V,m}$ values, but the values show a more pronounced increase with test temperature. In addition, either high or low values obtained at each test temperature.

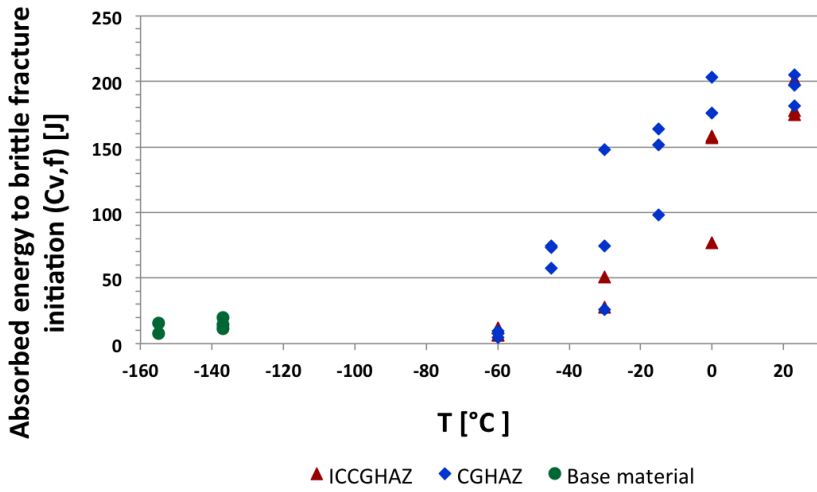


(a) With V-notch

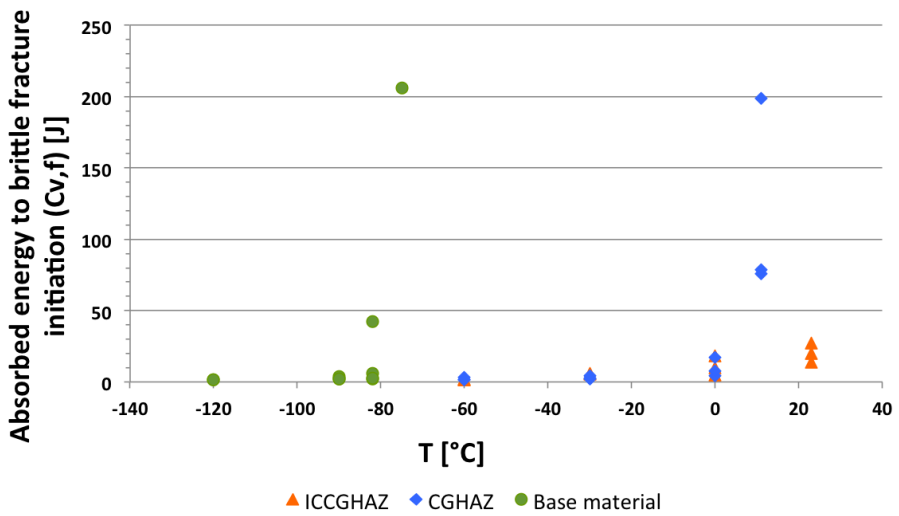


(b) With pre-crack

Figure 5.3: Distribution of $C_{V,m}$ as a function of test temperature for (a) V-notched series and (b) pre-cracked series for base material (green), weld simulated CGHAZ (blue) and ICCGAZ (red) microstructures.



(a) With V-notch



(b) With pre-crack

Figure 5.4: Distribution of $C_{V,f}$ as a function of test temperature for (a) V-notched series and (b) pre-cracked series for base material (green), weld simulated CGHAZ (blue) and ICCGHAZ (red) microstructures.

5.4.2 Charpy Energy Fractions

The ratio between the total calculated energy, $C_{V,c}$ and the energies measured before the onset of brittle fracture initiation, $C_{V,f}$, and before maximum load was reached, $C_{V,m}$, estimated for the different curve classes are presented in this section.

The values have been separated into values obtained using notched and pre-cracked specimens. The average values of $\frac{C_{V,m}}{C_{V,c}}$ and $\frac{C_{V,f}}{C_{V,c}}$ obtained are included below in Table 5.2. The table includes the number of curves obtained used in calculating the average values for each of the curve classes. These values are presented graphically as a function of curve class number in Figure 5.5 (a) for (b) for $\frac{C_{V,m}}{C_{V,c}}$ and $\frac{C_{V,f}}{C_{V,c}}$, respectively. In addition, all of the $\frac{C_{V,m}}{C_{V,c}}$ values are included in the table of all data obtained during instrumented Charpy testing in Appendix A.

It should be noted that only the class II and III curves have different $C_{V,m}$ and $C_{V,f}$ values. Therefore, the $\frac{C_{V,m}}{C_{V,c}}$ and $\frac{C_{V,f}}{C_{V,c}}$ fractions are identical for the other curve classes. In addition, the $\frac{C_{V,f}}{C_{V,c}}$ fractions does not include class I curves, as a $C_{V,f}$ value cannot be determined for these curves due to fully ductile behaviour.

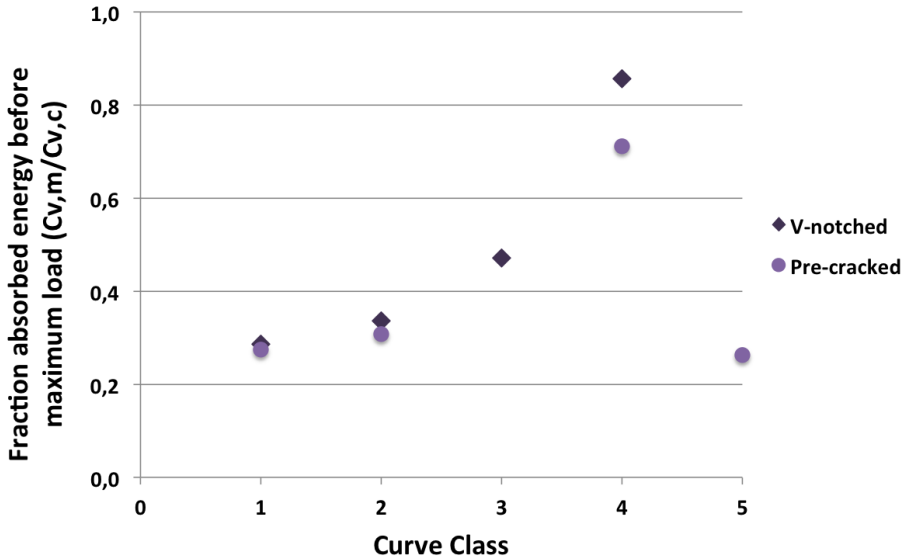
In Figure 5.6 (a) and (b), the distribution of the fraction $\frac{C_{V,m}}{C_{V,c}}$ among the six combinations of microstructure and flaw geometry are plotted against temperature. Figure (a) and (b) show the distribution of $\frac{C_{V,f}}{C_{V,c}}$ among the notched and pre-cracked specimens, respectively.

Table 5.2: Fraction of energy calculated up to maximum load, F_m and load at brittle fracture initiation, F_u for the different curve classes. Some of the curves have been hard to classify.

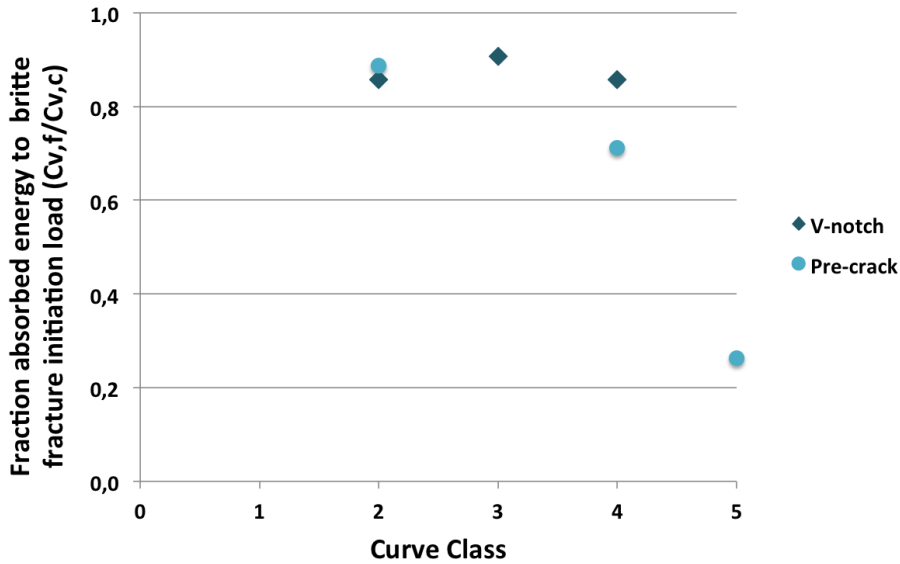
		Energy to maximum load			Energy to brittle initiation		
Curve class	No. of curves	$\frac{C_{V,m}}{C_{V,c}}$	SD	RSD [%]	$\frac{C_{V,f}}{C_V}$	SD	RSD [%]
Notched specimens							
Class I	12	0.287	±0.029	10.0	No brittle initiation		
Class II	7	0.336	±0.029	8.7	0.865	±0.047	5.4
Class III	7	0.472	±0.077	16.3	0.906	±0.038	4.4
Class IV	19	0.857	±0.081	9.4	Same as $\frac{C_{V,m}}{C_{V,c}}$, as $F_m = F_u$		
Class V	0	No class V obtained			No class V obtained		
Pre-cracked specimens							
Class I	13	0.274	±0.043	15.6	No brittle initiation		
Class II	2	0.308	±0.005	1.7	0.887	±0.005	0.6
Class III	0	No class III obtained			No class III obtained		
Class IV	5	0.712	±0.190	26.7	Same as $\frac{C_{V,m}}{C_{V,c}}$, as $F_m = F_u$		
Class V	25	0.262	±0.138	52.8	Same as $\frac{C_{V,m}}{C_{V,c}}$, as $F_m = F_u$		

From Table 5.2 and Figure 5.5, where the results in Table 5.2 are presented graphically, it can be seen that the $\frac{C_{V,m}}{C_{V,c}}$ values increase with curve class number I to IV, and are low for the class V curves. The general trend for the $\frac{C_{V,f}}{C_{V,c}}$ values are higher values for curve class II, III and IV and low values for the class V curves. The SD is seen to be quite large for some of the estimates, especially for the pre-cracked specimens of higher curve classes. It can also be seen that the $\frac{C_{V,f}}{C_{V,c}}$ values are generally high for the class II and III curves, where the $\frac{C_{V,m}}{C_{V,c}}$ and $\frac{C_{V,f}}{C_{V,c}}$ values are dissimilar, as $F_m \neq F_u$.

It can be seen that the increase in $\frac{C_{V,m}}{C_{V,c}}$ values with curve class (Figure 5.5) resembles the increase in CTOD values measured with temperature, included in Figure 5.8 in the following section (Section 5.5).

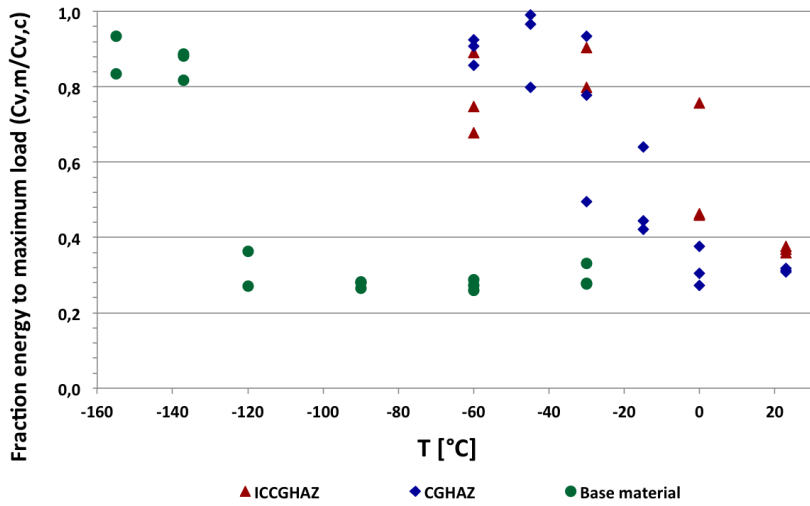


(a) Fraction absorbed energy to maximum load, $\frac{C_{V,m}}{C_{V,c}}$. No class III curves obtained for the pre-cracked series, no class V curves obtained for the notched series.

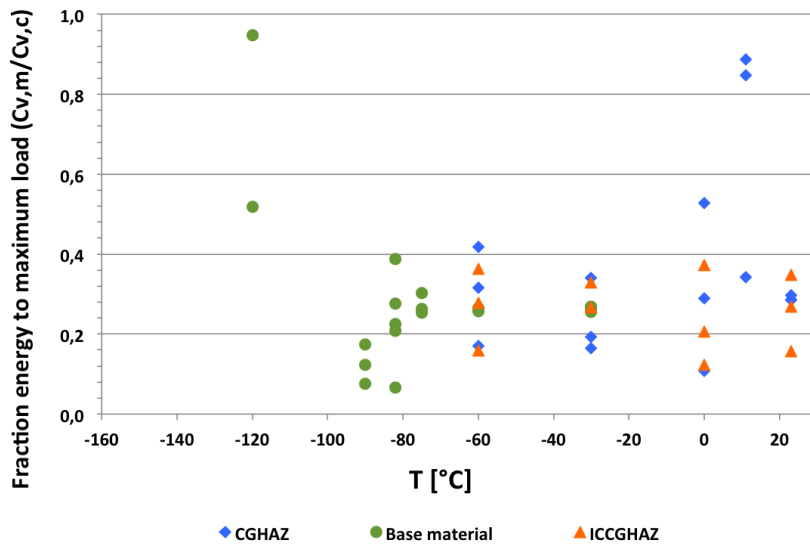


(b) Fraction absorbed energy to brittle fracture initiation, $\frac{C_{V,f}}{C_{V,c}}$. Class I does not show brittle fracture initiation, and are therefore excluded. No class V curves obtained for the notched series.

Figure 5.5: Distribution of $\frac{C_{V,m}}{C_{V,c}}$ and $\frac{C_{V,f}}{C_{V,c}}$ as a function of curve class for both notched (dark, diamond-shaped points) and pre-cracked series (light, circular points).

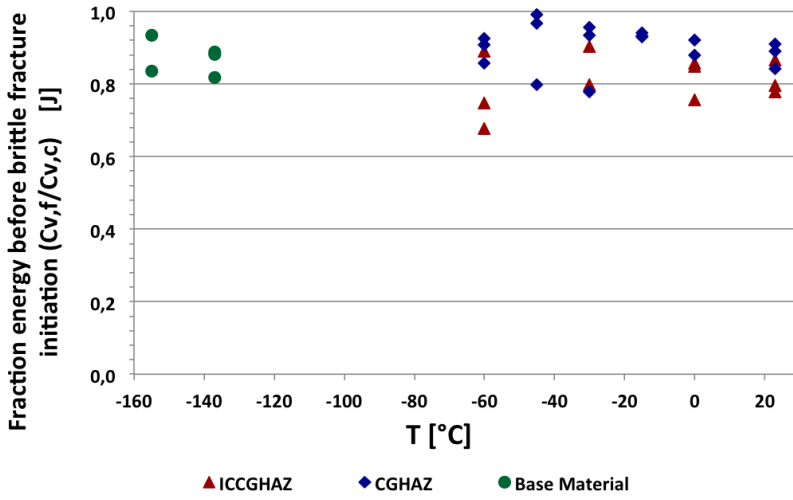


(a) With V-notch

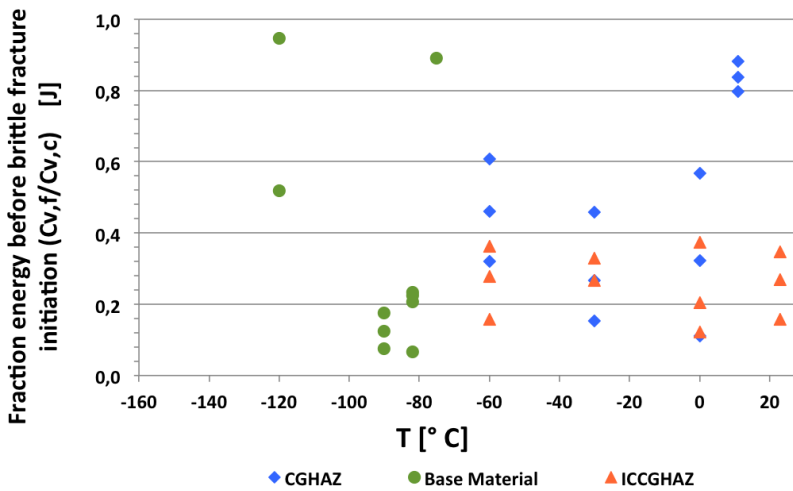


(b) With pre-crack

Figure 5.6: Distribution of fraction $\frac{C_{v,m}}{C_{v,c}}$ as a function of test temperature for (a) V-notched series and (b) pre-cracked series for base material (green), weld simulated CGHAZ (blue) and ICCGHAZ (red) microstructures.



(a) With V-notch



(b) With pre-crack

Figure 5.7: Distribution of fraction $\frac{C_{v,f}}{C_{v,c}}$ as a function of test temperature for (a) V-notched series and (b) pre-cracked series for base material (green), weld simulated CGHAZ (blue) and ICCGHAZ (red) microstructures.

The $\frac{C_{V,m}}{C_{V,c}}$ fractions obtained for the notched specimens (Figure 5.3) are seen to be higher for the same test temperature and microstructure tested compared to the fractions obtained from testing of pre-cracked specimens. An exception is the CGHAZ microstructure for the highest test temperature. It can also be seen that for the notched series (Figure 5.6(a)), the $\frac{C_{V,m}}{C_{V,c}}$ value decreases with increasing temperature.

For the notched series in Figure 5.6, the value of $\frac{C_{V,m}}{C_{V,c}}$ seems to stabilize at a value of about 0.3 for the base material. In addition, a notable drop in $\frac{C_{V,m}}{C_{V,c}}$ value can be seen between -137 °C and -120 °C for this series. The CGHAZ and the ICCGHAZ materials show a more gradually decreasing value, where the $\frac{C_{V,m}}{C_{V,c}}$ values are seen to approach the same value as for the base-material series at high test temperatures.

For the pre-cracked series in Figure 5.6, a decrease in $\frac{C_{V,m}}{C_{V,c}}$ values with increasing temperature is not seen for all three microstructures tested. Here, the CGHAZ series show high $\frac{C_{V,m}}{C_{V,c}}$ values for some of the highest test temperatures. The fractions obtained at the different temperatures for the ICCGHAZ series have a quite stable value. For the base material the fraction is seen to stabilize at a value of approximately 0.3, the same value that the value was seen to stabilize at for the notched base material series.

The distribution of the $\frac{C_{V,f}}{C_V}$ fractions are similar to the $\frac{C_{V,m}}{C_{V,c}}$ fraction distribution for the pre-cracked series, although some values are shifted to higher values, especially evident for the CGHAZ microstructure. In the plot of the $\frac{C_{V,f}}{C_{V,c}}$ for the notched series, all of the fractions show high values. The values are more scattered for the pre-cracked CGHAZ parallel and quite stable for the pre-cracked ICCGHAZ parallel.

5.5 Results From CTOD Testing

The average measured critical CTOD values (CTOD at final fracture) are included in Table 5.3 and are presented graphically in Figure 5.8. Data for all performed tests can be found in Appendix B. The measured CTOD values are lower for the ICCGHAZ microstructure than the CGHAZ microstructure over the whole temperature range tested. It can be seen that the SD is generally higher for the CGHAZ microstructure, while the results from testing of ICCGHAZ microstructure are less scattered. The CTOD value show a decrease in CTOD from 0 °C and -30 °C for both the CGHAZ and ICCGHAZ series, although less significant for the ICCGHAZ than the CGHAZ microstructure.

Table 5.3: Average measured CTOD at each test temperature.

Microstructure	Temperature [°C]	Average CTOD [mm]	SD	RSD [%]	Total No. of Tests
CGHAZ	0	0.756	0.266	35.1	10
	-30	0.189	0.169	89.2	10
	-60	0.114	0.095	83.5	10
	-90	0.092	0.065	71.5	10
ICCGHAZ	0	0.185	0.050	27.0	10
	-30	0.090	0.033	37.2	10
	-60	0.050	0.018	36.2	10
	-90	0.024	0.006	25.8	9

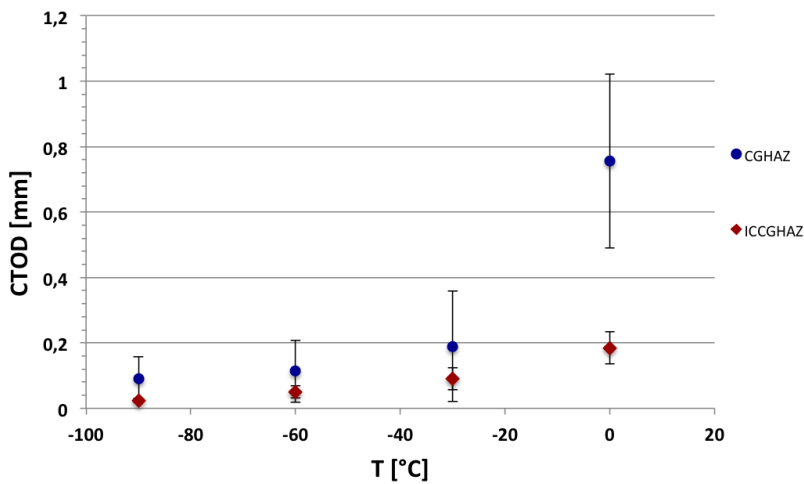


Figure 5.8: Average measured CTOD values with error bars for CGHAZ (blue) and ICCGHAZ (red).

5.6 Results From Fracture Surface Investigations

Several initiation points were found and imaged along the notch and pre-crack borders in the investigated samples. A representative selection of micrographs of the investigated samples is included in this section. For all of the investigated specimens, a micrograph of lower magnification is included to show how close the crack facets were found. Several facets and possible initiation points are also included.

5.6.1 CGHAZ, V-notched tested at -30°C

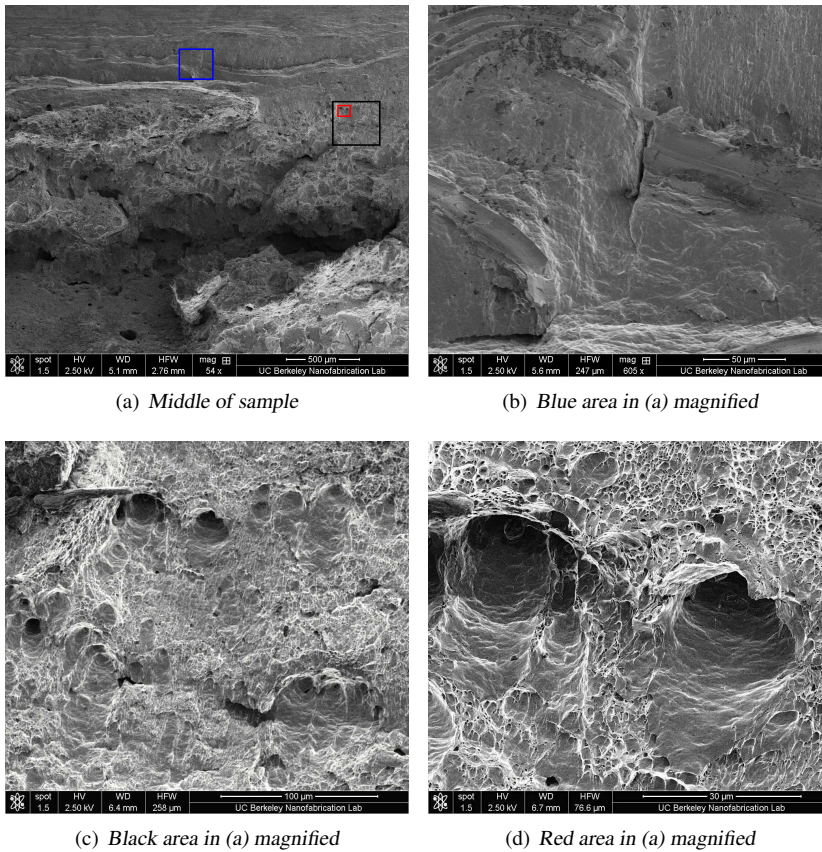


Figure 5.9: Micrographs of V-notched CGHAZ tested at -30°C . Specimen *ss4c*. Images from new and previous work performed [74].

The specimen show a ductile fracture appearance over a larger distance from the notch compared to the other investigated specimens including a rougher appearance with larger dimples further away from the notch. Particles can be seen inside the dimples in Figure (c) and (d).

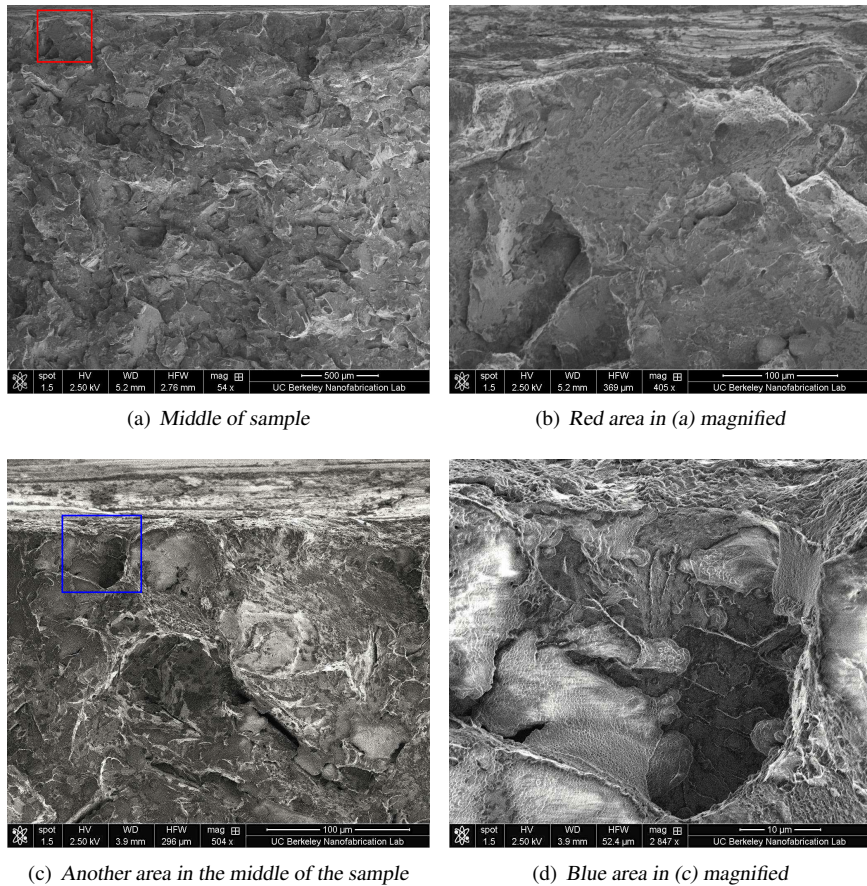
5.6.2 CGHAZ, V-notched tested at -60°C 

Figure 5.10: Micrographs of V-notched CGHAZ tested at -60°C . Specimen ss7c. The sample looks somewhat contaminated.

Cleavage facets are seen closer to the notch, compared to the specimen tested at -30 celsius. The facet shown in (b) show river patterns extending upwards to the right. However, although treated the same way as the other samples, the micrographs shows that this specimen looks somewhat contaminated. Therefore, detailed and good images for has been hard to obtain.

5.6.3 CGHAZ, pre-cracked tested at 0°C

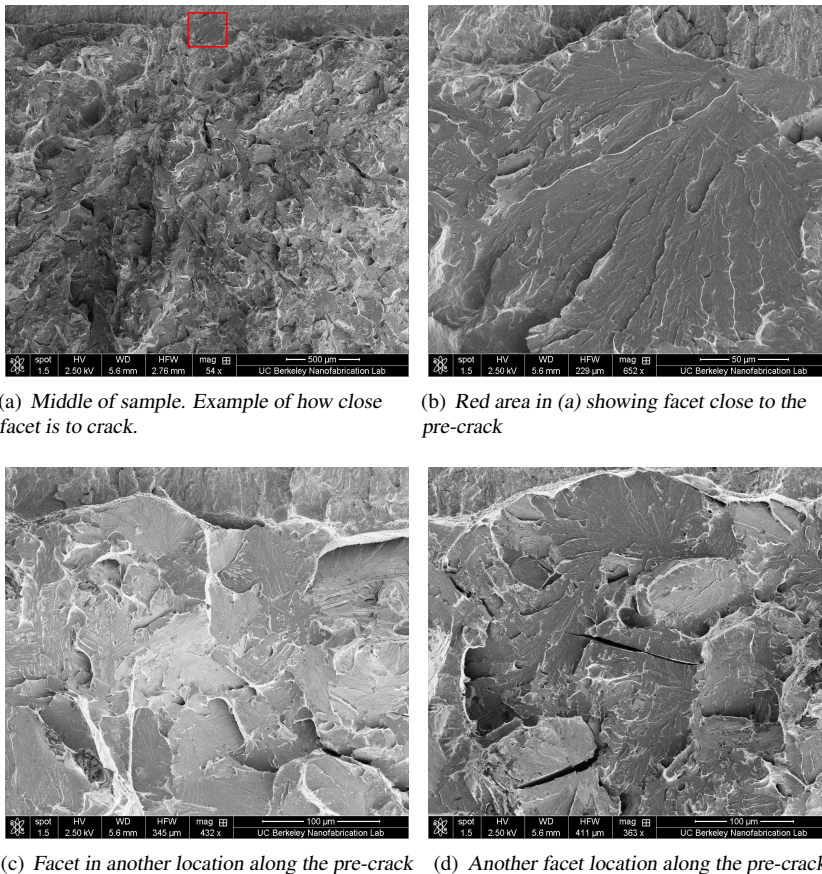
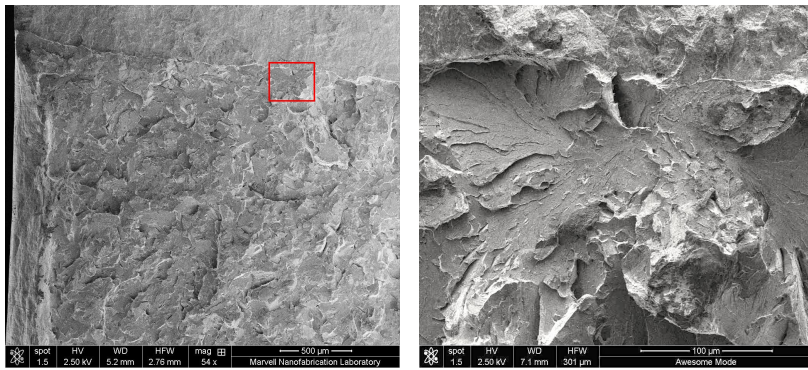


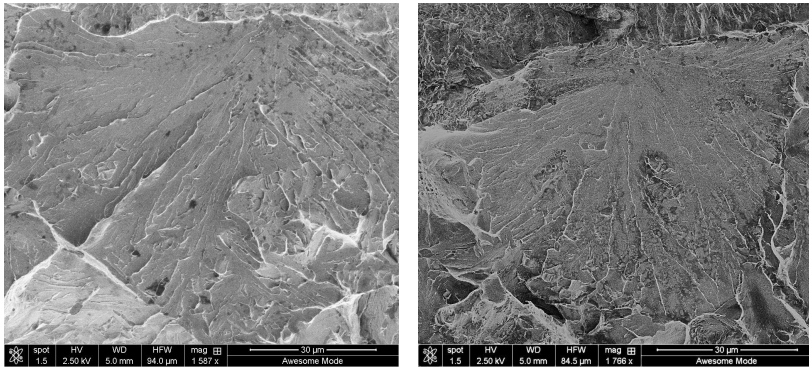
Figure 5.11: Micrographs of pre-cracked CGHAZ tested at 0°C. Specimen *ss30f*.

Facets are seen to appear very close to the pre-crack border, as in micrograph (b). Here, the river patterns are pointing downwards, away from the pre-crack. Also, several other initiation sites are found close to the pre-crack, as in micrograph (c) and (d). These facets do not occur almost at the pre-crack border and have river patterns extending upwards towards the end of the pre-crack. Micrograph (c) and (d) also show a "rougher" appearance with smaller cracks and several blocks of facets with different origins. This shows that there is some variation along the pre-crack.

5.6.4 CGHAZ, pre-cracked tested at -30°C 

(a) Left side of the sample. Showing location of facets in (b)

(b) Red area magnified



(c) Facet in another location along the pre-crack (d) Another facet along the pre-crack border

Figure 5.12: Micrographs of pre-cracked CGHAZ tested at -30°C . Specimen ss27c. Micrographs obtained during new and previous previous work performed [74].

Several initiation points were found directly at the pre-crack border with river patterns growing downwards, away from the pre-crack, as in (c) and (d). Micrograph (b) show facets originating from a initiation point at some distance away from the crack border. Here, the river patterns are growing diagonally up towards the end of the pre-crack.

5.6.5 ICCGHAZ, V-notched tested at -30°C

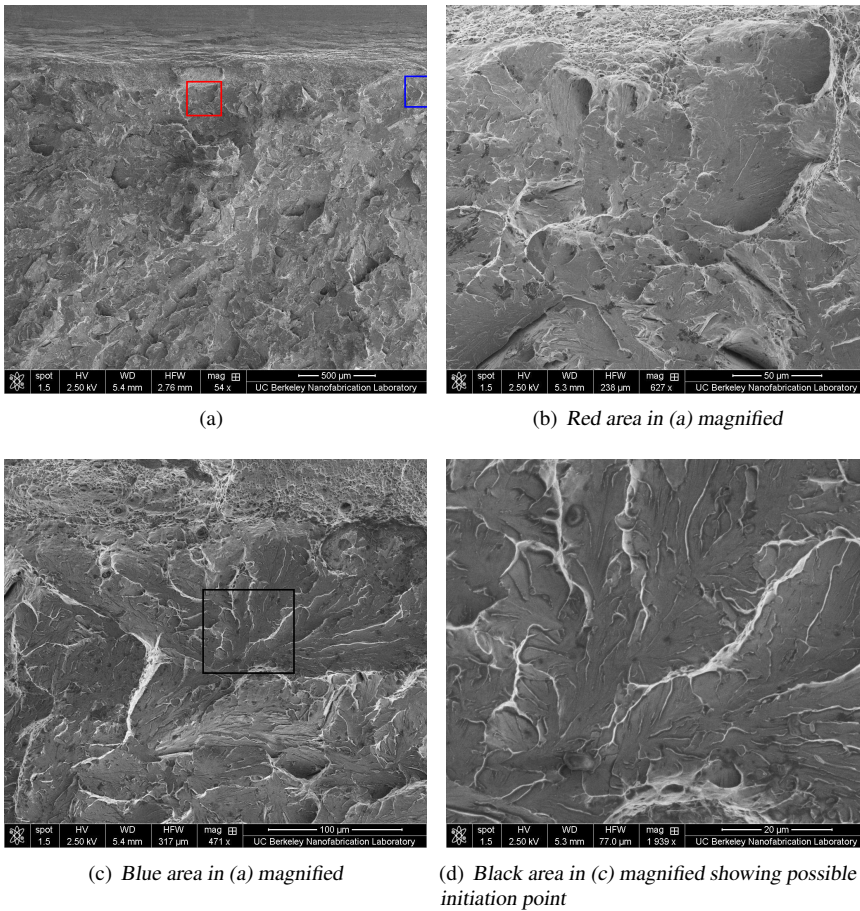


Figure 5.13: Micrographs of V-notched ICCGHAZ tested at -30°C . Specimen ss2.104c.

A band with ductile fracture appearance can be seen before the cleavage region in micrograph (a). The facets are not as distinct as the ones seen in Figure 5.11 and 5.12. The cleavage facets have river patterns originating at some distance away from the notch border growing up towards the notch. Some ductile areas are seen between the faceted areas.

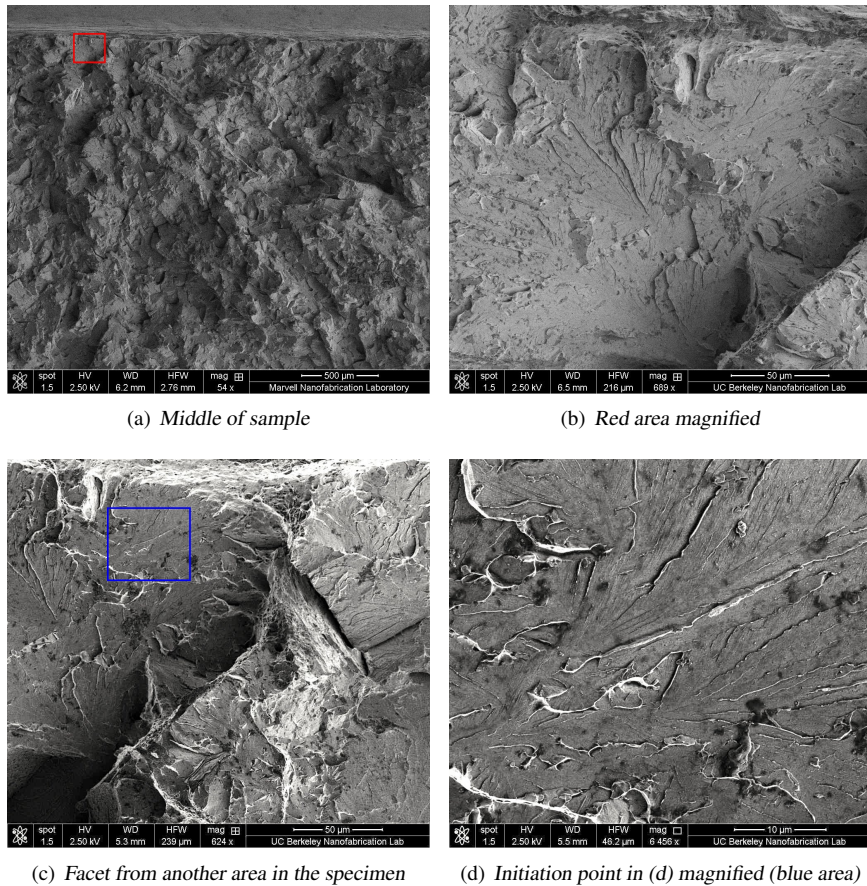
5.6.6 ICCGHAZ, V-notched tested at -60°C 

Figure 5.14: Micrographs of V-notched ICCGHAZ tested at -60°C . Specimen ss2.106c.

Cleavage facets are seen to initiate closer to the notch compared to the facets imaged in Figure 5.13. The river patterns are reaching towards the notch in this specimen as well. Some areas show a rougher surface than others, as the area to the right in micrograph (c). Here, larger cracks can also be observed.

5.6.7 ICCGHAZ, pre-cracked tested at 0°C

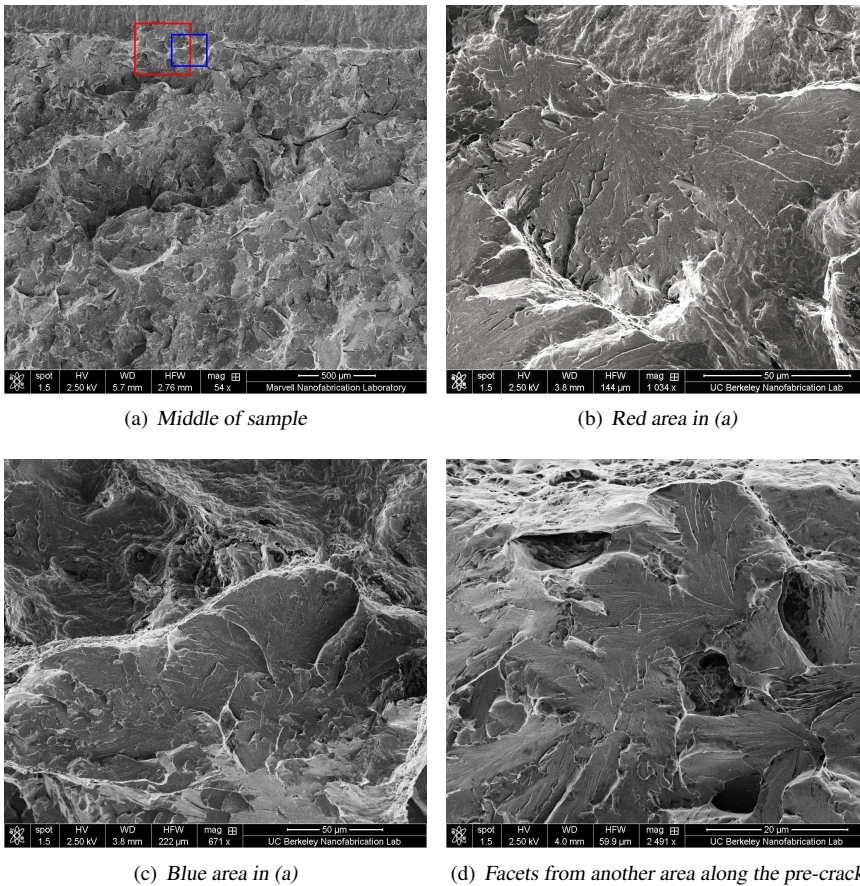


Figure 5.15: Micrographs of pre-cracked ICCGHAZ tested at 0°C. Specimen ss2.79f.

Facets are found close to the pre-crack border. Some facets appears to have initiated almost at the pre-crack border itself, like the facet shown in micrograph (b). The river patterns are seen to continue until another facet is met, where a smaller ductile region can be observed. The micrographs (c) and (d) show smaller facets originating at a distance away from the pre-crack very close to the facet shown in (b). The fracture appearance changes locally along the pre-crack. In micrograph (c) and (d), a small portion of ductile fracture is observed before the facets are initiated, and ductile areas can be seen between the facets.

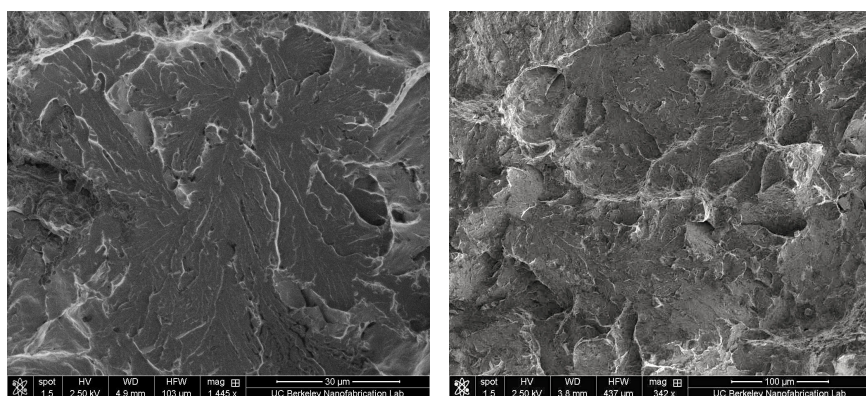
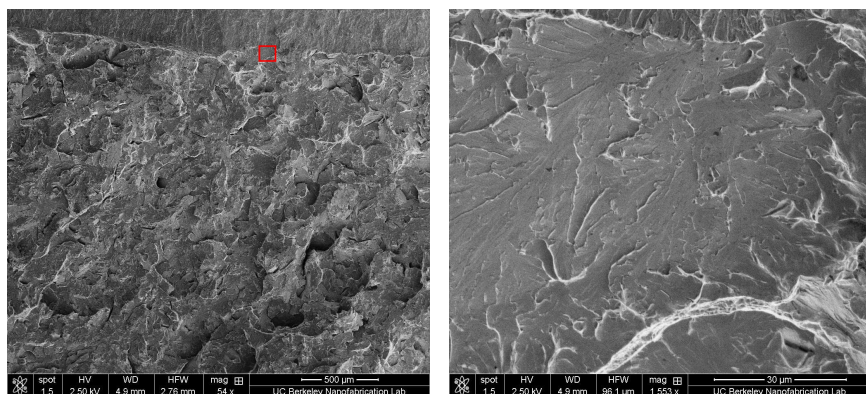
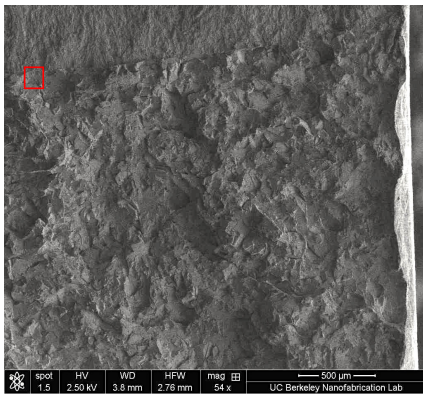
5.6.8 ICCGHAZ, pre-cracked tested at -30°C 

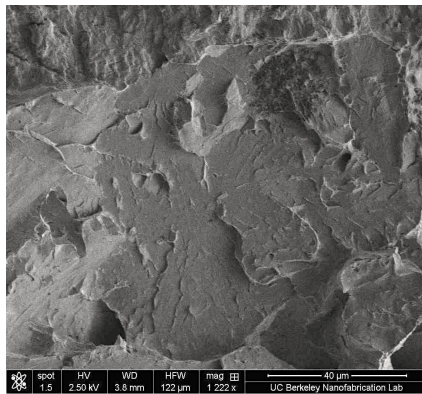
Figure 5.16: Micrographs of pre-cracked ICCGHAZ tested at -30°C . Specimen ss2.82f.

Several facets are seen close to the pre-crack with initiation points very close to the crack. In these facets, the river patterns are branching downwards, away from the pre-crack. Some facets are also seen to initiate a bit further away from the pre-crack. There are some ductile areas within the areas governed by cleavage, as can be seen in micrograph (b).

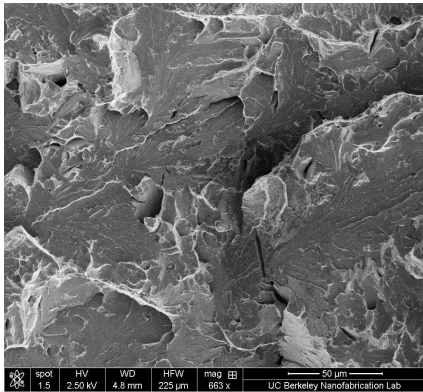
5.6.9 ICCGHAZ, pre-cracked tested at -60°C



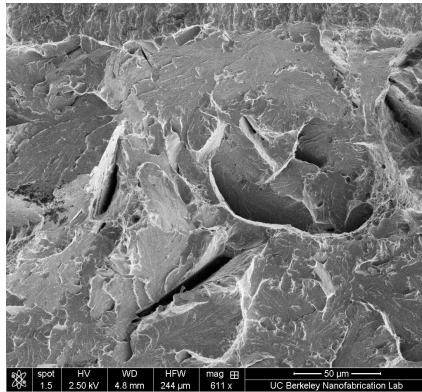
(a) Right side of the specimen



(b) Red area in (a)



(c) Another facet from area closer to the middle of the specimen along the pre-crack



(d) Facet area a little to the right of the area shown in (c)

Figure 5.17: Micrographs of pre-cracked ICCGHAZ tested at -60°C . Specimen ss2.87f.

Facets are seen to begin close to the pre-crack, like in micrograph (d). Here, ductile areas can also be observed between areas with cleavage facets. The ductile regions only appear along some parts of the pre-crack are not seen along the remaining areas along the end of the pre-crack. Large facets originating just at the end of the pre-crack, as in Figure 5.15 and 5.16 were not seen.

5.7 Results From Microstructural Investigations

Micrographs obtained using Nital-etchant are presented in Figure 5.18, 5.20 and 5.22. The micrographs presented are obtained using a 50X objective. It should be noted that two different microscopes with different cameras and set-up have been used when imaging the specimens with the two etchants. Therefore, the magnification is not identical, although all images have been obtained using 50X objectives.

The base material has a finer grain structure compared to the CGHAZ and the ICCGHAZ microstructures, consisting of mainly fine bainite and ferrite phases. It can be seen that the grains found in the CGHAZ microstructure are largest and that the structure is inhomogeneous.

The CGHAZ mainly consist of bainite and martensite, which can be seen in the micrograph obtained using Nital etchant (Figure 5.20). Areas with a brown tint are believed to be martensite, while the lighter areas with darker lines are believed to be bainite, possibly upper bainite. Grain boundaries are also detectable, as dark continuous lines. In the micrograph obtained using LaPera (Figure 5.21), light areas are found along the grain boundaries and between the bainite and martensite laths. These lighter areas are believed to be MA constituents or MAC aggregates. These are not as easily visible in the micrograph obtained using Nital.

The ICCGHAZ microstructure is somewhat finer, but is also inhomogeneous, consisting of bainite and martensite. The martensite is not brown coloured brown as it has been tempered during the second weld cycle. Therefore, it appears as though more martensite is present in CGHAZ. Prior austenite grain boundaries are not as visual as in the micrographs for CGHAZ. Individual MA islands can be seen in the micrographs for both of the etchants used. In the micrograph obtained using Nital, the MA islands are brown and appear as larger or smaller regions. Some of the largest MA-regions found are pointed out in Figure 5.22. The MA-regions pointed out in Figure 5.23 are seen to be of comparable size. Prior austenite grain boundaries can be glimpsed vaguely, at least in the micrograph where LaPera etchant has been used, where the white phases appears more closely spaced.

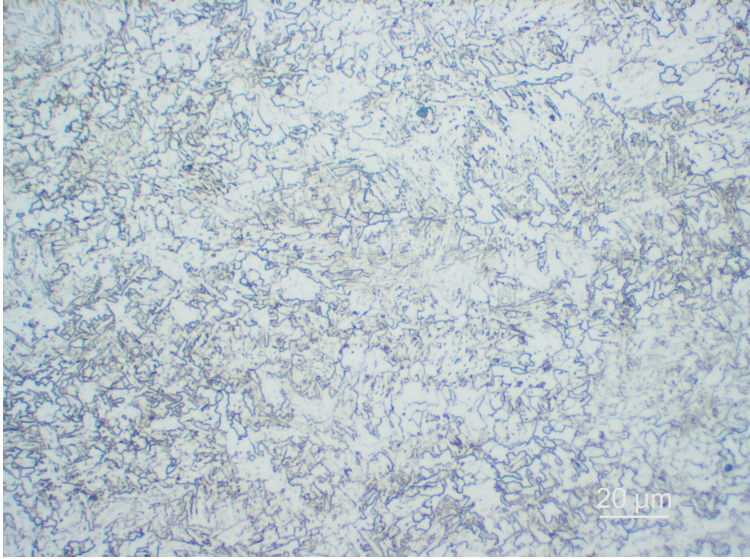


Figure 5.18: *Microstructure of base material. 2% Nital etchant has been used and the microstructure is imaged using a 50X objective.*

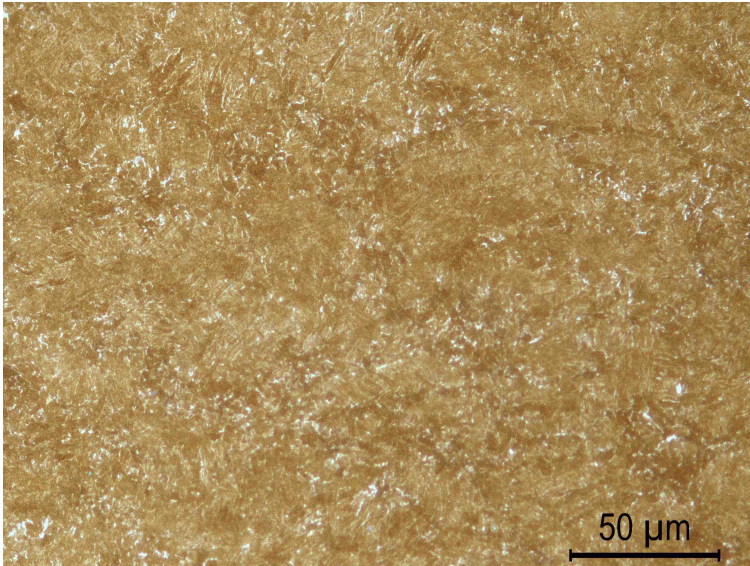


Figure 5.19: *Microstructure of base material. LaPera etchant has been used and the microstructure is imaged using a 50X objective.*

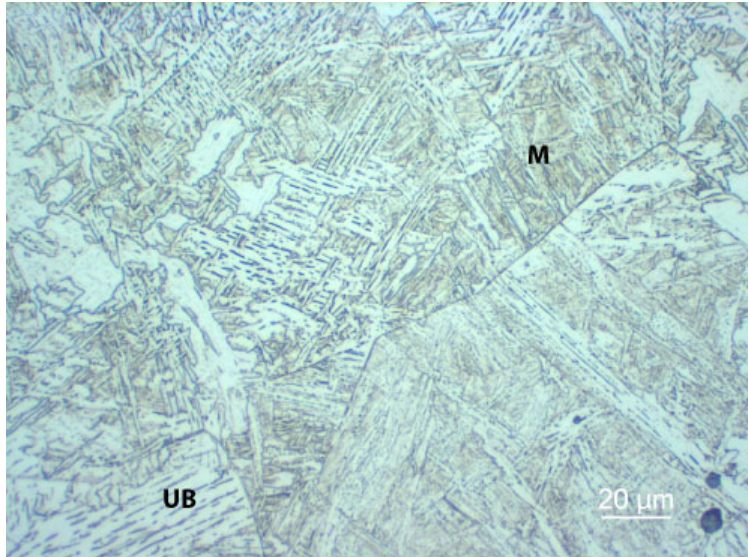


Figure 5.20: Microstructure of the CGHAZ microstructure. 2% Nital etchant has been used and the microstructure is imaged using a 50X objective. M = Martensite, UB = Upper Bainite.

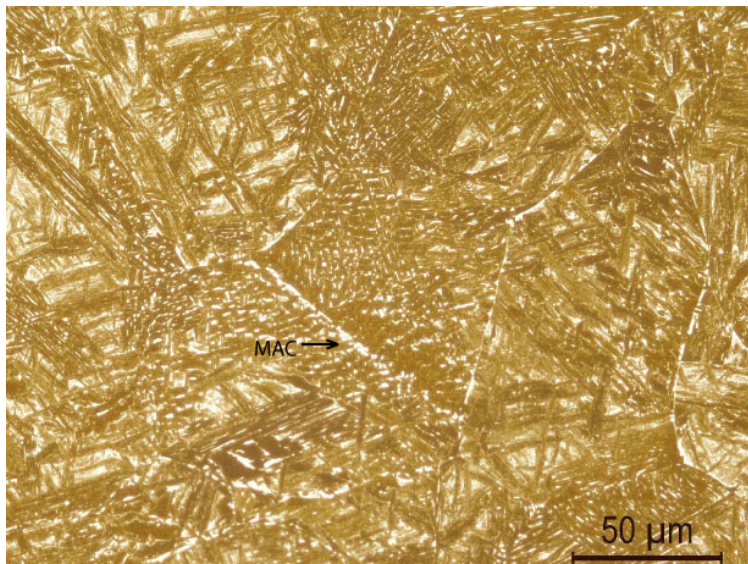


Figure 5.21: Microstructure of the CGHAZ microstructure. LaPera etchant has been used and the microstructure is imaged using a 50X objective. MAC = Martensite-Austenite-Carbide.

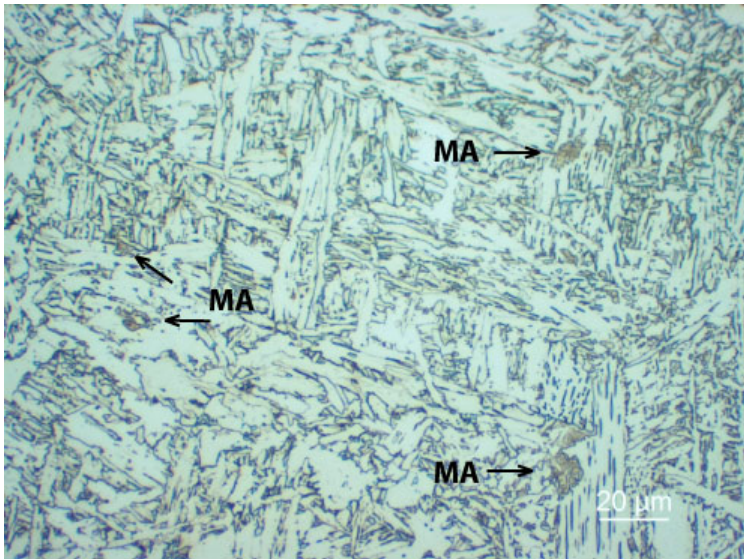


Figure 5.22: Microstructure of the ICCGHAZ microstructure. 2% Nital etchant has been used and the microstructure is imaged using a 50X objective. MA = Martensite-Austenite.

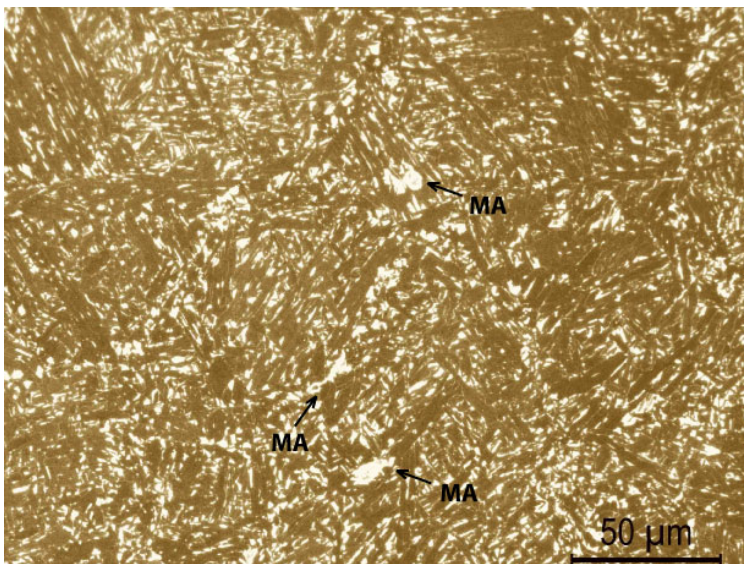


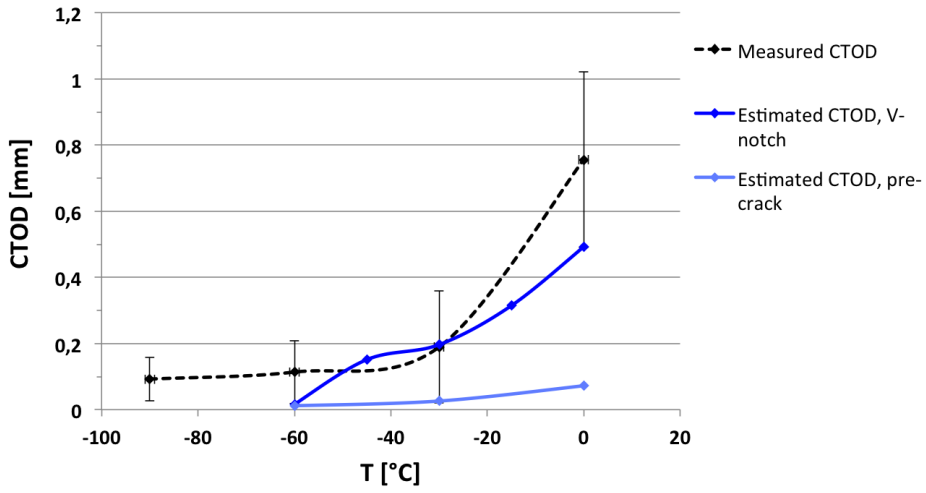
Figure 5.23: Microstructure of the ICCGHAZ microstructure. LaPera etchant has been used and the microstructure is imaged using a 50X objective. MA = Martensite-Austenite.

5.8 Results From Using CTOD Correlations

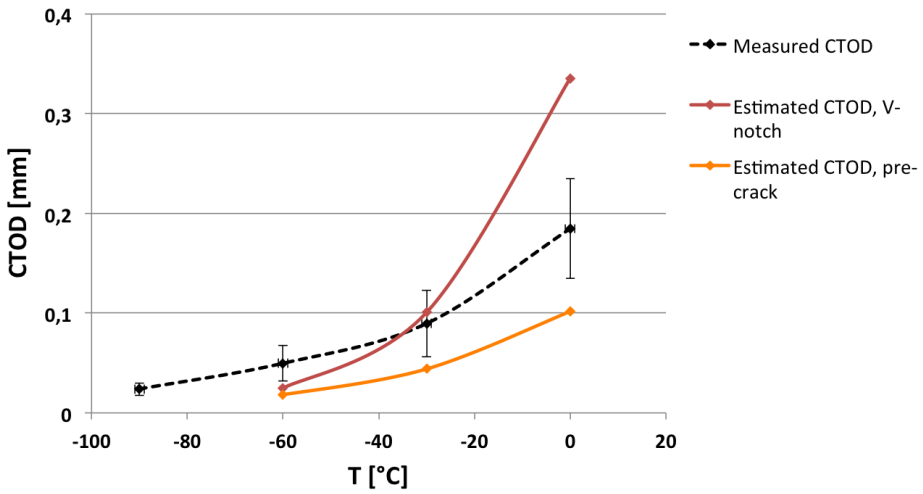
The results from using correlations between the data obtained during Charpy-V Notch (CVN) and fracture mechanical testing are presented in this section. The degree of correlation of the investigated methods has been evaluated mainly using notched Charpy data. This has been done because it has to be taken into consideration that the correlations are empirical and developed for correlating data obtained using notched Charpy specimens. Nevertheless, results from using pre-cracked specimens are included in order to see how well the empirical correlations might predict CTOD values for this specimen configuration also.

5.8.1 Lower Bound Relation after BS7910

CTOD values estimated using the lower bound method in BS7910, described in section 4.8.1 are presented below both for CGHAZ and ICCGHAZ material. The real measured CTOD values are included with error bars showing the standard deviation measured during the tests performed. The other curves show CTOD values obtained from averaged measured Charpy energy values, C_V . A The results are plotted in Figure 5.24.



(a) CGHAZ



(b) ICCGAZ

Figure 5.24: Estimate of CTOD values using lower bound method in BS7910, $B = 10$

5.8.2 The Master Curve Approach

Calculation of T_0 to be used in the Master Curve Correlation

Estimation of T_0 using Equation (4.5) in ASTM E1921 and BS7910 and Equation (4.6) developed by Wallin are given in Table 5.4 presented below. Estimates with and without a pre-crack correction in Equation (4.5) are included. The estimated TC_{V28J} used in the equations and the T_{trans} value for the curves where this parameter can roughly be estimated are included in the table for comparison. CTOD values for the two ICCGHAZ series and the pre-cracked CGHAZ series have been estimated by assuming that the upper shelves are at comparable values as the V-notched CGHAZ series.

It can be seen that both equations used to predict T_0 estimate a lower value than the values estimated from the transition curves. Also, the pre-crack correction provides lower T_0 estimates. When T_0 is estimated using Equation (4.6) by Wallin, the resulting values are very low for the notched specimens, while the equation provides comparable values to T_0 values estimated using the pre-crack correction in Equation (4.5). In addition, T_0 values are not seen to be far from to the T_{trans} temperatures estimated from the Charpy transition curves.

Table 5.4: Temperatures used in estimation of T_0 .

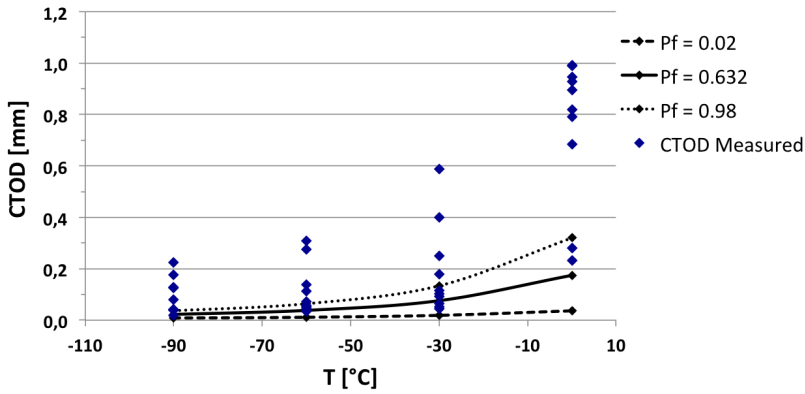
Temperature parameter [°C]	Microstructure			
	CGHAZ		ICCGHAZ	
	V-notch	pre-crack	V-notch	pre-crack
T_{trans} from transition curves (Fig. 5.1)	-15	10	~0	>23
TC_{V28J} from curves	-55		-46	
T_0 from ASTM1921/BS7910 (Equation (4.5))	-73		-64	
T_0 from ASTM1921 with pre-crack corr. (Equation (4.5))		-58		-72
T_0 from equation by Wallin (Equation (4.6))	-102	-55	-93	-69

CTOD Values Estimated Using the Master Curve

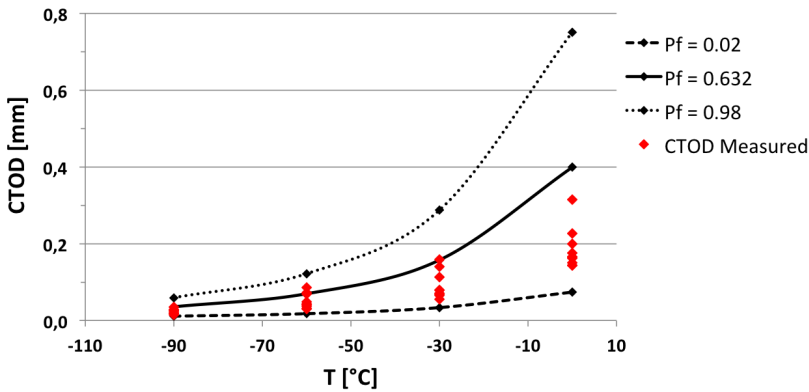
The results from using the MC to estimate real CTOD values from C_V values are presented below. The test results from using notched specimens are used in obtaining the correlations. In addition, data from pre-cracked specimens have been used in order to see how well the correlation predicts CTOD values for this specimen configuration. In all of the graphs, curves using a fracture probability, P_f of 0.02, 0.632 and 0.98 are shown.

The curve using a P_f of 0.632 can be considered a median estimate, while the curves with P_f set to 0.02 and 0.98 represent validity limits for the estimated CTOD values.

The resulting curves using a T_k of 25 a thickness, B , of 10 mm and Equation (4.5) are presented first (Figure 5.25). These curves are used as a reference when investigating the effect of the different parameters used in the correlation.



(a) CGHAZ V-notched

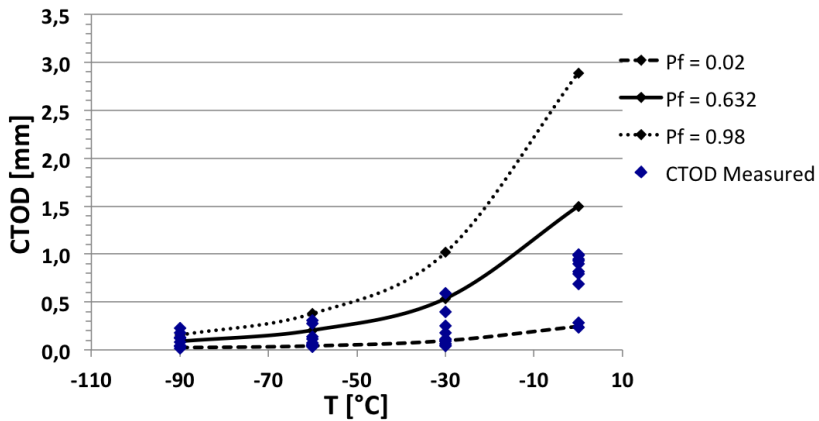


(b) ICCGHAZ V-notched

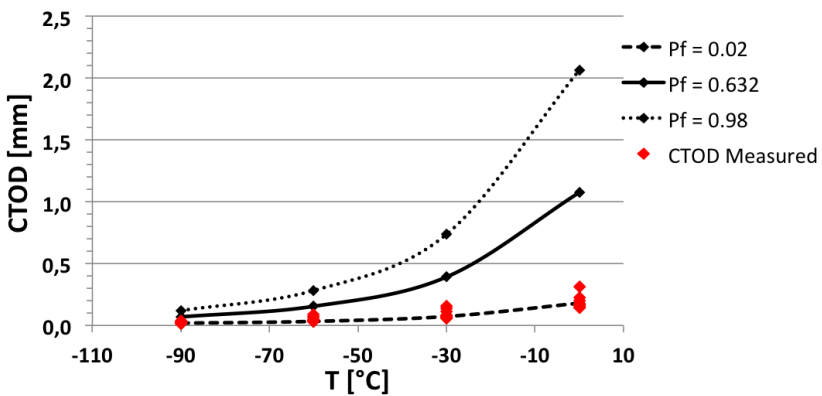
Figure 5.25: Master Curve with scatter bands and parameters $T_k=25$, $B=10$ in Equation (4.7).

CTOD Values Calculated Using Alternative Equation for T_0 by Wallin

The resulting curves obtained using Equation (4.6) are presented below in Figure 5.26. It can be seen that the estimated CTOD values are over 2.5 times higher for the V-notched series when using Equation (4.6) compared to Equation (4.5) presented above.



(a) CGHAZ V-notched

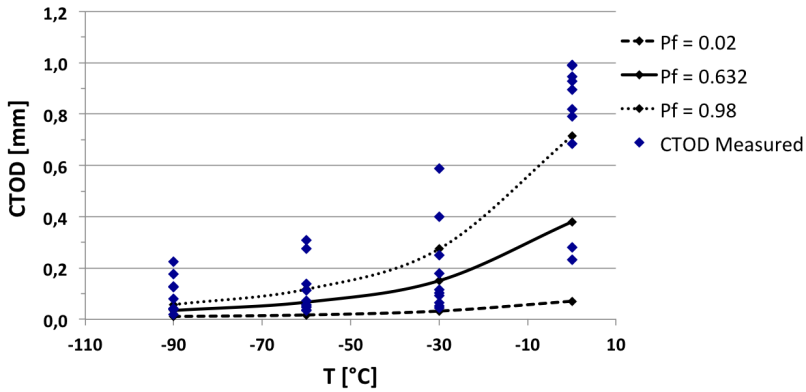


(b) ICCGHAZ V-notched

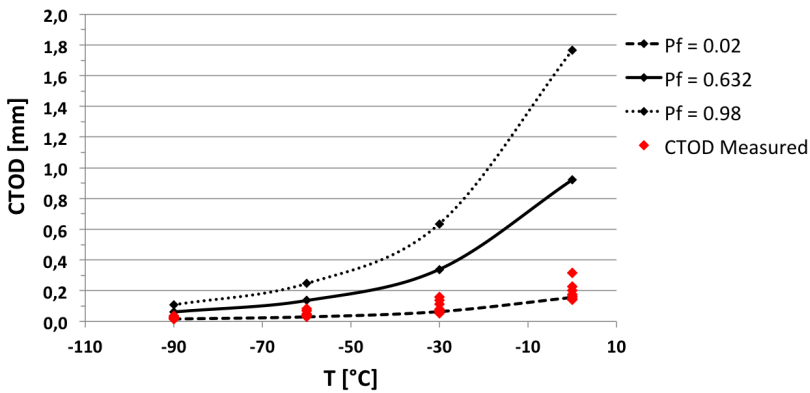
Figure 5.26: Master Curve with scatter bands and parameters $T_k=25$, $B=10$ in Equation (4.7). Alternative T_0 estimation by using Equation (4.6) by Wallin.

Effect of Changing T_k on the CTOD Values

It can be seen that the MC correlation provides a more conservative estimate of the CTOD with an increasing T_k value when comparing Figure 5.27 and 5.25, as lower CTOD values are estimated.



(a) CGHAZ V-notched

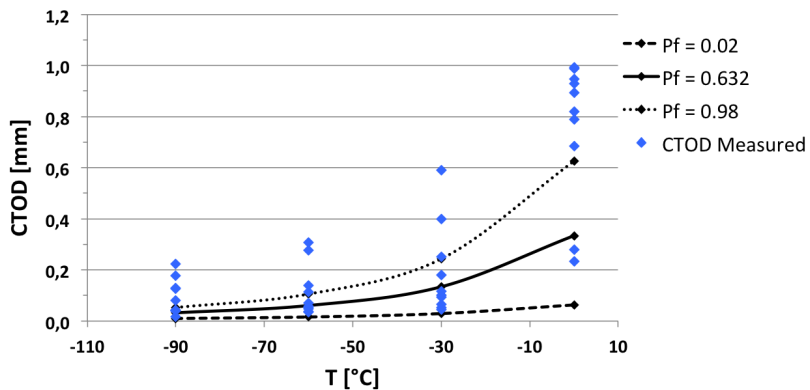


(b) ICCGHAZ V-notched

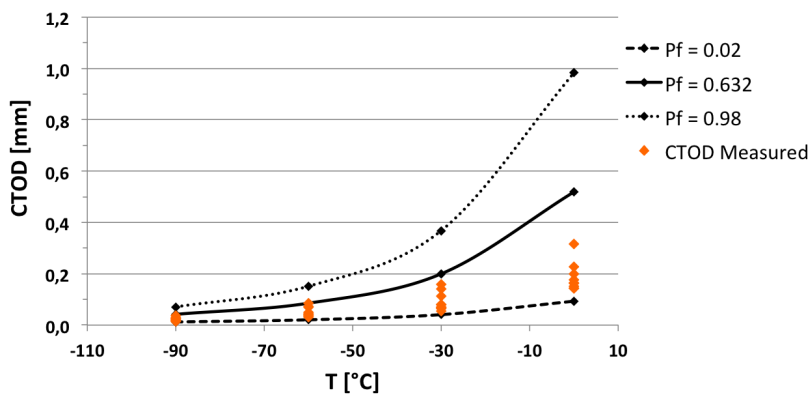
Figure 5.27: Master Curve with scatter bands and parameters $T_k=0$, $B=10$ in Equation (4.7).

Effect of the Pre-Crack Correction in Determining T_0 on the CTOD Values

In order to use data from pre-cracked Charpy specimens in the MC correlation, as the ones used in instrumented Charpy testing, using a C value of 50 in Equation (4.5) is recommended in ASTM E1921. The resulting MC and how it fits with the CTOD values obtained during testing can be seen in Figure 5.28 (a) and (b) for the CGHAZ and ICCGHAZ microstructures, respectively.



(a) CGHAZ pre-cracked, $C = 50$



(b) ICCGHAZ pre-cracked $C = 50$

Figure 5.28: Master Curve for pre-cracked series with scatter bands and parameters $T_k=25$, $B=10$, in Equation (4.7) and $C = 50$ in Equation (4.5).

6 Discussion of Results

The following discussion aims to explain and connect the different results obtained. The focus of the discussion are the trends seen at low test temperatures in the lower shelf and lower transition regions, although trends seen for higher test temperatures and upper shelf behaviour are included in describing some of the general trends observed.

6.1 Transition Curves

Although the lowest values obtained for each test temperature during Charpy testing should generally be used for structural assessment purposes, the discussion is based on the Charpy transition curves obtained using average measured Charpy energies, C_V . As can be seen from comparing the curve obtained with average C_V values and lower bound C_V values (Figure 5.1 and 5.2), respectively, the shape of the curves are similar.

Due to the large scatter obtained from testing at several test temperatures, the conservative position of the transition curve is hard to establish based on only three parallel tests at each test temperature. Using average C_V values with error bars allows for the data scatter to be presented along with the curves and is believed to provide a better overview of the test results than curves generated by using strictly lower bound values.

6.1.1 Effect of Changes in Microstructure

The transition curves in Figure 5.1 show that the fracture toughness of the investigated steel is deteriorated when subjected to typical heat cycles experienced during welding. The steel is deteriorated despite the estimated carbon equivalent shows that the steel investigated should can be considered weldable. The trends observed and possible reasons for this are discussed below.

The curves are shifted to higher temperatures when the steel has been weld simulated prior to testing. When comparing the notched base material and CGHAZ series, a shift of approximately $-110\text{ }^{\circ}\text{C}$ to the right is observed. This is a significant increase, and the investigated steel shows poor fracture properties even at room temperature in as welded condition. These findings suggest that the weld-simulated material behaves in a much more brittle manner than the base material, even at normal operating temperatures found in the North Sea.

From the large increase in T_{trans} for the welded microstructures compared to the base material, it is evident that the fracture properties of the material of interest has been severely degraded by the weld simulation performed. This suggests that the microstructure of the steel has changed, as brittle fracture occurs for higher test temperatures in the welded material. This was confirmed by optical light microscopy (Section 5.7). The T_{trans} of the weld microstructures being close to room temperature shows that the steel that was originally considered to be a candidate for low temperature applications may, in as-welded condition, not even provide sufficient toughness at ambient temperatures. Hence, the investigated steel can not be considered safe to be used in as-welded condition in Arctic environments. If this particular steel is accepted to be used in as-welded condition, eventual cracks and flaws present in the material would have to be very small.

The upper shelf is obtained for somewhat lower energy values for the CGHAZ notched curve compared to the base material, while the upper shelf is not reached at all for the pre-cracked CGHAZ and both of the ICCGAZ curves. This can be explained in terms of the temperature dependence of the σ_Y and the fracture strength of materials. The welded material experiences a transition between ductile and brittle fracture mode at a higher temperature. At higher temperatures, the strength of the material and σ_Y generally tends to be somewhat lower, and may explain why the upper shelf is obtained for lower measured loads (or C_V) at higher temperatures.

From previous research of the investigated steel, σ_Y was found to be somewhat higher, about 20 to 100 MPa, for the base material tested at $-100\text{ }^{\circ}\text{C}$ compared to σ_Y for the CGHAZ and ICCGAZ microstructures tested at $0\text{ }^{\circ}\text{C}$. As the temperature increases, the tensile strength of the material decreases. From previous research of the investigated steel, the tensile strength was found to be somewhat lower, about 40 to 90 MPa, for the

base material tested at $-100\text{ }^{\circ}\text{C}$ compared to the tensile strength for the CGHAZ and ICCGHAZ microstructures tested at $0\text{ }^{\circ}\text{C}$ [93]. This may imply that the weld-simulated microstructures might be more ductile than the base material. When the strength of a material decreases, the load bearing capacity also decreases. The tensile strength being lower in the weld-simulated microstructures might have led to lower upper shelf values for these microstructures.

The shape of the transition curves are somewhat different for the weld simulated series compared to the base material series, especially in the transition region. The base material curves exhibit a steep increase in measured energy with increasing temperature leading to a narrow transition region. In the weld simulated series on the other hand, a wider transition region is observed. This is especially evident for the weld-simulated series with a standard V-notch, and may be linked to the scatter in the C_V values that can be explained in terms of microstructure.

As the fracture toughness can vary between phases, a more inhomogeneous microstructure, as seen for the CGHAZ microstructure especially, can lead to a wider transition region. When testing inhomogeneous materials, the sampled material in front of the crack tip may be different in parallel test specimens. Since the microstructure sampled in front of the crack tip to a great extent determines the fracture mode and test result obtained during testing, the data results are scattered over a wider temperature range for inhomogeneous materials. The result can be fracture occurring both by ductile and brittle fracture modes for the same test temperature over a larger temperature interval. Hence, the transition region will be wider for the CGHAZ, as observed.

As the T_{trans} of the ICCGHAZ microstructure is found to be highest, indicating a lower toughness, of the three microstructures investigated, subjecting the steel to two-cycle or multi-pass welding procedures renders the steel susceptible to brittle fracture if used in Arctic regions with temperatures as low as $-70\text{ }^{\circ}\text{C}$. The ICCGHAZ pre-cracked parallel show almost no scatter in the measured data, and the scatter is notable only for one test temperature.

Also, for the pre-cracked parallel the upper shelf has not been reached at the highest test temperature, and the location of the transition region is not clear. The ICCGHAZ series may also like the CGHAZ microstructure have a wide transition region. Testing at higher temperatures would have to be performed in order to discuss the fracture behaviour in the transition region for the ICCGHAZ microstructure.

6.1.2 Effect of Notch Geometry

From studying the transition curves in Figure 5.1, it is evident that using pre-cracked instead of notched specimens changes the position of the curves to higher temperatures. This is equivalent to elevated T_{trans} . These changes are discussed below.

One of the apparent results is the transition curves being shifted to the right, towards higher temperatures. This shift is more pronounced within the transition region. This is especially evident for the base material curves, which is the only microstructure tested where the whole transition curve is obtained for both notch geometries. For the pre-cracked specimens, T_{trans} changes about 35 °C, from -20 °C to 15 °C for the weld simulated material, if it is assumed that the upper shelf is reached at a comparable level as the notched series. For the base material, the middle of the transition region is shifted from around -130 °C to -75 °C, a difference of 55 °C.

A curve shift to higher temperatures is equivalent to the measured energies being lower for pre-cracked specimens at the same test temperature. The lower energies measured for the pre-cracked specimens may be explained by the different stress field experienced in front of a sharp crack compared to a notch and the fact that brittle fracture is stress controlled. The shift being larger within the transition region can be linked to the fracture mode changing from brittle to ductile in the DBT region. As the stresses in front of a sharp crack are higher, brittle fracture may occur earlier if a critical flaw is sampled, leading to lower measured values. It is believed that the pre-crack is more sensitive to inhomogeneities and brittle microstructures present in the material, and might therefore result in brittle fracture where the notched samples fail in a more ductile fashion for lower temperatures, as seen in the results from the Charpy testing, the fracture surface investigations and the CTOD measurements. This observation is in agreement with existing theories, as described in Section 3.1.2.

In addition to having higher transition temperatures, the transition between the upper and lower shelf is steeper for the pre-cracked curves, at least for the base material and CGHAZ microstructure. This confirms that the change in fracture mechanism from ductile to brittle is more sensitive to changes in temperature when a flaw with sharper root radius is used, as described in Section 3.1.2. The reason for the difference in the curve steepness in the transition region could also be explained by a sharp crack being more sensitive to defects and inhomogeneities in the material, which will be more pronounced in the DBT region where the fracture can occur by both fracture modes. This will lead to brittle fracture initiation occurring abruptly when the temperature is lowered and dislocations are less prone to move when using a sharp crack. Of the curves where the transition region and upper-shelf are obtained, the notched CGHAZ curve has the widest transition region. The reason for this may also in this case be the microstructure being inhomogeneous, as discussed above, combined with the notch being less sensitive to defects in the material.

6.1.3 Data Scatter

In the base material series, the scatter is small except for within the transition region, as the fracture mode can easily change from specimen to specimen in this region. Also, the SD and RSD are seen to be quite small for the upper and lower shelf for all microstructures tested, showing that the fracture mode is more stable than in the transition region. Almost no scatter was observed for the pre-cracked ICCGHAZ series, suggesting that the low values obtained for this microstructure are correct.

The SD and RSD are lower in the transition region for the notched parallels compared to the fatigue pre-cracked parallels, most likely due to the root radius being larger for a notch. A notch being less sensitive to flaws in the material, leads to the transition region ranging over a larger temperature interval compared to the transition region in curves obtained with fatigue pre-cracked specimens.

In the weld simulated series, especially when the CGHAZ microstructure is tested with notched specimens, the data is scattered for most of the over test temperatures. The weld-simulated specimens have a more heterogeneous microstructure than the base material due to diffusion, formation of new phases and constituents, like martensite, bainite and MA islands, and grain growth during thermal impact. Presence of other

microstructural components and brittle phases has probably resulted in increasing the probability of brittle fracture to occur in the weld-simulated microstructures tested. Brittle phases form a more heterogeneous microstructure and may lead to earlier cleavage fracture initiation, as the transition curves also suggest.

Although a large scatter is associated with the notched CGHAZ series, several curve classes at one single temperature are generally not obtained for the notched parallels. Similar curves for the parallel tests should imply that fracture has occurred by similar fracture mechanisms, and a smaller deviation would be natural to expect. The higher SD obtained for the notched CGHAZ curve could be due to the combination of the presence of a notch and weld simulated material.

When the transition region is narrow, the data scatter is seen to be larger than when the transition region is wide. Also, several curve classes are obtained for a given specimen configuration and test temperature in the transition region. This may be explained by a change in fracture mechanism occurring abruptly and the fracture mode being sensitive to temperature changes in this region. A large scatter in the obtained data at a single temperature suggests that fracture may occur by both ductile and brittle fracture, determined by the flaw size and microstructural features inherent in each of the test specimens. This was clarified from the SEM work performed (Section 5.6), where the fracture appearance changes notably with notch geometry and microstructure at similar test temperatures. When the transition region is narrow, the results may be more sensitive to particles and microstructural inhomogeneities, as the fracture mode can easily vary.

It is evident that the notched samples do not show the same spread in curve shapes at a single test temperature as the pre-cracked specimens. This may be because the transition region is larger when using notched specimens. Here, usually one curve class is obtained for most of the test temperatures, even within the transition region. When a change between curve classes occurs, usually the whole set of parallel tests changes shape and fracture mode. This is believed to be due to the samples being less sensitive to local inhomogeneities due to the stress state in front of a blunt notch compared to a sharp crack.

6.2 Fracture Surfaces

Fracture examination of the selected samples show that initiation occurs at several points along the edge of the fatigue pre-crack and the notch. The fracture initiation points are seen closer to the end of the pre-crack than at the end of a notch. In addition, the pre-cracked samples tend to have a larger portion of ductile areas in-between the areas of cleavage facets compared to the notched specimens with the same microstructure tested at the same temperatures. This can be seen when comparing Figure 5.13 and 5.16 for ICCGHAZ tested at $-30\text{ }^{\circ}\text{C}$ with notch and pre-crack, respectively.

Also, a portion of ductile tearing is seen the cleavage region in Figure 5.13 seen before the faceted area begins. This ductile band only being found in the micrographs of the notched specimens suggests that the stresses are lower in these samples compared to the pre-cracked samples when the hammer impacts the specimens. This may result in some yielding and ductile tearing occurring prior to the onset of cleavage fracture. The ductile band being wider for notched specimens also indicates that fracture initiates earlier when the root radius is decreased.

The width of the area of ductile tearing decreases with decreasing temperature, and is completely gone in most of the specimens tested at low temperature, showing that brittle fracture governs the fracture process at low temperature, as expected. The pre-cracked specimens generally does not have a band of ductile tearing before the cleavage facet area begins, at least not a band that appears continuously along the whole pre-crack border. The reason for this is most likely the increase in stresses in front of the pre-crack compared to the notch leading to the stresses reaching the cohesive strength of the material sooner.

In the the pre-cracked specimens investigated, some initiation points were seen to originate almost from the pre-crack border with river patterns radiating downwards. For the notched specimens, initiation occurs somewhat further away from the notch, and the river patterns are seen to radiate in different directions, including river patterns in the direction back towards the notch interface from the initiation cite. A possible reason why the river patterns can grow in multiple directions in the notched specimens might be that these samples are exposed to lower stresses ahead of the root, so that fracture occurs at a

distance from the notch border where a critical stress level is reached. It might be that the fracture initiating further away from the crack allows for the fracture to proceed in several directions.

The V-notched CGHAZ samples investigated show a more ductile appearance than the other samples. Therefore, cleavage initiation points cannot be found along the notch border. In the micrographs of the V-notched CGHAZ sample tested at $-30\text{ }^{\circ}\text{C}$, dimples with particles were observed, while the sample tested at $-60\text{ }^{\circ}\text{C}$ appeared to be somewhat contaminated, and therefore it is hard to determine the location of initiation points. However, compared to the V-notched ICCGHAZ specimens tested at the same temperatures, the V-notched CGHAZ specimens investigated does show a more ductile appearance. This suggests that the ICCGHAZ microstructure is more prone to fail by a brittle fracture mechanism at higher test temperatures.

However, as only one specimen of three or more parallel tests performed at each test temperature has been investigated in addition to the the fact that the scatter observed is large for several test temperatures, it hard to make generalized conclusions on ICCGHAZ being a more brittle microstructure than the CGHAZ from the SEM micrographs. Nevertheless, the measured CTOD are lower for the ICCGHAZ compared to the CGHAZ values at the same test temperatures (Figure 5.8), which is also the case for the measured C_V values 5.1. This indicates that the ICCGHAZ microstructure is more brittle at the same test temperature compared to the CGHAZ microstructure, ass less energy is absorbed during testing.

6.3 Microstructure

The base material and the weld-simulated specimens investigated are seen to be different in terms of microstructure. The base material has a grain structure, where the microstructure is seen to be more homogeneous compared to the CGHAZ and ICCGHAZ microstructures. The larger scatter observed during testing of the CGHAZ microstructure could be explained by the grain size being large in addition to the microstructure being homogeneous. Testing of the ICCGHAZ did not lead to widely scattered results, which could be explained by the grains not being as large in this microstructure in addition to the microstructure being somewhat more disorganized. Both weld-microstructures consist of bainite and martensite regions that are usually more brittle than other phases.

MA constituents were found to be present in the CGHAZ and ICCGHAZ microstructures, easiest visible in the micrographs obtained using the LaPera etchant (Section 5.7). As described in Section 2.7.2, MA constituents believed to be detrimental to the fracture toughness of the CGHAZ and ICCGHAZ weld regions. As previously discussed in this chapter, the Charpy impact energies and measured CTOD values were found to be lower in the ICCGHAZ compared to the CGHAZ, and a lot lower than for the base material. Most likely, the presence of MA phases in combination with the microstructures being more heterogeneous and the grain size larger, have led to the decrease in fracture toughness for the weld simulated microstructures. The presence of MA constituents were most evident in the ICCGHAZ microstructure (Section 5.7), which may explain this microstructure shows the poorest toughness properties.

As described in Section 2.7.1, MA constituents can be found as blocky particles or stringer-like particles between bainite or martensite laths. From the micrographs obtained, it seems as though stringer-like MA constituents could be present in the CGHAZ, while blocky MA constituents were seen in the ICCGHAZ microstructure. Probably stringer-like particles are present in the ICCGHAZ microstructure as well. How these MA constituents have contributed in fracturing the specimens is hard to determine without having investigated possible fracture mechanisms, like particle-matrix debonding. This has not been studied in the SEM, as studying the location of possible initiation sites has been the focus while working on the SEM.

To be completely confident about the different phases and microstructural constituents present in the specimens investigated, micro-hardness measurements to distinguish between the different ferrite, bainite and martensite areas could be performed in addition to investigations in a SEM to investigate the MA islands and MAC aggregates further. This has not been carried out due to the scope being wide and focus areas of this thesis many.

6.4 Results and Parameters Obtained from Instrumented Charpy Tests

It is clear that the instrumented Charpy test provides additional data compared to the conventional un-instrumented Charpy test. However, the interpretation of these data and how to use them in the best way can be discussed. Some possible trends in how the different portions of the total energy measured, in addition to the energy fractions calculated from these, change with temperature and curve class can be observed. These parameters were investigated in search of ways to describe and quantify different fracture events occurring in the Charpy specimen during testing. Although some general trends were seen related to these parameters, the usefulness of the calculated fractions is somewhat unclear.

6.4.1 Challenges in Curve Class Determination

Which curve class a specific curve from a instrumented Charpy belongs to has sometimes been hard to determine. The appearance of the curves are seen to change gradually from class to class, where some of the curves does not seem to fit the description of neither of the five standard classes. Some of the curves with a shape deviating from the standard class descriptions have characteristics that fit several of the curve classes. For these curves, a final decision has been made based on what is believed to be the most pronounced and important features on the curve obtained.

For the five different curve classes suggested, class I, II and III are obtained for the highest test temperatures and are associated with ductile fracture. Class II and III also features a vertical load drop at brittle fracture initiation. Class IV and V are generally obtained for the lowest test temperatures. The class IV and V have been more challenging to evaluate than curve class I, II and III. This might have led to errors, especially in the calculated fraction values.

For the ICCGHAZ microstructure, where all curves are classified as class V, several of the curves obtained have been hard to classify. Some of the curves classified as class V curves show higher loads and deflection values at the higher temperatures compared to

the class V curves obtained at lower temperatures. Although choosing a lower curve class number might have been more correct for some of these tests, several factors has led to classifying these curves as class V. These factors are mainly the early load drop observed in addition to the curves not being as smooth as the curves of lower classes usually are.

Since the onset of brittle fracture initiation is an important point when considering brittle fracture, the location of this point has been emphasized when categorizing these curves. Making a separate class for curves where F_m is reached before the point of general yield, and where the further fracture path and general shape deviate from the standard class V curves might have been appropriate. This might also have led to less deviations when calculating average fracture values obtained for the different curve classes (Table 5.2).

An example of a class V curves differing slightly from the others and from the general class description, is specimen ss2.77f, where a plateau with constant load can be seen after the load drop from F_m . Some of the curves have quite high deflection and load values compared to the other curves of the same class. The curves with somewhat different appearance are found for the ICCGHAZ material tested at the highest test temperatures. Nevertheless, they have been included in the class V category as the maximum load is reached early, where F_m equals F_u on and the curves have a quite large tail, in addition to the measured energies not being too high. It is therefore unclear whether the fractions for the class V curves are correct in value. However, the fractions are low, as they should be since fracture initiation occurs early, so that the general trend observed seems to be correct.

Also curves classified as class IV show some shape variation, but they all reach maximum loads at small deflection values. In addition, F_m equals F_u . An important factor to consider when evaluating class V and IV curves is that F_m is reached at small deflection values. When this is the case, the 3τ criterion (described in Section 2.9.5) may not have been met. This may have led to to erroneous measures of the maximum load, as the inertia effects might not have been dissipated when F_m was measured.

In order for the $C_{V,f}$ value and the fractions to be correct, it is important that the point on the curves where fracture initiates is determined correctly. Also, finding the right position of the fitted curve through the oscillations is challenging with a lot of oscillations

in the measured data. This may have influenced the final curve shape. The deviations and uncertainty factors linked to the lower curve classes may have influenced the estimated average values of the two fractions, $\frac{C_{V,m}}{C_{V,c}}$ and $\frac{C_{V,f}}{C_{V,c}}$. In addition, the SD and RSD related to these values are most likely strongly influenced by the factors discussed. For instance, the deviation is seen to be large for the class V curves, which may indicate that some of the curves in this class might not really be class V curves.

Another factor affecting the accuracy of the calculated fraction values is the criterion for when the curve cut-off should be made. The cut-off criterion has been at 5 % of the maximum measured load. For some of the class IV and V curves, the load has dropped almost to a value zero after maximum load is reached, but the fitted curve has not reached a low enough value to perform the cut-off until some time later. For some of the curves classified as class IV, it can be seen that a larger portion of energy measured after the onset of brittle fracture than other class IV curves. In addition, most of the class V curves have a large tail after the onset of fracture initiation. It might be that the cut-off should be performed earlier and that this has led to the calculated fraction values for the class IV and V curves to be erroneous. The result would have led to the class IV fractions being too low and the class V fractions being too low.

6.4.2 Distribution of Energies Measured to Maximum Load and Load to Brittle Fracture Initiation With Temperature

The distribution of the energies measured to the onset of brittle fracture initiation, $C_{V,f}$ (Figure 5.4) is seen to resemble the trend observed in the transition curves, where the values are low at low temperatures, and increase as the test temperature is increased. This may be explained by most of the $C_{V,f}$ values being close to the total energies absorbed, with the exception of the curves where early initiation is observed (usually class V). Therefore, the $C_{V,f}$ distribution resembles the trends in shape seen for the transition curves. The distribution of $C_{V,m}$ values is more scattered, but the trend in increasing $C_{V,m}$ with temperature is still evident, although the increase with temperature is not as abrupt. The difference in steepness in the increase in $C_{V,m}$ and $C_{V,f}$ values may be explained by the class I curves not being included in the $C_{V,f}$ plot, as they show a fully ductile behaviour.

Both high and low $C_{V,m}$ values are usually obtained at the same test temperature, as can be seen in the $C_{V,m}$ -T plot (Figure 5.3). This indicates that samples where both ductile and brittle fracture has occurred have been found at the same test temperature. This occurs most frequently at low temperatures for the base material. Also, it can be seen that either high or low $C_{V,m}$ values are obtained, with no intermediate values. This is interesting, and shows that either a large or a small amount of energy is absorbed in the specimen before the highest load is measured. It may suggest that the transition from ductile to brittle fracture mode occur abruptly and that the microstructures tested may be inhomogeneous. This was seen from the transition curves previously discussed and during the microstructural investigations. High and low maximum loads may be measured in the same material due to the material being inhomogeneous, dependent on if the weakest links in the microstructures tested are sampled in front of the crack.

6.5 Change in Energy Fractions with Curve Class

It should be emphasized that the fraction values are obtained using a limited amount of curves. In addition, a different number of values has been used to obtain the average fraction values for the different curve classes, as the number of curves obtained for the separate classes depend on the test results. Therefore the values obtained show varying reliability for the different curve classes. In order to obtain more reliable values of the general fraction values associated with the distinct curve classes, more samples would have to be tested.

The energy fractions were calculated in order to try to quantify some of the trends observed on the curves from instrumented Charpy testing. Although there are uncertainties related to the definition of the curve classes, one trend in observed is that the amount of energy absorbed before maximum load values, $\frac{C_{V,m}}{C_{V,c}}$, increase with increasing curve class number and degree of brittleness, with the exception of class V (Table 5.2). This means that from class I to class II, III and IV, the energy absorbed up to maximum load, $C_{V,m}$, constitute an increasing value of the total calculated C_V . When it is hard determine which class a curve belongs to, this suggests that the $\frac{C_{V,m}}{C_{V,c}}$ fraction may be used in separating the curve classes during class determination. In addition it may also be used when determining the fracture mode experienced in a specimen.

Another trend is the fraction of energy absorbed to brittle fracture initiation, $\frac{C_{V,f}}{C_{V,c}}$, being high for all curve classes. Also in this case with the exception of class V where the fraction values are lower. These trends may indicate that there are different fracture mechanisms and fracture paths governing the fracture process in specimens where a curve class V curve is obtained during instrumented Charpy testing as supposed to when other curves classes are obtained. However, the dynamic oscillations that affects the load measures in the early stages of the instrumented Charpy test may make the results incorrect. These effects are discussed in a later paragraph.

The trends seen in $\frac{C_{V,m}}{C_{V,c}}$ or $\frac{C_{V,f}}{C_{V,c}}$ values (Figure 5.6 and 5.7) give an impression of the fracture processes that may have occurred in a specimen upon testing. An example is the small $\frac{C_{V,f}}{C_{V,c}}$ values obtained for the class V curves that shows that a large portion of the energy has been absorbed after the onset of brittle fracture. This may indicate that a large

portion of the energy has gone into arresting the crack in these specimens, due to the crack driving force being too small. It may also be that a different microstructure with higher arrest toughness is reached, so that further crack propagation has been prevented.

For curve class IV and V, the $C_{V,m}$ and $C_{V,f}$ energies are equal, as brittle fracture initiation occurs at maximum load. These curve classes are obtained at low test temperatures, where brittle fracture is the governing fracture mode. Although the measured C_V energies are low for these curve classes, the fraction of energy absorbed before the onset of brittle fracture initiation, $\frac{C_{V,f}}{C_{V,c}}$ was found to be highest for the class IV and lowest for the class V curves, which suggests that there are different fracture events occurring throughout the test for specimens with class IV and V curves. This may support the assumption that the class IV curves were found in the lower transition region, whereas the class V curves were predominant on the lower shelf, where arrest properties may be of importance for the fracture propagation.

Also, for the class V curves, a larger portion of the total measured C_V energy is obtained after brittle fracture initiation. This shows that little energy is needed to initiate a crack, and suggests that a greater portion of the total absorbed energy has gone into arresting the crack.

6.6 Change in Energy Fractions with Temperature

The distribution of the $\frac{C_{V,m}}{C_{V,c}}$ values plotted against temperature in Figure 5.6 are seen to be somewhat different for the series using pre-cracked and notched specimens. The general trend is that the pre-cracked series have somewhat lower $\frac{C_{V,m}}{C_{V,c}}$ values compared to the notched series for the same microstructure and test temperature. This may indicate that less energy is needed to initiate brittle fracture in pre-cracked specimens. This is at least the case for curve class II and III, where F_m equals F_u .

In addition, the $\frac{C_{V,m}}{C_{V,c}}$ values for the pre-cracked series can be seen to be more stable over the whole test temperature range for the three microstructures tested compared to the notched series. This may confirm that pre-cracked specimens have a higher stress state in front of the crack tip compared to a notch so that the critical fracture stress is reached closer to the crack. This in turn will allow for a smaller material volume to be sampled before brittle fracture is initiated. Another factor that might explain this is the pre-cracked specimens being more sensitive to inhomogeneities present in the material.

For the notched series in Figure 5.6(a), the CGHAZ and ICCGHAZ materials show a decreasing $\frac{C_{V,m}}{C_{V,c}}$ value with temperature. However, the fraction was not seen to stabilize as clearly at one single value for the CGHAZ at the highest test temperatures, and did not stabilize at all for the ICCGHAZ microstructure, as was the case for the base material. This may indicate that the presence of a notch is indeed less sensitive to flaws present in the material, leading to less abrupt changes in the values with temperature. In addition, the values not stabilizing as clearly may indicate that the upper-shelf has not been reached for the temperatures tested. This is also in accordance with trends observed in the transition curves in Figure 5.1, where it can be seen that the upper-shelf is not obtained for neither of the two ICCGHAZ series.

In addition, this shows that the ICCGHAZ microstructure is brittle even at ambient temperatures. For the notched base-material series a significant drop in $\frac{C_{V,m}}{C_{V,c}}$ value were seen between $-137\text{ }^{\circ}\text{C}$ and $-120\text{ }^{\circ}\text{C}$. No other combination of microstructure and flaw geometry were seen to have a comparable abrupt drop in $\frac{C_{V,m}}{C_{V,c}}$ value with temperature.

This drop is in accordance with the location of the Charpy transition region for this specific combination of microstructure and flaw geometry.

The fraction $\frac{C_{V,m}}{C_{V,c}}$ to a certain degree quantifies the trend seen change in curve appearance, and could therefore be used in describing the fracture events governing the total fracture process. When evaluating arrest properties, the $\frac{C_{V,f}}{C_{V,c}}$ fraction may provide useful information, as it is the fraction of the total energy needed to initiate brittle fracture. As discussed before, the fraction is seen to be quite high for class II, III and IV, while the value is low for the class IV curves. This suggests that most of the energy is absorbed after the onset of brittle fracture initiation, possibly in arrest processes.

Measuring the load drop from F_m could also provide information about the arrest properties of the microstructures tested. Also, it would have been interesting to investigate the location of eventual arrest lines to see if the distance from the crack border coincide with the curve class and also if the size of the facets is different in the different curve classes. This load drop has not been estimated in the work performed in relation to this master's thesis, and is suggested as possible areas of investigation for further work. In order to use these values and be able to make more general conclusions, one would have to investigate the trends seen further using more than one material.

6.6.1 The Relation Between SEM Results, Energy Fractions and Curve Classes

The fractions $\frac{C_{V,m}}{C_{V,c}}$ and $\frac{C_{V,f}}{C_{V,c}}$ and the appearance of the curves give an impression of how the fracture process may have proceeded in a specimen. However, it is hard to find a very good relations to the fracture appearance observed in SEM, especially when it comes to the positions of the exact initiation points along the border between the notch or crack and the fracture surface. One reason for this is the many initiation points potentially leading to final fracture of the specimens that.

Nevertheless, a decreasing portion of the fracture surface has a ductile appearance with decreasing temperature. In addition, the distance of the ductile region before the brittle cleavage region is of different length in the specimens investigated. Of the investigated specimens, both of the investigated V-notched CGHAZ only one of the V-notched

ICCGHAZ samples show a ductile band before the cleavage facets begin. The curves without a ductile band are almost all of curve class V, while the investigated specimens with a ductile band stem from class III or IV specimens.

It is believed that the length of the ductile region, the load drop at brittle fracture initiation and the amount of ductile appearance in the specimens may be linked to the curve classes and the parameters like $C_{V,f}$ and the fraction $\frac{C_{V,f}}{C_{V,c}}$ found from instrumented Charpy-testing. It may be that these observations and parameters could be used in describing the fracture events occurring in the specimens and the general trends expected to be seen at the different test temperatures and fracture regimes.

In order to be able to make general considerations and conclusions on this theory, a larger amount of samples should be investigated in a SEM. One of the tasks could be determining length of the portion of ductile fracture occurring before the brittle faceted cleavage area to see if these measurements could be linked to the parameters mentioned above.

6.7 Correlations Used to Relate Charpy Data and Quasi Static Fracture Mechanical Parameters

Minimum C_V values of at least three minimum tests are usually used when using the Charpy test to perform structural assessment evaluations [26, 66]. However, average values of the measured C_V have been used when evaluating the degree of correlation between measured CTOD values and CTOD values estimated from the two Charpy test correlations investigated. As described in the discussion of the transition curves (Section 6.1), this has been done as a general overview of the degree of correlation was desired. The shape of the Charpy transition curves using average and lower bound values are comparable, and as the calculations were only intended to be used in evaluating the agreement between estimated and tested CTOD values using the correlations, and not as a part of a structural assessment procedure, using average values has been considered appropriate.

It should be mentioned that several factors may have lead to the final estimates not being completely correct. One such element is the equation used in converting calculated K_{mat} values to CTOD values (Equation (2.9)) is valid for small scale yielding, where the plastic zone is small. When the Charpy and CTOD values increase, and move towards the transition region, this conversion equation may not be accurate. Also, the crack has been made in different orientations in the Charpy and CTOD specimens, as illustrated in Figure 4.2. As the specimens have been weld simulated prior to testing, the primary microstructure has been altered. Therefore it is believed that the difference in the crack orientation has not influenced the final results for the CGHAZ and ICCGHAZ microstructures to a great extent. The effect might have been larger if the base material were to be tested with different crack orientation in the Charpy and CTOD specimens, as the position of the crack in relation to the rolling direction is important for the measured toughness.

6.7.1 Degree of Correlation of the Lower Bound Relation After BS7910

The lower bound relation for lower shelf and transition behaviour after BS7910 was shown not to provide good estimates of the CTOD from C_V values for the weld-microstructures tested. However, the results obtained are always conservative, meaning that the estimated CTOD values are lower than the actual CTOD values, at least when pre-cracked specimens are used. This is true both for the CGHAZ and ICCGHAZ microstructures. Here, the estimated CTOD is seen to follow the increase in the measured CTOD to some extent. The notched series are not seen to correlate with the real CTOD data at all, which can be linked to the scatter in the measured results, that are generally larger for the notched parallels, as can be seen in Table (5.3).

It is evident that using pre-cracked specimens as opposed to notched specimens makes the CTOD estimates conservative, and show a somewhat better degree of correlation, where more conservative results is equivalent to lower estimated CTOD values, i.e. safer estimates are generated. The difference between the notched and the pre-cracked series becomes more pronounced with increasing temperature, where the notched series does not continue to provide strictly conservative. The reason for this may be that the C_V values measured for the notched series are higher for higher test temperatures, and may then no longer, at least not for the highest test temperatures, represent values within the lower transition and lower shelf regime. If the C_V values are outside the lower part of the transition curve, the lower bound relation should not be used, as the estimates provided will not be valid.

It would have been interesting to see if the tested correlation were to provide a better degree of correlation if data for base material were to be used. This would validate or invalidate if the microstructures tested being inhomogeneous that makes the degree of correlation far from satisfactory, or if the relation also provides a bad fit for a more homogeneous microstructure as well. Unfortunately, CTOD results for the base material have not been available.

6.7.2 Degree of Correlation of the Master Curve

When using the MC to predict CTOD values based on the Charpy test is generally not seen to provide a curve that fits all of the measured CTOD values perfectly (Figures presented in Section 5.8.2). However, the correlation is seen to have a better degree of correlation than the lower bound correlation after BS7910 previously discussed, somewhat depending on the parameters used.

When using the MC, most measured CTOD values fall well below the upper confidence limit ($P_f = 0.98$), although the CTOD values estimated are generally too high for the ICCGHAZ microstructure, falling between the median and lower tolerance bound ($P_f = 0.632$ and 0.02). The correlation is seen to be best for the ICCGHAZ material when the T_0 is estimated from the equation given in BS7910 (Figure 5.25, Equation (4.5)). For the CGHAZ microstructure, the CTOD values fall both below and above the higher and lower tolerance bound, which shows that the degree of correlation is not very good. However, few of the CTOD values fall below the lower tolerance bound, which is more important for low temperature applications.

The reason why the correlation provides a somewhat better estimate for the ICCGHAZ may be explained the larger data scatter seen in the estimated CTOD values and C_V values. This may be linked to the difference in microstructure observed. For the curves estimating T_0 from Wallin's equation (Equation (4.6)), the measured CTOD values lie below or on the lower tolerance bound for the ICCGHAZ material, providing a lower degree of correlation. It is seen to provide a better degree of correlation for the CGHAZ microstructure. The reason for this is the very low T_0 values obtained using this equation, leading to the estimated CTOD values being higher and the distance between the upper and lower tolerance bounds being wider so that the highly scattered CTOD values measured for the GCHAZ material fit within the bounds. However, this equation is seen to provide too high CTOD values for the ICCGHAZ where the scatter is less pronounced.

For most of the curves generated for the ICCGHAZ microstructure included in Section 5.8.2, the estimated CTOD values are too high compared to the real CTOD values, which is not good if the MC were to be used in structural assessment for the given steel. However, the MC is developed for more homogeneous microstructures than the weld simulated microstructures tested, so that this result may only indicate and confirm that the correlation is indeed not to be used for inhomogeneous microstructures, unless one can find a way to correct for this in the equations for estimating T_0 and K_{mat} .

In addition, the MC is to be used for the temperature range ± 50 celsius [90], a temperature range with temperatures higher than most of the test temperatures used during testing. The CTOD tests has been performed at temperatures mainly on the lower shelf, and not the lower transition region, where the MC may have provided a better estimate of the measured CTOD values. How the temperature parameters in the MC correlation, T_0 and T_k are obtained influence the estimated K_{mat} values. Better estimation procedures and explanations of how to estimate these from Charpy data may contribute to the MC providing a better degree of correlation to real values of fracture mechanical parameters obtained from quasi-static testing. Estimation procedures for parameters might also be developed so that the MC correlation could be used for weld microstructures as well.

Effect of the Parameter T_k in the MC

The parameter T_k in Equation (4.7) is seen to have a significant impact on how well the MC provided a good fit for the measured CTOD values or not, where the estimated CTOD values in the MC are seen to decrease with increasing T_k . For the ICCGHAZ microstructure, the correlation that were shown to provide the most fitting estimate when a T_k value of 25 was used. When a value of 0 was used, the lower validity curve with P_f 0.05 was found to lie above most of the measured CTOD values for the ICCGHAZ series. When T_k were set to 25, the measured CTOD values were located within the tolerance bounds, although towards the lower tolerance limit.

The difference between including and not including T_k in the MC is notable, showing that it is important to consider how the T_k value affect the MC estimates when evaluating the degree or correlation. This parameter also influences how conservative the CTOD estimates are. Therefore, the meaning of T_k should be investigated further to find a optimum value or an equation for calculating such a value for a given steel. The

recommendation of using a T_k of 25 is not well reasoned for in the standards, and may not be the best value to use for the investigated material and test situation.

It has not been found any literature on the development and descriptions of the T_k parameter used. More information about this parameter would have been useful when discussing the use of T_k in the equation and why it is included in BS7910 and not included in ASTM E1921, as this parameter seems to improve the degree of correlation of the MC to a certain extent. This being true for the specific microstructures of the steel alloy investigated.

Discussions of the Equations used in Estimation of T_0 Used in the MC

The estimation procedure used in determining T_0 was also seen to affect the degree of correlation between estimated and measured CTOD values. The estimation of T_0 from CVN data is not very well defined in the standards, which makes accurate estimates difficult to obtain, at least for the curves where the upper shelf is not obtained during testing. According to BS7910 Equation (4.5) should be used when determining the T_0 to be used in the calculation of K_{mat} using the MC correlation, while it is only used as a first estimate of the start test temperature in estimation T_0 from quasi-static fracture mechanical testing, according to ASTM E1921.

As the MC has a similar shape for all ferritic steels, where the position of the curve is determined by T_0 , a different definition of the T_0 will lead to the MC being positioned differently. Hence, using the two standards to estimate CTOD values may provide a different result and a different fit to the measured CTOD values for the same steel, which is unfortunate. However, the start temperature in T_0 estimations should be chosen quite close to the actual T_0 , so that the deviations should not be that far apart if the procedures and testing has been done correctly according to ruling standards.

Equation (4.5) uses TC_{V27J} in the estimation, where the measured energies are very low, and most of the curves have reached the lower shelf region. The estimated T_0 values are lower than the TC_{V27J} values. A high T_0 value used in the MC leads to the estimated CTOD values being lower and to more conservative predictions. The fact that the CTOD estimates decrease with increasing T_0 values can be explained from the correlation equation (Equation (4.7)). If the T_k term is set to zero, as it appears in ASTM

E1921, the exponential term will be less than unity if the estimated T_0 is lower than the test temperature. Hence, the estimated K_{mat} will be reduced compared to a situation where the estimated T_0 is lower than the test temperature. Here, the exponential term will be above unity, and the estimated K_{mat} will be higher.

As the fracture toughness is closer to the upper shelf when T is above T_0 and closer to the lower shelf when T is below T_0 , the estimated CTOD being higher for higher test temperatures and lower T_0 values is a reasonable result and shows that the MC behaves as it should for different T_0 values. It is important that the correlation does not predict too high fracture toughness values when the test temperature is below T_0 and brittle fracture may occur. In this regard, one would like to estimate a T_0 as correctly as possible. If too low T_0 values are used, most of the test temperatures will be above T_0 leading to the exponential term being above unity and the predicted CTOD or (K_{mat}) values may be too high.

Although T_0 is just a reference temperature used in the MC, and not directly connected to the ductile-to-brittle transition temperature, T_{trans} or DBTT, it is interesting to see that the actual DBTT estimated from the Charpy transition curves clearly shows that the T_{trans} of the steel is well above both TC_{V27J} and T_0 . This can be seen from looking at the curves in Figure 5.1 and the values summarized in Table 5.4.

It is important to consider the value of T_0 used in the MC correlation, as using a far too low T_0 value results in the correlation not really imaging the real situation and may position the MC incorrectly for the steel of interest. As one would like to avoid brittle fracture from occurring, it is important to provide conservative estimates. In this regard, it is interesting that the standards leads to quite low T_0 values, far lower than the T_{trans} of the given steel. At least this seems odd since it does not result in the results being more conservative or the degree of correlation being better. Both of the tested equations used in determining T_0 provide quite low values, where the equation developed by Wallin (Equation (4.6)) provides the lowest T_0 values.

It is suggested that an equation for calculating T_0 from CVN data more accurately should be developed in order to make sure that the MC can be used when predicting CTOD and other fracture mechanical parameters accurately from Charpy data. As lower CTOD

estimates are generated when using higher T_0 values, the T_0 value used is of importance, especially if the MC is to be used for structural assessment purposes. Maybe the T_{trans} temperature could be used in determining T_0 to be used in the MC in order to obtain a better procedure for T_0 determination from CVN test data than the procedures included in the two standards investigated.

Data Obtained from Pre-cracked Specimens in the MC

Although the MC correlation is developed for standard CVN specimens with a notch, constants to be used in determination of the start test temperature from pre-cracked Charpy specimens was found in ASTM E1921, where a higher C-value of 50 is recommended instead of a value of 18 used for standard CVN specimens. This allows for determining T_0 and the location of the MC for pre-cracked specimens, where the estimated T_0 has a lower value than the T_0 estimated for notched specimens at the same test temperature. However, as the pre-crack correction in ASTM is mainly used in obtaining a start temperature for CTOD testing, and not directly as a part of the equation estimating K_{mat} , and not at all included in BS7910, the use of the parameter is somewhat unclear. Nevertheless, the test results show that a lower T_0 temperature shifts the position of the MC to lower CTOD values.

The estimated T_0 are lower for the pre-cracked specimens compared to the notched specimens when different C-values are used. Using a higher C-value for pre-cracked specimens seems reasonable, since the pre-crack specimens are seen to behave brittle at higher test temperatures compared to the notched specimens, based on lower CTOD and C_V values obtained during testing with pre-cracked specimens. When comparing the microstructures tested, the correlation is seen to provide a somewhat high CTOD estimate for the ICCGAZ microstructure although most of the CTOD values fall within the tolerance bounds for the pre-cracked specimens. The large scatter associated with the CGHAZ microstructure makes the tolerance bounds too narrow for all the CTOD values to fit. Hence, the MC correlation provides a somewhat better estimate of the CTOD for the ICCGAZ microstructure compared to the CGHAZ microstructure, the same trend as observed for the notched specimens.

Although using a higher C-value for pre-cracked specimens seems reasonable, the reason why the specific values of the constant C in Equation (4.5) is set to 18 for the notched and 50 for the pre-cracked series is not outlined in the standards, and it has been difficult to find literature describing this parameter. This makes discussing the use of the C-parameter more extensively challenging. The MC correlation is most likely not originally developed for correlating CTOD and C_V values from using pre-cracked specimens, and the changed C-value might not be sufficient in making the MC predict CTOD values correctly for pre-cracked specimens.

In addition to have one C-value for pre-cracked and notched specimens, it might also have been useful to investigate if the C-parameter could be used in making the MC estimate values for inhomogeneous microstructures better. Maybe the C-value should be the same for all microstructures in order to provide better CTOD estimates, as the different microstructures tested behave somewhat differently, especially considering the difference in associated scatter.

Although it is difficult to make general conclusions based on a single test series for one steel type, it can be concluded that the using the pre-crack correction in the MC correlation seems generate curves with trends comparable to the curves obtained using data from the notched specimens. The fact that using pre-cracked specimens show the same trend as when notch specimens were used is clear. The similarities are the MC predicting too high CTOD values for upper confidence limit for the ICCGHAZ microstructure, while the lower tolerance bound seem to provide a better degree of correlation. In addition, the distance between the upper and lower tolerance bound is too large. The tolerance bounds are too narrow to fit all of the measured CTOD values from testing of the CGHAZ microstructure.

These similarities may indicate that the MC could possibly be used for pre-cracked specimens also if the correlation is improved, in order to be used for more inhomogeneous microstructures. However, this should be tested in a larger scale before general conclusions can be made, as the MC relation does not originally take effects of the presence of a pre-crack into account. In addition, the microstructures tested are not commonly used in obtaining correlations, which also have to be taken into account.

6.7.3 Comparison of the Lower Bound Relation After BS7910 and the Master Curve Correlation

None of the correlations are seen to predict measured CTOD values correctly, although the values estimated are or the same order of magnitude as the CTOD values obtained during testing. The MC correlation is seen to provide a somewhat better estimate, at least for the ICCGHAZ microstructure, compared to the lower bound method after BS7910. The reason for this may be that fracture is considered a weakest link phenomenon, where a P_f is included in the correlation in addition to making use of a reference temperature, T_0 , and not only the test temperature. Although scatter in fracture mechanical data could be accounted for, the correlation is not seen to provide good CTOD estimates for the CGHAZ microstructure, where the scatter in test data is large.

The lower bound method uses the C_V value directly, and parameters other than the specimen thickness cannot be varied. This may make it hard to account for the scatter related to fracture mechanical testing into consideration, and may be one reason why the correlation does not show good degree of correlation with the real measured CTOD values. However, determining the different variables and constants in the MC correlation is not straightforward. It seems as though better estimates for the parameters in the MC approach would have been useful in providing better a better correlation, at least for the microstructures tested. In addition, the standards should describe the different parameters used, like T_k and T_0 including their meaning and how to select appropriate values in a better way.

It is clear that using Charpy data when estimating CTOD or K_{mat} values are not straightforward when using the selected methods investigated. As most correlations, the ones investigated are most likely developed using the standard notched Charpy specimens. Hence, they do not account for the effect of introducing a pre-crack. As the correlations are not developed for this specimen configuration, the results from using data from pre-cracked specimens in the correlations may not provide correct CTOD estimates. If the instrumented Charpy test were to be used more regularly in CTOD estimation and structural assessment, a separate standard including correlations and different procedures in obtaining the information of interest using pre-cracked specimens would be needed.

The fact that the microstructures tested are not commonly used in obtaining fracture mechanical correlations may be a reason for the poor degree of correlation observed. The correlations tested are most likely primarily fitted for more finely grained base materials. Therefore, using other more coarse grained materials, like the CGHAZ and ICCGHAZ investigated, will result in a lower degree of compliance.

Although it might be hard to overcome the inherent challenges connected to testing of inhomogeneous materials, the test results show that the investigated correlations does not predict CTOD values too far from the real values if the right parameter combination is used, at least for the steel tested. If several steel types were to be tested, one might be able to develop more reliable correlations for certain inhomogeneous microstructures also.

6.7.4 Use of Instrumented Charpy Test Data in Obtaining Fracture Mechanical Parameters

It is proposed that the calculated energy fractions provide information that could possibly be used in obtaining correlations between data from instrumented Charpy testing and fracture mechanical parameters, like the CTOD. The increase in $\frac{C_{V,m}}{C_{V,c}}$ values with curve class, presented in Figure 5.5(a) resembles the trend in CTOD plotted against temperature, seen in Figure 5.8. This might suggest that it could be possible to obtain a correlation between $\frac{C_{V,m}}{C_{V,c}}$ and fracture mechanical parameters, for example CTOD.

If a good relation between these two parameters were found, testing a large number of samples in order to obtain a transition curve and the temperature at a specific energy level could have been avoided. Using the curve generated during the instrumented Charpy test could then be used to estimate the CTOD from a single test, if a good correlation were to be developed. The value of $\frac{C_{V,m}}{C_{V,c}}$ might also say something about how close to the transition temperature a test is recorded, which is often required information in structural assessment procedures. Hence, using the additional data provided by performing an instrumented test could be useful in lowering costs associated with testing a large number of samples or performing expensive quasi-static tests.

This approach would also have avoided a longer sequence of equations, as has been a challenge when using the MC in estimating CTOD values from C_V values. Estimating different parameters like T_0 and T_k is seen to be a challenge when obtaining good correlations. Avoiding use of similar parameters and approaches could have provided more confidence in fracture parameter estimates made from Charpy data. The more terms on the way to the final estimate, the more insecurity may be introduced. Using a single equation where $\frac{C_{V,m}}{C_{V,c}}$ values or other parameters found in the instrumented Charpy test are included, may also possibly overcome the challenges faced in testing different microstructures. The reasoning for this is that the fraction of energy measured to maximum load or brittle fracture initiation is given by the curve generated during the test. This will be a result of the properties of the microstructure tested.

Normally, correlations are divided into areas of applicability, usually valid only for lower-shelf, transition region and upper-shelf behaviour. Finding a correlation that could be used for the whole range of temperatures would have been useful. In this regard, using the $\frac{C_{V,m}}{C_{V,c}}$ or $\frac{C_{V,f}}{C_{V,c}}$ fractions in obtaining a more universally applicable correlation could be a possible solution. It would certainly have been interesting to investigate this idea further with more materials and data, to see if it is even possible to go through with.

7 Conclusions

In the present master's thesis, brittle fracture initiation and toughness at low temperatures have been investigated for CGHAZ and ICCGHAZ microstructures of a 420 MPa HSLA steel. Scanning electron microscopy has been performed to evaluate crack initiation sites and fracture mode, while the microstructures have been investigated by using optical light microscopy on samples etched with Nital and LaPera etchants. In addition, data obtained during instrumented Charpy testing have been evaluated. Also investigated are two possible correlations to be used in obtaining fracture mechanical data, usually obtained during quasi-static tests, to data obtained from Charpy impact testing.

From this, the following conclusions can be drawn:

- **Fracture Initiation and Microstructure**

- * MA constituents were found in the weld-simulated microstructures, most evident in the ICCGHAZ microstructure. The weld-simulated microstructures are more inhomogeneous than the base material and have a coarser grain structure, especially the CGHAZ microstructure. In addition, the weld-simulated microstructures consist mainly of martensite and bainite.
- * Several initiation sites were found close to the notch and fatigue pre-crack in the investigated fracture surfaces. For specimens with a pre-crack, the initiation sites were seen to occur closer to the fatigue crack than in the notched specimens tested at the same temperature for the same microstructure. This is believed to be a result of the higher stress state in front of a sharp crack compared to a blunt notch.
- * The notched specimens show a more ductile appearance compared to the pre-cracked specimens at the same test temperature. A ductile region was found in front of the cleavage area in the samples tested at the highest test temperatures.

• **Charpy Transition Curves**

- * The fracture toughness of the investigated steel is clearly deteriorated when subjected to welding. The fracture toughness was found to be lowest for the ICCGHAZ microstructure tested. The transition temperature of the steel was found to be close to room temperature in as-welded condition. Therefore, the steel is not safe to be used in as-welded condition for low temperature applications, as would certainly be revealed by today's standards. Therefore, it should not be considered a candidate to be used in the Arctic region.
- * The Charpy transition curves obtained for the investigated steel are moved towards higher temperatures with increasing weld thermal cycles and with increasing root radius of the flaw induced in the material. This shows that the transition temperature increases and fracture toughness of the investigated steel decreases with an increasing number of weld cycles and when using a fatigue pre-crack instead of the conventional notch.
- * The deteriorated fracture toughness is linked to the weld microstructures being more heterogeneous and to the MA phases found in these. The fracture resistance is most likely lowered when using a pre-crack due to the higher stress state in front of the sharp crack, compared to the blunt notch in addition to the sharp crack being more sensitive to inhomogeneities in the material.
- * For the three microstructures tested, the difference in fracture toughness between the notched and pre-cracked parallels were found to be largest within the transition region. The notched parallels have a lower transition temperature.
- * For the three microstructures tested, the upper and lower shelf values are comparable for the notched and pre-cracked parallels. The upper shelf plateau was found to be lower in the weld-microstructures tested compared to the base material.
- * The scatter was found to be large within the transition region for all combinations of microstructure and notch sharpness. The microstructure with the overall largest scatter was found for the CGHAZ microstructure, probably due to the large grain size and inhomogeneous microstructure. The data was found to be more scattered

when testing notched specimens compared to the pre-cracked specimens, probably due to the sensitivity of a sharp crack due to a higher stress level close to the crack.

- **The Instrumented Charpy Test**

- * It is clear that the instrumented Charpy test provides additional data compared to the conventional un-instrumented Charpy test usually performed.
- * A change in absorbed energies to maximum load and to load at brittle fracture initiation with temperature was observed, where the trend resembled the increase seen in the transition curves.
- * The fraction of energy measured to maximum load was found to increase with curve class number, with the exception of the class V curves. The fraction of energy measured to brittle fracture initiation were generally high, also with the exception of the class V curves. This suggests that a large portion of energy has gone into arresting the crack rather than to initiate brittle fracture in specimens where a Class V curve is recorded.
- * The curve classes obtained at the lowest test temperature show signs of early fracture initiation. It has been challenging to classify some of these curves. The validity of these curves are also uncertain due to the early fracture initiation and the criterion used to determine where perform a cut-off of the load detected during testing.

- **Correlations**

- * The lower bound relation after BS7910 was shown not shown to provide a good coefficient of correlation for the microstructures tested. However, too conservative results were obtained for the pre-cracked parallels where the correlation seemed to provide the best coefficient of correlation.
- * The Master Curve relation was seen to provide better estimates of the CTOD. The degree of correlation was best for the ICCGHAZ microstructure tested, although the upper confidence limit estimated too high values of the fracture toughness (or CTOD).
- * The parameters used in obtaining the final fracture toughness estimate were shown to have a large impact on the degree of correlation. A difference in how the two

standards investigated, ASTM E1921 and BS7910, define some of these parameters were also found. The parameter T_k is not included in BS7910. In addition the ASTM standard includes a way to account for using pre-cracked specimens which is not mentioned in BS7910. The definition of the parameter T_0 used to find the right position of the MC is not identical in the two standards either. Better procedures and explanations of the parameters used in obtaining the final fracture toughness estimates were proposed to be made.

- * A suggestion in using data obtained from instrumented Charpy testing in obtaining better correlations was proposed. The shape of the increase in absorbed energy to maximum load with curve class number was seen to resemble the increase in CTOD values found. Obtaining a correlation using could be possible.

8 Suggestions for Further Work

- **Investigation of Fracture Arrest**

Investigation of fracture arrest properties and how the instrumented Charpy test could reveal information about this.

- * Measuring load drop on curves from instrumented Charpy curves. See how the size of the load drop varies with temperature, notch geometry and possibly with curve class.
- * Looking for arrest lines on fracture surfaces from instrumented Charpy tests and measure the distance from the end of the notch or pre-crack.

- **Further Surface Investigation**

- * Investigation of MA phases in a SEM to confirm what has been observed using optical light microscopy.
- * Looking for arrest lines on fracture surfaces from instrumented Charpy tests.
- * Investigate a larger number of samples in order to be able to say something more general about how the fracture appearance changes with temperature and notch geometry.

- **Further Microstructural Investigations**

- * Perform micro-hardness measurements to verify the presence of different phases throughout the material.
- * Investigation of the influence of the MA phases and what causes the fracture toughness to be degraded by their presence. This should include investigating possible fracture mechanisms caused by the presence of MA-phases, like de-bonding and residual stresses in the material.

- **Further Investigation of Parameters Obtained from Instrumented Charpy Tests**

- * Investigate the trends found in $\frac{C_{V,m}}{C_{V,c}}$ and $\frac{C_{V,f}}{C_{V,c}}$ with more data included to see if the findings represent a more general trend. Here, results could be separated not only by notch geometry, but also by means of microstructure to see if that will have an effect of the average fraction values obtained for each of the curve classes.
 - * Testing more specimens and steels in order to verify trends in changes observed in $C_{V,m}$ and $C_{V,f}$ with temperature.
 - * Evaluate if there is a better way to classify the curves obtained at the lowest test temperature, where fracture initiates early. In addition, how one should evaluate the curves where fracture initiates before the 3τ criterion is satisfied could be investigated further.
- **Improving and Developing Correlations**
- * If the correlations investigated were to provide a better degree of correlation for the weld-microstructures tested, a different approach to estimate the temperature parameters T_k and T_0 should be developed, in addition to a better approach when using pre-cracked Charpy specimens. Finding these kind of equations and improving the correlations is time consuming, but would have been valuable on the path towards making fracture toughness estimations less costly by using the Charpy test with increased reliability.
 - * Investigate if it is possible to obtain a correlation using the fraction of energy to maximum load, $\frac{C_{V,m}}{C_{V,c}}$ or just the value of the energy to maximum load, $C_{V,m}$.

Bibliography

- [1] K. J. Bird, R. R. Charpentier, D. L. Gautier (CARA Project Chief), D. W. Houseknecht, T. R. Klett, P. J. K., T. E. Moore, C. J. Schenk, M. E. Tennyson, and C. J. Wandrey, *Circum-Arctic resource appraisal: Estimates of undiscovered oil and gas north of the Arctic Circle*. US Department of the Interior, US Geological Survey, 2008.
- [2] A. J. Dahl, "Arctic oil and gas," *The ARCTIS Database*, 2010. [Online]. Available: "<http://www.arctis-search.com/Arctic+Oil+and+Gas#>"
- [3] D. L. Gautier, K. J. Bird, R. R. Charpentier, A. Grantz, D. W. Houseknecht, T. R. Klett, T. E. Moore, J. K. Pitman, C. J. Schenk, J. H. Schuenemeyer, K. Sørensen, M. E. Tennyson, C. V. Zenon, and C. J. Wandrey, "Assessment of undiscovered oil and gas in the Arctic," *Science*, vol. 324, no. 5931, pp. 1175–1179, 2009.
- [4] A. Bishop, C. Bremner, A. Laake, C. Strobbia, P. Parno, and G. Utskot, "Petroleum potential of the Arctic: Challenges and solutions," *Oilfield Review*, vol. 2011, no. 22, p. 4, 2010.
- [5] B. J. Paaske, P. N. Hoffmann, H. P. Dahlslett, and E. al., "Dnv gl: A broader view the Arctic – the next risk frontier," *Managing risk, building trust - DNV GL'S past, present and future*, 2014. [Online]. Available: "<http://www.dnvgl.com/Images/The%20Arctic%20FINAL%20lowres.pdf>"
- [6] SINTEF, "Arctic materials," accessed: 02.02.14. [Online]. Available: <http://www.sintef.no/Projectweb/Arctic-Materials/>
- [7] U. E. I. Administration, "Arctic oil and gas reserves," 2012, (Accessed: 25.04.14). [Online]. Available: "<http://www.eia.gov/todayinenergy/detail.cfm?id=4650>"
- [8] ISO, "Petroleum and natural gas industries—Fixed steel offshore structures," *EN ISO 19902:2007*, December 2007.
- [9] D. François, A. Pineau, and A. Zaoui, *Mechanical Behaviour of Materials, Volume II: Fracture Mechanics and Damage*, ser. Solid Mechanics and Its Applications. Springer, Editor: G. M. L. Gladwell, 2013, vol. 191.
- [10] H. K. D. H. Bhadeshia and R. W. K. Honeycombe, *Steels: Microstructure And Properties*, ser. Metallurgy and Materials Science Series. Elsevier Science & Tech, 2006.
- [11] J. K. Solberg, "Teknologiske metaller og legeringer." Trondheim, Norway, 2010.

- [12] S. Moeinifar, A. H. Kokabi, and H. R. Madaah Hosseini, "Influence of peak temperature during simulation and real thermal cycles on microstructure and fracture properties of the reheated zones," *Materials & Design*, vol. 31, no. 6, pp. 2948–2955, 2010.
- [13] W. D. Callister, *Materials Science and Engineering: An Introduction, 7th Edition Binder Ready Version*. USA: John Wiley & Sons Canada, Limited, 2007.
- [14] D. F. Askeland, P. Fulay, and W. Wright, *The science and engineering of materials (International student edition)*. Cengage Learning, 2008.
- [15] A. Hurlich, "Low temperature metals," in *Proceedings of the 1968 Summer Study on Superconducting Devices and Accelerators*, 1968, pp. 311–325, First published in 1963.
- [16] E. Østby, C. Thaulow, and O. M. Akselsen, "Fracture toughness scatter and effect of constraint in weld thermal simulated HAZ microstructures at -60°C ," in *Offshore Proceedings of the Twenty-first (2011) International Offshore and Polar Engineering Conference*, vol. 4. Maui, Hawaii: ISOPE, 2011, pp. 443–448.
- [17] C. Zhongxiao, C. Zigang, X. Shaoshan, L. Zhaoqi, D. Jiexiang, D. J. H. Machine, and B. Factory, "The effect of MA constituent on toughness in the HAZ of low temperature 12Ni3MoV steel," in *Welding research: the state of the art: proceedings of the JDC University Research Symposium, 1985 International Welding Congress held in conjunction with ASM Materials Week '85, Toronto, Ontario, Canada, 15-17 October 1985*. ASM International, 1986, pp. 113–122.
- [18] "Metallography and microstructures," *ASM Handbook Volume 9*, 2005.
- [19] G. E. Totten and M. A. H. Howes, *Steel Heat Treatment Handbook*. CRC Press, 1997.
- [20] M. Takahashi and H. K. D. H. Bhadeshia, "Model for transition from upper to lower bainite," *Materials Science and Technology*, vol. 6, no. 7, pp. 592–603, 1990.
- [21] O. M. Akselsen, *Transformation Behaviour*, Trondheim, 2012, ch. 15.
- [22] T. Kobayashi, *Strength and Toughness of Materials*. Japan: Springer Japan, 2004.
- [23] T. L. Anderson, *Fracture Mechanics: Fundamentals and Applications, Third Edition*. Taylor & Francis, 2005.
- [24] J. F. Knott, *Fundamentals of Fracture Mechanics*. Butterworths, 1973.
- [25] Y. Li and T. N. Baker, "Effect of morphology of martensite–austenite phase on fracture of weld heat affected zone in vanadium and niobium microalloyed steels," *Materials Science and Technology*, vol. 26, no. 9, pp. 1029–1040, 2010.
- [26] K. Wallin, *Fracture Toughness of Engineering Materials: Estimation and Application*. Emas Publishing, 2011.
- [27] F. Beremin, A. Pineau, F. Mudry, J.-C. Devaux, Y. D'Escatha, and P. Ledermann, "A local criterion for cleavage fracture of a nuclear pressure vessel steel," *Metallurgical Transactions A*, vol. 14, no. 11, pp. 2277–2287, 1983.

- [28] X.-K. Zhu and J. A. Joyce, "Review of fracture toughness (G, K, J, CTOD, CTOA) testing and standardization," *Engineering Fracture Mechanics*, vol. 85, no. 0, pp. 1–46, 2012.
- [29] "Standard test methods for notched bar impact testing of metallic materials," *ASTM Standard E23 – 12c*, November 2012.
- [30] R. Hertzberg, R. Vinci, and J. Hertzberg, *Deformation and Fracture Mechanics of Engineering Materials, 5th Edition*. John Wiley & Sons, Incorporated, 2012.
- [31] G. E. Dieter and D. Bacon, *Mechanical metallurgy*, 3rd ed. McGraw-Hill New York, 1986, vol. 3.
- [32] S. M. Han, G. Feng, J. Y. Jung, H. J. Jung, J. R. Groves, W. D. Nix, and Y. Cui, "Critical-temperature/Peierls-stress dependent size effects in body centered cubic nanopillars," *Applied Physics Letters*, vol. 102, no. 4, p. 041910, 2013.
- [33] R. O. Ritchie, "The conflicts between strength and toughness," *Nature materials*, vol. 10, no. 11, pp. 817–822, 2011.
- [34] R. I. Stephens and H. O. Fuchs, *Metal fatigue in engineering*, second edition ed. Wiley, 2001.
- [35] "Standard test method for linear-elastic plane-strain fracture toughness K_{Ic} of metallic materials," *ASTM Standard E399*, November 2012.
- [36] A. F. Liu, *Mechanics and Mechanisms of Fracture: An Introduction*. USA: ASM International, 2005.
- [37] S. Machida, T. Miyata, M. Toyosada, and Y. Hagiwara, "Study of methods for CTOD testing of weldments," *Fatigue and Fracture Testing of Weldments, ASTM Special Technical Publication, Philadelphia, PA*, pp. 142–16, 1990.
- [38] O. M. Akselsen, J. K. Solberg, and Ø. Grong, "Effects of martensite-austenite (MA) islands on intercritical heat affected zone toughness of low carbon microalloyed steels," *Scand. J. Metall*, vol. 17, pp. 194–200, 1988.
- [39] O. M. Akselsen, Ø. Grong, and J. K. Solberg, "Structure-property relationships in intercritical heat affected zone of low-carbon microalloyed steels," *Materials science and technology*, vol. 3, no. 8, pp. 649–655, 1987.
- [40] C. Chen, W. Li, and H. Peng, "Investigation on MA constituent in weld CGHAZ of high-strength microalloyed steel," in *Materials Science Forum*, vol. 575. Trans Tech Publ, 2008, pp. 690–695.
- [41] C. L. Davis and J. E. King, "Cleavage initiation in the intercritically reheated coarse-grained heat-affected zone: Part i. fractographic evidence," *Metallurgical and materials transactions A*, vol. 25, no. 3, pp. 563–573, 1994.
- [42] D. P. Fairchild, "Fracture toughness testing of weld heat-affected zones in structural steel," *Fatigue and Fracture Testing of Weldments, ASTM STP*, vol. 1058, pp. 117–141, 1990.

- [43] K. Easterling, *Introduction to the Physical Metallurgy of Welding*, 2nd ed. London; Boston: Butterworths, 1992.
- [44] A. C. Palmer and R. A. King, *Subsea pipeline engineering*. PennWell Books, 2004.
- [45] TWI, "What is the difference between the various carbon equivalent formulae used in relation to hydrogen cracking?" *TWI Technical Knowledge – Material FAQs*, 2013, accessed: 11.04.14. [Online]. Available: "<http://www.twi-global.com/technical-knowledge/faqs/material-faqs/faq-what-is-the-difference-between-the-various-carbon-equivalent-formulae-used-in-relation-to-hydrogen-cracking/>"
- [46] "Standard specification for structural steel shapes," *ASTM Standard A992 A992M – 11*, May 2011.
- [47] A. B. of Shipping, "Rule requirements for materials and welding 2000, part 2," *Supplementary Requirements for Naval Vessels*, 2000.
- [48] J. Elmer and J. Wong, "Welding science: A new look at a fundamental technology," 2001, (Accessed: 25.04.14). [Online]. Available: "<https://www.llnl.gov/str/November01/Elmer.html>"
- [49] S. Data, "HSLA 100 steel," *Database of Steel Transformation Diagrams*, 2010, (Accessed: 29.05.14). [Online]. Available: "<http://www.steeldata.info/std/cct/html/2684.html>"
- [50] R. M. Denys, "Wide-plate testing of weldments: Part II wide-plate evaluation of notch toughness," *Fatigue and Fracture Testing of Weldments, ASTM STP*, vol. 1058, pp. 174–203, 1990.
- [51] A. P. Institute, *Recommended Practice for Reproduction Qualification for Steel Plates for Offshore Structures*. Washington DC: American Petroleum Institute, 1987, vol. 2Z.
- [52] J. Liao, K. Ikeuchi, and F. Matsuda, "Toughness investigation on simulated weld HAZs of SQV-2A pressure vessel steel," *Nuclear Engineering and Design*, vol. 183, no. 1, pp. 9–20, 1998.
- [53] J. H. Chen, Y. Kikuta, T. Araki, M. Yoneda, and Y. Matsuda, "Micro-fracture behaviour induced by MA constituent (island martensite) in simulated welding heat affected zone of ht80 high strength low alloyed steel," *Acta Metallurgica*, vol. 32, no. 10, pp. 1779–1788, 1984.
- [54] R. M. Ale, J. M. A. Rebello, and J. Charlier, "A metallographic technique for detecting martensite-austenite constituents in the weld heat-affected zone of a micro-alloyed steel," *Materials characterization*, vol. 37, no. 2, pp. 89–93, 1996.
- [55] H. Ikawa, H. Oshige, and T. Tanoue, "Effect of martensite-austenite constituent on HAZ toughness of a high strength steel," *Transactions of the Japan Welding Society*, vol. 11, no. 2, pp. 87–96, 1980.
- [56] P. Mohseni, "Brittle and ductile fracture of X80 arctic steel," Ph.D. dissertation, Norwegian University of Science and Technology, 2012.

- [57] C. L. Davis and J. E. King, "Effect of cooling rate on intercritically reheated microstructure and toughness in high strength low alloy steel," *Materials Science and Technology*, vol. 9, no. 1, pp. 8–15, 1993.
- [58] O. M. Akselsen, Ø. Grong, and P. E. Kvaale, "A comparative study of the heat affected zone (HAZ) properties of boron containing low carbon steels," *Metallurgical Transactions A*, vol. 17, no. 9, pp. 1529–1536, 1986.
- [59] R. M. Denys, "Wide-plate testing of weldments: Part iii heat-affected zone wide-plate studies," *Fatigue and Fracture Testing of Weldments, ASTM STP*, vol. 1058, pp. 204–228, 1990.
- [60] R. O. Ritchie, B. Francis, and W. L. Server, "Evaluation of toughness in AISI 4340 alloy steel austenitized at low and high temperatures," *Metallurgical Transactions A*, vol. 7, no. 6, pp. 831–838, 1976.
- [61] "Test method for measurement of fracture toughness," *ASTM Standard E1820 – 11*, March 2013.
- [62] L. Inc., "Handbook for damage tolerant design: Section 4.2.2. fracture toughness - abrupt fracture," "http://www.afgrow.net/applications/DTDHandbook/sections/page4_2_2.aspx", 2009-2011, accessed: 18.02.14.
- [63] S. T. Rolfe and S. R. Novac, "Slow-bend KIC testing of medium-strength high-toughness steels," in *Review of Developments in Plane Strain Fracture Toughness Testing*, ser. ASTM STP 463, W. Brown and ASTM., Eds. American Society for Testing and Materials, 1970, pp. 124–159.
- [64] L. C. A. Folch and F. M. Burdekin, "Application of coupled brittle–ductile model to study correlation between Charpy energy and fracture toughness values," *Engineering Fracture Mechanics*, vol. 63, no. 1, pp. 57–80, 5 1999.
- [65] P. Nevasmaa and K. Wallin, "SINTAP VTT/4: Task 3 status review report: Reliability based methods," VTT, TWI, British Steel, SAQ, JRC, NE, Espoo, Finland, Tech. Rep., March 1997.
- [66] B. S. Institution, "Guidance on methods for assessing the acceptability of flaws in metallic structures," *British Standards*, 2005.
- [67] G. Mathers, "CTOD testing," "<http://www.twi-global.com/technical-knowledge/job-knowledge/ctod-testing-076/>", accessed: 18.02.14.
- [68] TWI, "What is Charpy testing?" *TWI Technical Knowledge – Material FAQs*, 2013, accessed: 06.09.13. [Online]. Available: "<http://www.twi.co.uk/technical-knowledge/faqs/material-faqs/faq-what-is-charpy-testing/>"
- [69] TWI, "Mechanical testing – notched bar or impact testing," *TWI Technical Knowledge – Material FAQs*, 2013, accessed: 11.04.14. [Online]. Available: "<http://www.twi-global.com/technical-knowledge/job-knowledge/mechanical-testing-notched-bar-or-impact-testing-071/>"

- [70] R. Phaal, K. A. Macdonald, P. A. Brown, and T. W. I. TWI, *Critical Examination of Correlations Between Fracture Toughness and Charpy Impact Energy: Final Report*. TWI, 1992.
- [71] M. J. Manahan, C. N. McCowan, and M. P. S. Manahan, “Percent shear area determination in Charpy impact testing,” *Journal of ASTM International*, vol. 5, no. 7, 2008.
- [72] H.-J. Schindler and P. Tipping, “Instrumented impact testing of pre-ctacked Charpy-type specimens to obtain fracture toughness data for use in master curve methodology.”
- [73] ISO, “Steel – Charpy V-,” *EN ISO 14556:2000*.
- [74] T. Vadholm, “Comparison between Charpy-V and fracture toughness in structural steels,” NTNU - The Norwegian University of Science and Technology, Project Thesis, 2013.
- [75] R. Rintamaa, “Single specimen fracture toughness determination procedure using instrumented impact test,” Ph.D. dissertation, 1993.
- [76] “Standard test method for instrumented impact testing of metallic materials,” *ASTM Standard E2290 –13*, April 2013.
- [77] B. A. Fields, S. R. Low, and J. G. Early, “The effect of fatigue pre-cracking versus V-notching on impact testing of Charpy specimens,” in *Charpy Impact Test: Factors and Variables*, ser. ASTM STP 1072, J. Holt, A. S. for Testing, and Materials., Eds. ASTM, 1990, no. 1072, pp. 120–133.
- [78] S. Mikalac, M. G. Vassiliaros, and H. C. Rogers, “Pre-cracking and strain rate effects on hsla-100 steel Charpy specimens,” in *Charpy Impact Test: Factors and Variables*, ser. ASTM STP 1072, J. Holt, A. S. for Testing, and Materials., Eds. ASTM, 1990, no. nr. 1072, pp. 134–140.
- [79] TWI, “What is crack arrest?” *TWI Technical Knowledge – Material FAQs*, 2013, accessed: 01.12.13. [Online]. Available: <http://www.twi.co.uk/technical-knowledge/faqs/structural-integrity-faqs/faq-what-is-crack-arrest/>
- [80] K. Wallin, “Guidelines for deriving fracture toughness estimates from normal and miniature size Charpy-V specimen data,” *Rakenteiden Mekaniikka*, vol. 25, no. 3, pp. 24–40, 1992.
- [81] M. T. Kirk, K. C. Koppenhoefer, and C. Shih, “Effect of constraint on specimen dimensions needed to obtain structurally relevant toughness measures,” in *Constraint Effects in Fracture*, ser. ASTM STP 1171, K. S. E.M. Hackett and R. Dodds, Eds. Philadelphia, USA: ASTM, 1993, pp. 79–103.
- [82] C. L. Walters and G. D. Van der Weijde, “Development and validation of a low-cost CTOD procedure,” *Proceedings of the twenty-third (2013) International Offshore and Polar Engineering*, pp. 234–241, 2013.
- [83] D. Clausing, “Effect of plastic strain state on ductility and toughness,” *International Journal of Fracture Mechanics*, vol. 6, no. 1, pp. 71–85, 1970.

- [84] C. L. Walters and K. Wallin, "The use of surface appearance in combination with Charpy impact energy to determine J-integral values," in *ASME 2013 32nd International Conference on Ocean, Offshore and Arctic Engineering*, vol. 3: Materials Technology; Ocean Space Utilization. Nantes, France: ASME, 2013.
- [85] S. Mikalac, M. G. Vassiliaros, and H. C. Rogers, "Böhme, w." in *From Charpy To Present Impact Testing*, ser. European Structural Integrity Society, A. P. D. François and A. Pineau, Eds. Elsevier, 2002, vol. 30, pp. 189–196.
- [86] A. Bannister, "Structural integrity assessment procedures for european industry (SINTAP) sub-task 3.3 report: Determination of fracture toughness from Charpy impact energy: Procedure and validation," *Document No. SINTAP/BS/15. British Steel plc*, 1997.
- [87] J. Barsom and S. Rolfe, "Correlations between and Charpy V-notch test results in the transition-temperature range," in *Impact Testing of Metals*, ser. ASTM STP 466. Philadelphia, USA: ASTM, 1970, pp. 281–302.
- [88] S. Webster and A. Bannister, "Structural integrity assessment procedure for europe—of the SINTAP programme overview," *Engineering Fracture Mechanics*, vol. 67, no. 6, pp. 481–514, 2000.
- [89] B. Marandet and G. Sanz, "Evaluation of the toughness of thick medium-strength steels by using linear-elastic fracture mechanics and correlations between KIC and Charpy V-notch," in *Flaw Growth and Fracture: 10th Conference*, ser. ASTM STP 631, J. Barsom, Ed. ASTM, 1977, pp. 72–95.
- [90] "Standard test method for determination of reference temperature, T_0 , for ferritic steels in the transition range," *ASTM Standard E1921 – 13a*, November 2013.
- [91] T. Planman, W. Server, K. Wallin, and S. Rosinski, "Application of the Master Curve approach for abnormal material conditions," in *ASME 2007 Pressure Vessels and Piping Conference*. American Society of Mechanical Engineers, 2007, pp. 235–242.
- [92] T. Planman, W. Server, K. Wallin, and S. Rosinski, "Application of the Master Curve approach for abnormal material conditions," in *ASME 2007 Pressure Vessels and Piping Conference*. American Society of Mechanical Engineers, 2007, pp. 235–242.
- [93] H. O. Nordhagen, "Project meeting – Instrumented Charpy tests of 420 steel," Power Point presentation from Arctic Material Project Meting, 2014.
- [94] H. O. Nordhagen, "Modelling of fracture in steel pipeline materials," Power Point presentation from Arctic Material Project Meting, 2010.
- [95] B. S. Institution, "Fracture mechanics toughness tests — Part 1: Method for determination of K_{Ic}, critical CTOD and critical J values of metallic materials," *British Standards*, 1991.
- [96] B. R. S. Rogne, C. Thaulow, and A. Barnoush, "Micromechanical testing of fracture initiation sites in welded high-strength low-alloy steel," *Metallurgical and Materials Transactions A*, pp. 1–8, 2014.

BIBLIOGRAPHY

- [97] E. Østby, "Communication and discussion on the topics discussed in the present master's thesis," Private communication, 2014.

Appendices

A Data From Instrumented Charpy Testing

Parameters presented

a_0	Initial notch or pre-crack length
C_V	Measured absorbed energy during Charpy-test. Value given by test instrument.
$C_{V,c}$	Calculated total absorbed Charpy energy, obtained from load-time history recorded
$\frac{C_{V,f}}{C_{V,c}}$	Calculated absorbed Charpy energy up to load at brittle fracture initiation, obtained from load-time history recorded
$C_{V,m}$	Calculated absorbed Charpy energy up to maximum load, F_m , obtained from load-time history recorded
$\frac{C_{V,m}}{C_{V,c}}$	Calculated absorbed Charpy energy up to maximum load, obtained from load-time history recorded
F_m	Maximum load
s_m	Bending displacement at maximum load, F_m

The specimens are labelled according to the following system:

bmxxc	for	base material, V-notched
bmxxf	for	base material, pre-cracked
ssxxc	for	CGHAZ, V-notched
ssxxf	for	CGHAZ, pre-cracked
ss2.xxc	for	ICCGHAZ, V-notched
ss2.xxf	for	ICCGHAZ, pre-cracked

A.1 All Data From Charpy Testing of V-notched Base Material

Table A.3: Table of test data from instrumented Charpy testing of ICCGHAZ, base material series.

No.	T [°C]	a ₀ [mm]	F _m [kN]	C _{V,m} [J]	C _{V,f} [J]	s _m [mm]	C _V [J]	C _{V,c} [J]	Note	Class	$\frac{C_{V,m}}{C_{V,c}}$	$\frac{C_{V,m}}{C_{V,c}}$
bm2c	-30	1.98	21.2	80.0	-	4.15	264.7	241.2		I	0.33	-
bm3c	-30	1.98	21.2	78.4	-	4.07	263.7	282.4		I	0.28	-
bm4c	-30	1.98	21.5	81.2	-	4.16	263.7	293.8		I	0.28	-
bm5c	-60	1.98	22.2	80.8	-	3.97	258.5	281.4		I	0.29	-
bm6c	-60	1.98	22.2	78.5	-	3.86	263.5	287.0		I	0.27	-
bm7c	-60	1.98	22.4	72.0	-	3.56	253.0	276.6		I	0.26	-
bm8c	-90	1.98	22.9	76.0	-	3.66	248.2	270.8		I	0.28	-
bm9c	-90	1.98	22.6	76.0	-	3.71	245.2	268.7		I	0.28	-
bm10c	-90	1.98	23.1	76.7	-	3.66	266.8	290.1		I	0.26	-
bm11c	-120	1.98	21.5	-	-	-	212.7	-	Invalid	-	-	-
bm12c	-120	1.98	24.1	73.0	-	3.25	183.3	201.3		I	0.36	-
bm13c	-120	1.98	23.8	70.1	-	3.14	233.8	259.1		I	0.27	-
bm18c	-137	1.98	23.0	11.7	11.7	0.78	13.9	14.3	Teflon	IV	0.82	0.82
bm19c	-137	1.98	23.1	19.9	19.9	1.15	20.6	22.6	Teflon	IV	0.88	0.88
bm20c	-137	1.98	22.7	14.2	14.2	0.76	14.6	16.0	Teflon	IV	0.89	0.89
bm14c	-155	1.98	21.5	-	-	-	6.4	-	Invalid	-	-	-
bm15c	-155	1.98	23.7	15.8	15.8	0.77	16.5	16.9	SEM	IV	0.94	0.94
bm16c	-155	2.00	-	6.7	7.6	-	-	-	Invalid	-	-	-
bm17c	-155	1.98	21.2	7.6	-	0.42	10.3	9.1		IV	0.84	0.84

Table A.4: Table of average measured energy values and standard and relative standard deviation obtained from instrumented Charpy testing of base material, V-notched series.

T [°C]	C _{V,average} [J]	SD	RSD [%]
-30	264.0	0.5	0.2
-60	258.3	4.3	1.7
-90	253.4	9.6	3.8
-120	209.9	20.7	9.9
-137	16.4	3.0	18.4
-155	10.0	4.14	0.8

A.2 All Data From Charpy Testing of pre-cracked Base Material

Table A.5: Table of test data from instrumented Charpy testing of base material, pre-cracked series.

No.	T [°C]	a ₀ [mm]	F _m [kN]	C _{V,m} [J]	C _{V,f} [J]	s _m [mm]	C _V [J]	C _{V,c} [J]	Note	Class	$\frac{C_{V,m}}{C_{V,c}}$	$\frac{C_{V,f}}{C_{V,c}}$
bm26f	-30	1.76	22.3	79.4	-	3.92	274.0	295.9		I	0.27	-
bm27f	-30	1.76	22.1	79.7	-	3.96	294.1	311.2		I	0.26	-
bm28f	-30	1.77	22.2	80.5	-	3.96	285.5	304.2		I	0.27	-
bm29f	-60	2.12	1.3	68.5	-	3.49	235.4	258.2		I	0.27	-
bm30f	-60	2.01	21.6	68.8	-	3.47	240.0	262.2		I	0.26	-
bm31f	-60	2.03	21.5	71.0	-	3.62	253.2	275.4		I	0.26	-
bm35f	-75	1.91	22.2	74.0	-	3.62	259.6	281.2		I	0.26	-
bm36f	-75	2.06	21.7	69.8	205.8	3.52	210.6	230.8		II	0.30	0.89
bm37f	-75	2.1	21.6	69.0	-	3.48	247.7	271.2		I	0.25	-
bm38f	-82	2.07	21.9	70.0	42.1	3.50	163.3	180.2	Class?	I*	0.39	-
bm39f	-82	2.04	13.0	6.0	6.9	0.44	31.9	26.6		V	0.23	0.27
bm40f	-82	2.04	8.3	2.1	2.1	0.24	31.4	31.5		V	0.07	0.07
bm44f	-82	2.04	21.5	-	-	-	26.8	-	Invalid	-	-	-
bm45f	-82	2.02	11.5	2.7	2.7	0.23	18.5	13.0	Teflon	V	0.21	0.21
bm46f	-82	2.01	22.3	69.7	-	3.42	230.7	252.5	Teflon	I	0.28	-
bm32f	-90	1.84	9.0	3.6	3.6	0.32	23.7	20.6	SEM	V	0.18	0.18
bm33f	-90	1.87	8.2	2.3	2.3	0.21	20.9	18.6		V	0.12	0.12
bm34f	-90	1.83	9.1	2.3	2.3	0.23	31.7	30.7		V	0.08	0.8
bm41f	-120	2.05	21.5	-	-	-	3.6	-	Invalid	-	-	-
bm42f	-120	1.91	11.6	1.4	1.4	0.11	5.7	2.7	SEM	IV	0.52	0.52
bm43f	-120	2.06	8.0	1.8	1.8	0.13	2.9	1.9		IV	0.95	0.95

Table A.6: Table of average measured energy values and standard and relative standard deviation obtained from instrumented Charpy testing of base material, pre-cracked series.

T [°C]	C _{V,average} [J]	SD	RSD [%]
-30	284.5	8.2	2.9
-60	242.9	7.5	3.1
-75	239.3	20.9	8.7
-82	83.8	82.5	98.5
-90	25.4	4.6	18.0
-120	4.1	1.2	29.3

A.3 All Data From Charpy Testing of V-notched CGHAZ

Table A.7: Table of test data from instrumented Charpy testing of CGHAZ, V-notched series.

No.	T [°C]	a ₀ [mm]	F _m [kN]	C _{V,m} [J]	C _{V,f} [J]	s _m [mm]	C _V [J]	C _{V,c} [J]	Note	Class	$\frac{C_{V,m}}{C_{V,c}}$	$\frac{C_{V,f}}{C_{V,c}}$
ss13c	23	1.98	20.0	62.2	181.4	3.55	208.1	199.4		II	0.31	0.91
ss14c	23	1.98	22.9	71.0	205.1	3.46	212.7	230.1		II	0.31	0.89
ss15c	23	1.98	22.8	74.5	197.2	3.55	216.8	234.3		II	0.32	0.84
ss10c	0	1.98	23.5	70.0	-	3.34	236.9	257.5		I	0.27	-
ss11c	0	1.98	23.4	75.0	175.8	3.55	185.9	199.7		III	0.38	0.88
ss12c	0	1.98	23.3	67.5	203.4	3.29	205.5	221.1		II	0.31	0.92
ss16c	-15	1.98	23.5	67.5	98.2	3.22	97.3	105.5		III	0.64	0.93
ss17c	-15	1.98	23.6	72.5	151.6	3.42	149.4	163.0		III	0.45	0.93
ss18c	-15	1.98	23.8	73.5	163.7	3.45	159.1	174.0		III	0.50	0.4
ss4c	-30	1.98	24.3	76.5	147.7	3.79	140.6	154.5	SEM	III	0.50	0.96
ss5c	-30	1.98	21.5	25.7	25.7	1.45	28.6	27.5		IV	0.94	0.94
ss6c	-30	1.98	24.1	74.4	74.4	3.45	87.6	95.7		IV	0.78	0.78
ss19c	-45	1.98	24.6	73.2	73.2	3.34	65.4	73.9		IV	0.99	0.99
ss20c	-45	1.98	24.6	74.4	74.4	3.37	82.4	93.2		IV	0.80	0.80
ss21c	-45	1.98	24.6	57.3	57.3	2.65	52.5	59.3		IV	0.85	0.97
ss7c	-60	1.98	15.5	4.9	4.9	0.34	5.2	5.3	SEM	IV	0.93	0.93
ss8c	-60	1.98	17.7	7.8	7.8	0.50	8.8	8.6		IV	0.91	0.91
ss9c	-60	1.98	19.5	9.6	9.6	0.59	11.6	11.2		IV	0.86	0.86

Table A.8: Table of average measured energy values and standard and relative standard deviation obtained from instrumented Charpy testing of CGHAZ, V-notched series.

T [°C]	C _{V,average} [J]	SD	RSD [%]
23	212.5	3.6	1.7
0	209.4	21.0	10.0
-15	135.3	27.1	20.1
-30	85.6	45.7	53.4
-45	66.8	12.2	18.3
-60	8.5	2.6	30.7

A.4 All Data From Charpy Testing of pre-cracked CGHAZ

Table A.9: Table of test data from instrumented Charpy testing of CGHAZ, pre-cracked series.

No.	T [°C]	a ₀ [mm]	F _m [kN]	C _{V,m} [J]	C _{V,f} [J]	s _m [mm]	C _V [J]	C _{V,c} [J]	Note	Class	$\frac{C_{V,m}}{C_{V,c}}$	$\frac{C_{V,f}}{C_{V,c}}$
ss63f	23	2.02	21.8	62.3	-	3.15	217.3	236.2		I	0.26	-
ss64f	23	1.88	23.0	69.3	-	3.35	233.8	253.9		I	0.27	-
ss65f	23	2.03	22.0	66.0	-	3.30	230.2	250.1		I	0.26	-
ss66f	11	1.87	23.4	70.6	198.9	3.35	206.5	225.6		II	0.31	0.88
ss67f	11	1.87	23.2	76.0	76.0	3.60	89.6	95.4		IV	0.80	0.80
ss68f	11	2.00	22.4	78.6	78.6	3.81	88.6	93.9		IV	0.84	0.84
ss30f	0	1.88	19.3	17.4	17.4	1.03	33.3	36.6	SEM	V	0.57	0.57
ss61f	0	2.02	14.6	4.2	4.2	0.32	39.1	38.0		V	0.11	0.11
ss62f	0	2.04	17.6	7.9	7.9	0.53	27.3	24.5		V	0.32	0.32
ss27f	-30	1.98	9.5	2.2	2.2	0.20	13.4	14.3	SEM	V	0.15	0.15
ss28f	-30	1.93	10.0	2.4	2.4	0.18	12.4	9.0		V	0.27	0.27
ss29f	-30	1.95	13.5	4.4	4.4	0.33	12.9	9.6		IV	0.46	0.46
ss69f	-60	1.88	9.0	3.1	3.1	0.28	7.4	5.1	Led	V	0.61	0.61
ss70f	-60	1.87	8.0	1.8	1.8	0.18	5.7	3.9		V	0.46	0.46
ss71f	-60	2.05	6.8	1.6	1.6	0.17	6.2	5.0		V	0.32	0.32
ss72f	-60	2.03	21.5	-	-	-	5.6	-	Invalid	-	-	-

Table A.10: Table of average measured energy values and standard and relative standard deviation obtained from instrumented Charpy testing of CGHAZ, pre-cracked series.

T [°C]	C _{V,average} [J]	SD	RSD [%]
23	227.1	7.1	3.1
11	128.2	55.3	43.2
0	3.1	4.8	14.5
-30	12.9	0.4	3.2
-60	6.2	0.7	11.5

A.5 All Data From Charpy Testing of V-notched ICCGHAZ

Table A.11: Table of test data from instrumented Charpy testing of ICCGHAZ, V-notched series.

No.	T [°C]	a_0 [mm]	F_m [kN]	$C_{V,m}$ [J]	$C_{V,f}$ [J]	s_m [mm]	C_V [J]	$C_{V,c}$ [J]	Note	Class	$\frac{C_{V,m}}{C_{V,c}}$	$\frac{C_{V,f}}{C_{V,c}}$
ss2.93c	23	1.98	21.5	84.5	174.4	4.45	2.2	224.3		II	0.38	0.78
ss2.95c	23	1.98	21.4	82.5	177.9	4.35	203.9	223.3		II	0.37	0.80
ss2.96c	23	1.98	21.3	83.5	201.2	4.45	214.3	232		II	0.36	0.87
ss2.97c	0	1.98	22.0	85.5	158.1	4.4	24.1	186.1		III	0.46	0.85
ss2.100c	0	1.98	22.0	77.0	77.0	4.0	95.0	101.8		IV	0.76	0.76
ss2.102c	0	1.98	22.0	85.0	157.2	4.35	166.9	183.3		III	0.46	0.86
ss2.103c	-30	1.98	21.9	51.0	51.0	2.7 5	5.1	56.4		IV	0.90	0.90
ss2.104c	-30	1.98	20.0	27.6	27.6	1.6 3	5.5	34.6	SEM	IV	0.80	0.80
ss2.106c	-60	1.98	17.3	6.5	6.5	0.5 1	0.8 1	8.7	SEM	IV	0.75	0.75
ss2.107c	-60	1.98	17.4	6.5	6.5	0.51	10.8	9.6		IV	0.68	0.68
ss2.108c	-60	1.98	18.8	12.3	12.3	0.83	14.9	13.8		IV	0.89	0.89

Table A.12: Table of average measured energy values and standard and relative standard deviation obtained from instrumented Charpy testing of ICCGHAZ, V-notched series.

T [°C]	$C_{V,average}$ [J]	SD	RSD [%]
23	205.0	207.7	4.7
0	170.0	144.0	34.6
-30	45.3	9.8	21.6
-60	2.2	1.9	15.9

A.6 All Data From Charpy Testing of pre-cracked ICCGHAZ

Table A.13: Table of test data from instrumented Charpy testing of ICCGHAZ, pre-cracked series.

No.	T [°C]	a ₀ [mm]	F _m [kN]	C _{V,m} [J]	C _{V,f} [J]	s _m [mm]	C _V [J]	C _{V,c} [J]	Note	Class	$\frac{C_{V,m}}{C_{V,c}}$	$\frac{C_{V,f}}{C_{V,c}}$
s2.76f	23	2	16.4	19.7	19.7	1.36	n/a	73.1		V	0.27	0.27
ss2.77f	23	2	16.3	13.7	13.7	1.00	78.8	86.7		V	0.16	0.16
ss2.78f	23	2	18.0	27.4	27.4	1.76	73.3	78.8		V	0.35	0.35
ss2.79f	0	2	21.5	5.1	5.1	0.40	43.1	41.7	SEM	V	0.12	0.12
ss2.80f	0	2	17.1	9.8	9.8	0.66	46.6	47.7		V	0.21	0.21
ss2.81f	0	2	18.6	18.2	18.2	1.11	47.6	48.7		V	0.37	0.37
ss2.82f	-30	2	16.0	6.0	6.0	0.52	20.1	18.2	SEM	V	0.33	0.33
ss2.83f	-30	2	17.5	5.3	5.3	0.44	21.6	19.9		V	0.27	0.27
ss.2.85f	-60	2	12.0	2.0	2.0	0.24	7.8	5.5		V	0.36	0.36
ss2.86f	-60	2	11.3	1.6	1.6	0.20	12.1	10.1		V	0.16	0.16
ss2.87f	-60	2	11.1	1.7	1.7	0.31	7.7	6.1	SEM	V	0.28	0.28

Table A.14: Table of average measured energy values and standard and relative standard deviation obtained from instrumented Charpy testing of ICCGHAZ, pre-cracked series.

T [°C]	C _{V,average} [J]	SD	RSD [%]
23	76.1	2.8	3.6
0	45.8	1.9	4.2
-30	20.9	2.8	3.6
-60	9.2	2.1 2	2.3

B Data From CTOD Testing

Data from quasi-static CTOD tests performed for specimens with weld-simulated CGHAZ and ICCGHAZ microstructures are included in this appendix.

B.1 CTOD Testing of CGHAZ

Table B.1: Table of data obtained during instrumented CTOD testing of CGHAZ. The two bottom rows includes the average values and the standard deviation (SD) and relative standard deviation (RSD) at each test temperature

No.	T [°C]	CTOD [mm]	J	No.	T [°C]	CTOD [mm]	J	No.	T [°C]	CTOD [mm]	J	No.	T [°C]	CTOD [mm]	J []
444	-90	0.081	70.5	299	-60	0.114	105.0	310	-30	0.251	246.5	434	0	0.988	750.9
445	-90	0.018	15.1	300	-60	0.276	258.4	311	-30	0.044	20.0	435	0	0.992	755.8
446	-90	0.126	114.3	301	-60	0.057	47.8	312	-30	0.589	324.2	436	0	0.820	658.9
447	-90	0.040	32.8	302	-60	0.038	32.3	313	-30	0.093	67.2	437	0	0.280	249.7
448	-90	0.176	167.2	303	-60	0.035	31.0	314	-30	0.180	150.0	438	0	0.928	732.3
449	-90	0.042	35.2	304	-60	0.139	131.5	315	-30	0.116	85.6	439	0	0.894	721.2
450	-90	0.224	217.2	306	-60	0.052	44.1	316	-30	0.065	32.0	440	0	0.790	655.1
451	-90	0.128	116.1	307	-60	0.071	59.0	317	-30	0.053	32.8	441	0	0.684	585.9
452	-90	0.042	34.5	308	-60	0.047	42.5	318	-30	0.399	296.2	442	0	0.233	205.3
453	-90	0.040	33.2	309	-60	0.308	305.0	319	-30	0.102	71.9	443	0	0.946	747.5

Average values, Standard Deviation (SD) and Relative Standard Deviation (RSD)

T [°C]	CTOD _{Ave} [mm]	SD	RSD [%]	T [°C]	CTOD _{Ave} [mm]	SD	RSD [%]	T [°C]	CTOD _{Ave} [mm]	SD	RSD [%]	T [°C]	CTOD _{Ave} [mm]	SD	RSD [%]
-90	0.092	0.065	71.5	-60	0.114	0.095	83.5	-30	0.189	0.169	89.2	0	0.756	0.266	35.1

B.2 CTOD Testing of ICCGHAZ

Table B.2: Table of data obtained during instrumented CTOD testing of ICCGHAZ. The two bottom rows includes the average values and the standard deviation (SD) and relative standard deviation (RSD) at each test temperature.

No.	T [°C]	CTOD [mm]	J	No.	T [°C]	CTOD [mm]	J	No.	T [°C]	CTOD [mm]	J	No.	T [°C]	CTOD [mm]	J []
174	-90	0.018	15.0	184	-60	0.043	33.4	194	-30	0.159	116.1	204	0	0.144	117.2
175	-90	0.025	19.8	185	-60	0.040	29.9	195	-30	0.113	90.8	205	0	0.165	135.4
176	-90	0.019	16.4	186	-60	0.030	23.6	196	-30	0.067	52.1	206	0	0.143	113.8
177	-90	0.028	23.5	187	-60	0.048	38.4	197	-30	0.079	51.7	207	0	0.175	141.1
179	-90	0.028	22.9	188	-60	0.072	57.7	198	-30	0.079	62.0	208	0	0.165	135.6
180	-90	0.025	21.8	189	-60	0.036	28.9	199	-30	0.071	54.8	209	0	0.163	130.2
181	-90	0.015	13.4	190	-60	0.031	23.4	200	-30	0.065	50.3	210	0	0.226	186.8
182	-90	0.020	15.8	191	-60	0.042	32.5	201	-30	0.071	55.1	211	0	0.200	168.1
183	-90	0.036	28.5	192	-60	0.085	68.1	202	-30	0.140	114.0	212	0	0.151	118.2
				193	-60	0.069	56.1	203	-30	0.055	42.3	213	0	0.315	271.1

Average values, Standard Deviation (SD) and Relative Standard Deviation (RSD)

T [°C]	CTOD _{Ave} [mm]	SD	RSD [%]	T [°C]	CTOD _{Ave} [mm]	SD	RSD [%]	T [°C]	CTOD _{Ave} [mm]	SD	RSD [%]	T [°C]	CTOD _{Ave} [mm]	SD	RSD [%]
-90	0.006	0.024	25.8	-60	0.018	0.050	36.2	-30	0.033	0.090	37.2	0	0.050	0.185	27.0

C Curves From Instrumented Charpy Testing

Valid curves from instrumented Charpy tests are included in this appendix. The curves for the base material, Charpy-V notched and fatigue pre-cracked specimens (bm,c and bm,f respectively) are presented first, followed by the curves for the Charpy V-notched and fatigue pre-cracked welds simulated CGHAZ and ICCGAZ specimens.

Invalid curves have been obtained for some of the test specimens due to lack of triggering of the machine. These curves have not been included in this section. However, the measured total energy can still be used and therefore valid numbers obtained from these tests are included in the table in Appendix A.

For all curves, the black line represents the averaged load value for the given deflection, given in kN. The thinner, dotted line is the true measured values. The thick black line is considered to represent the true load value, as it is an average of the peak and bottom values measured. The blue line represents the measured energy in Jcm^{-2} . The red lines marks the maximum load value at the given deflection and the corresponding energy measured at the same deflection.

All curves include specimen number and designated class. Some of the curves are designated with “teflon”. This means that the specimen has been covered with teflon during the test, in order to prevent triggering of the instrument due to air fluctuations due to temperature differences between the sample and test machine.

As some of the measurements ended at small measured deflection and load values, it should be noted that the x and y-axis has been scaled over different intervals for some of the graphs in order to get a better impression of the curve shape for these curves. Additional comments can be found under some of the curves below.

C.1 Base material V-notched

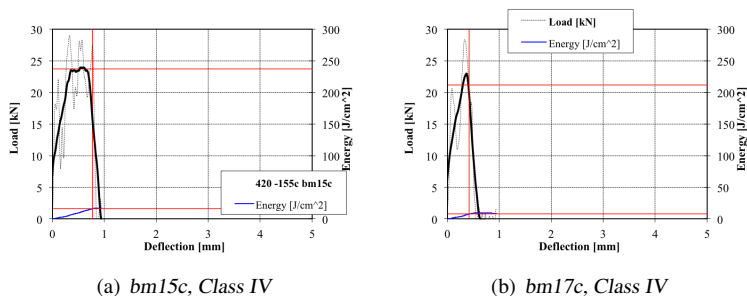


Figure C.1: Base material, V-notched specimens tested at -155°C . Two of the tests performed at this temperature, specimen *bm14c* and *bm16c*, had invalid curves.

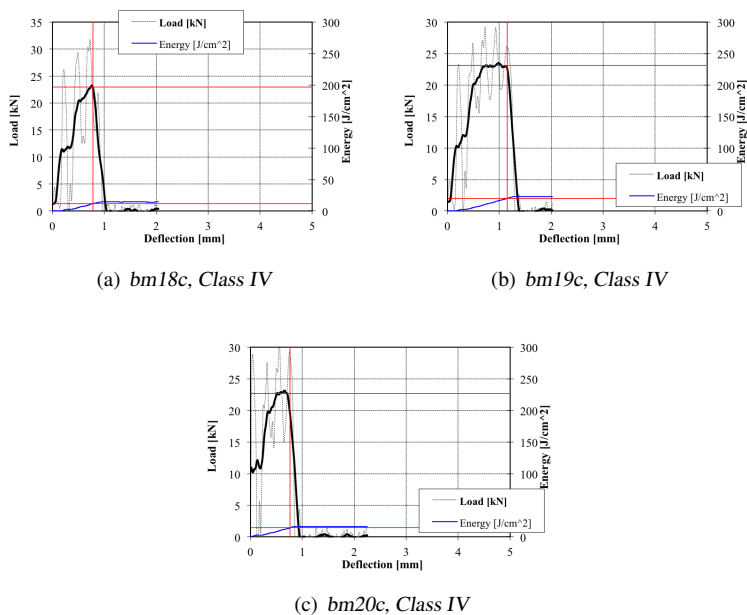


Figure C.2: Base material, V-notched specimens tested at -137°C

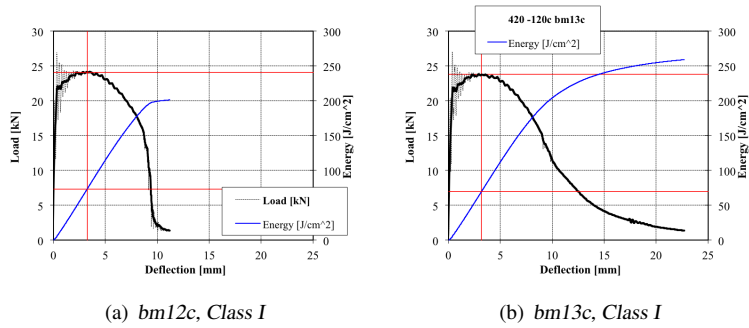


Figure C.3: Base material, V-notched specimens tested at -120°C . The third test performed at this temperature, specimen *bm11c*, had invalid curves.

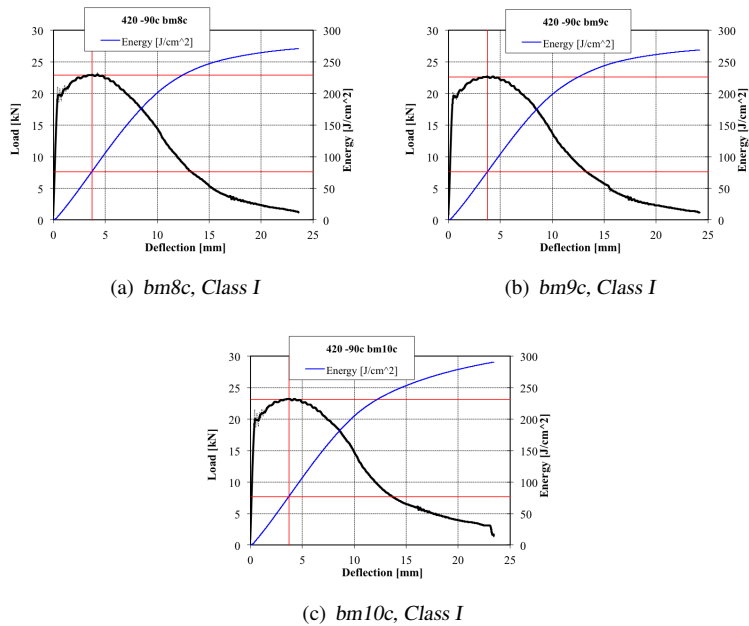


Figure C.4: Base material, V-notched specimens tested at -90°C

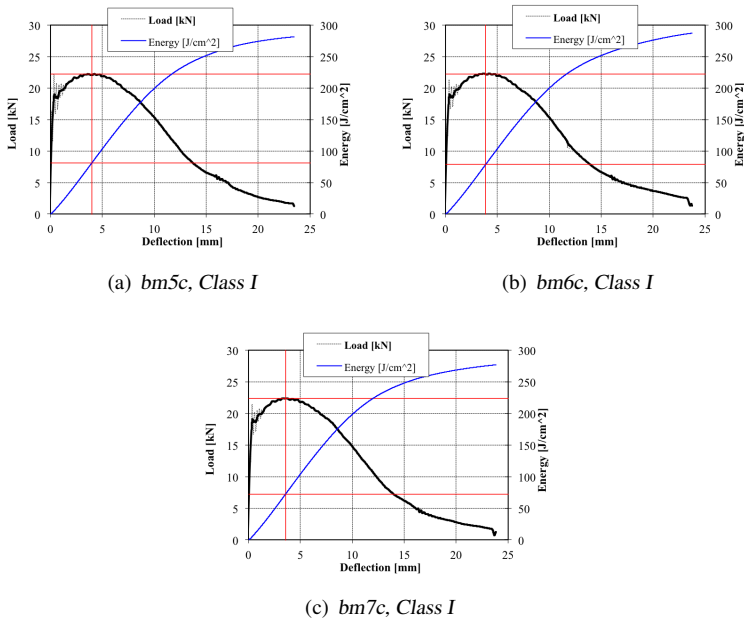


Figure C.5: Base material, V-notched specimens tested at -60°C

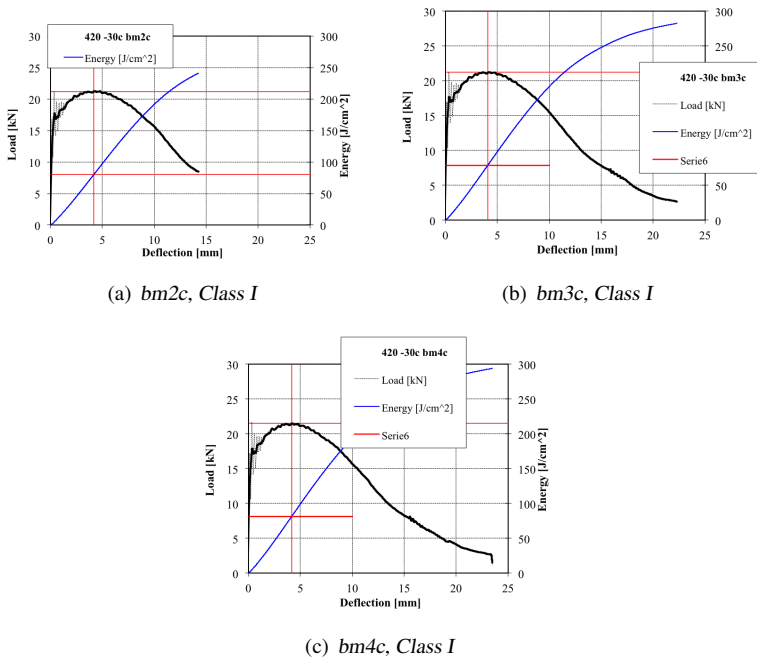


Figure C.6: Base material, V-notched specimens tested at -30°C

C.2 Base Material pre-cracked

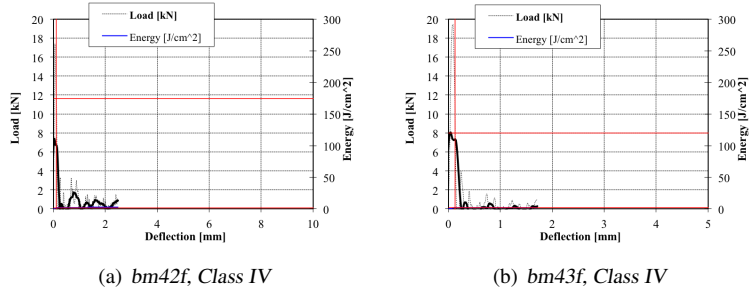


Figure C.7: Base material, pre-cracked specimens tested at -120°C . The third test performed at this temperature, specimen *bm41f*, had invalid curves.

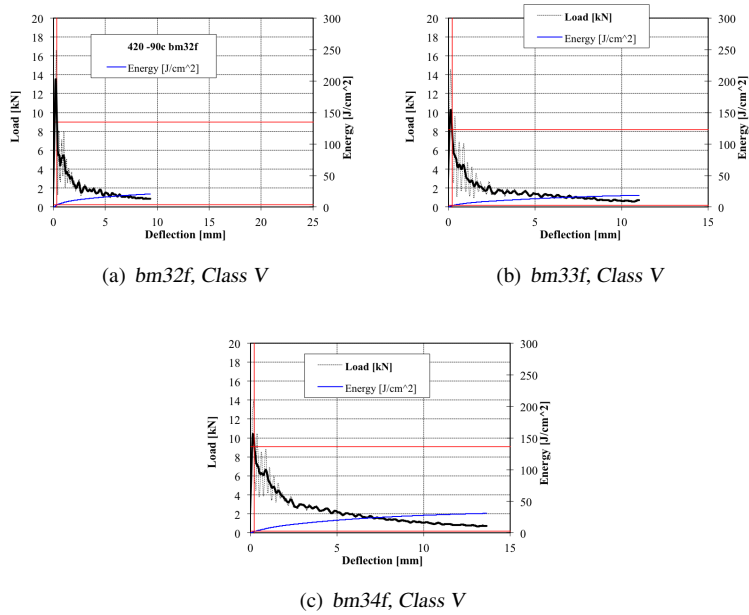
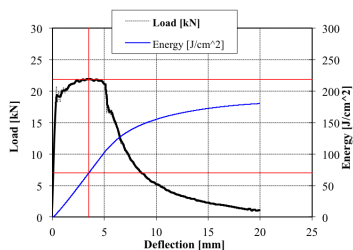
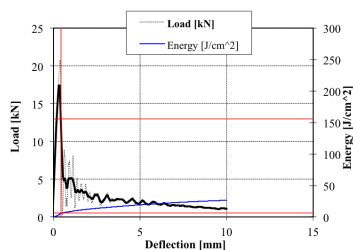


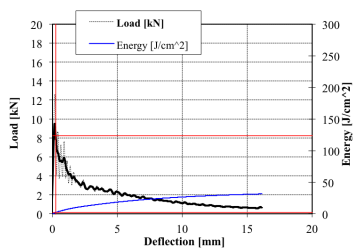
Figure C.8: Base material, pre-cracked specimens tested at -90°C



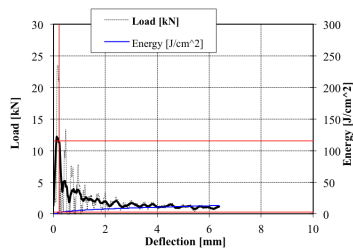
(a) *bm38f, Class I**



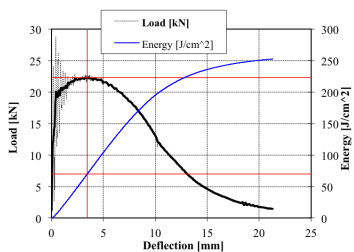
(b) *bm39f, Class V*



(c) *bm40f, Class V*



(d) *bm45f, Class V*



(e) *bm46f, Class I*

Figure C.9: Base material, pre-cracked specimens tested at -82°C . One test performed at this temperature, specimen *bm44f*, had invalid curves.

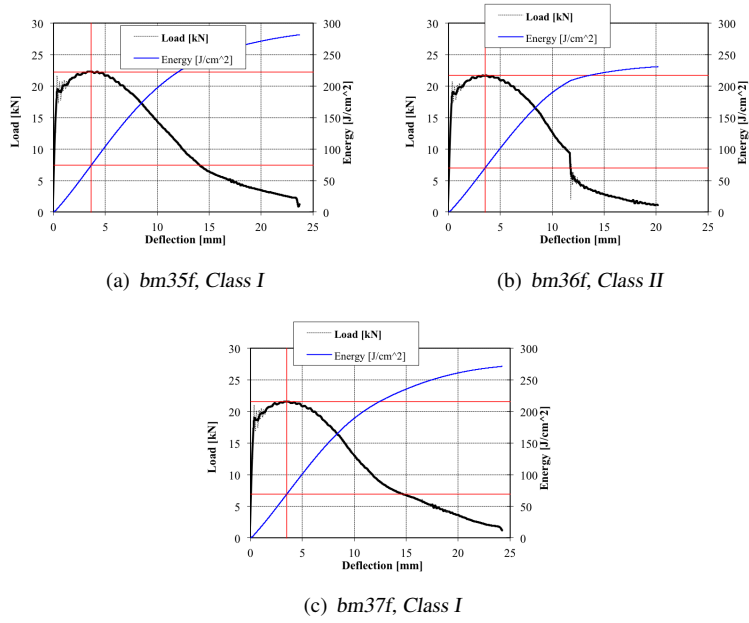


Figure C.10: Base material, pre-cracked specimens tested at -75°C

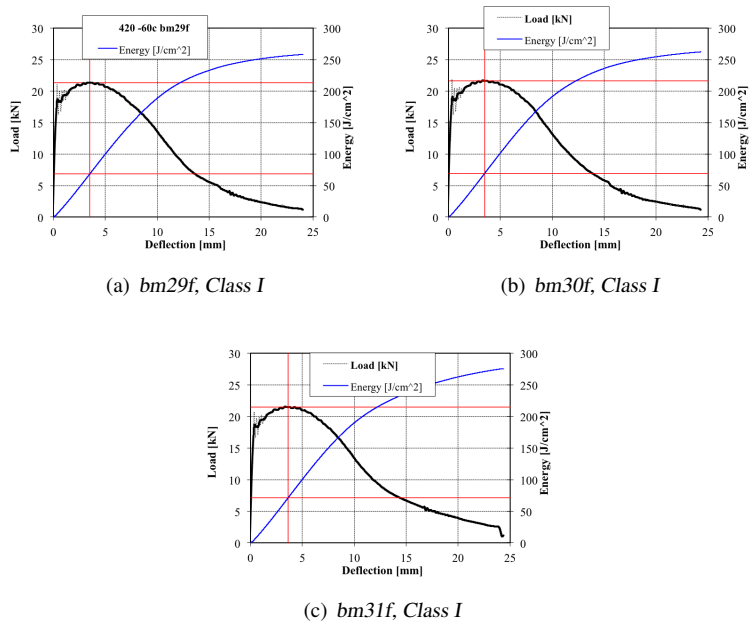
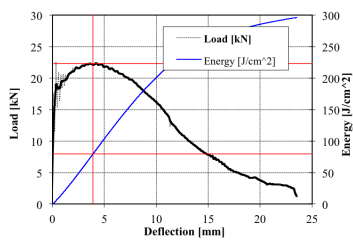
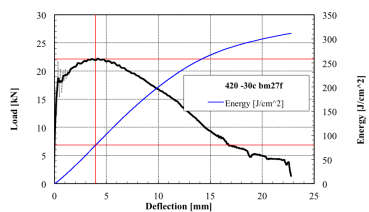


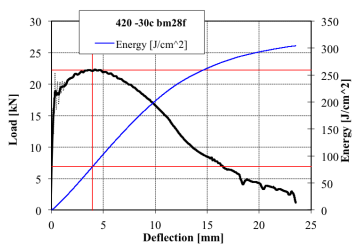
Figure C.11: Base material, pre-cracked specimens tested at -60°C



(a) *bm26f*, Class I



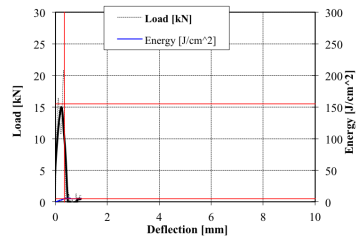
(b) *bm27f*, Class I



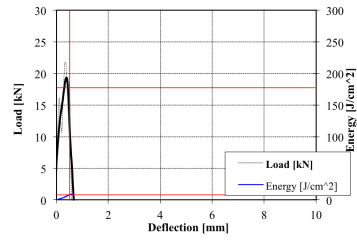
(c) *bm28f*, Class I

Figure C.12: Base material, pre-cracked specimens tested at $-30\text{ }^{\circ}\text{C}$

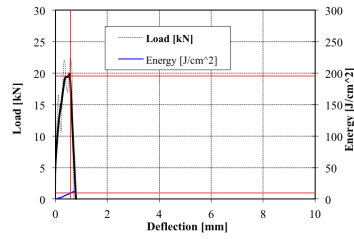
C.3 CGHAZ V-notched



(a) ss7c, Class IV



(b) ss8c, Class IV



(c) ss9c, Class IV

Figure C.13: CGHAZ, V-notched specimens tested at -60°C

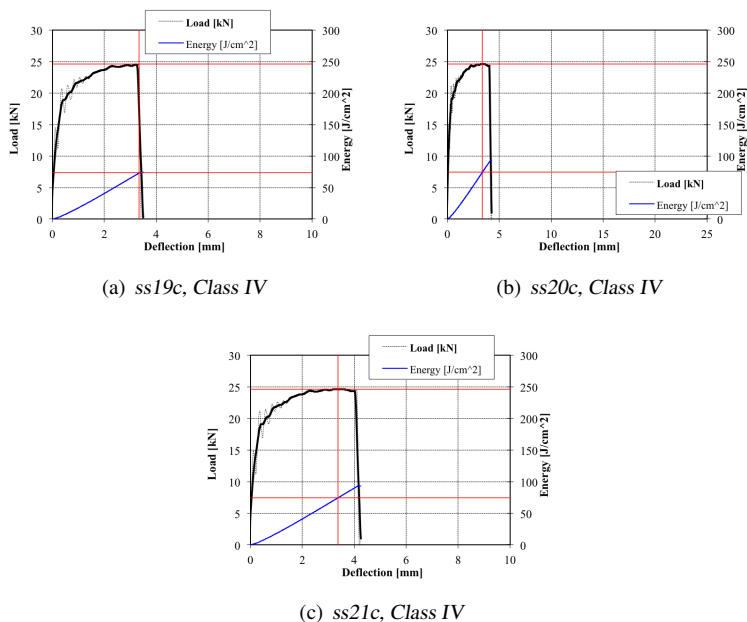


Figure C.14: CGHAZ, V-notched specimens tested at -45°C

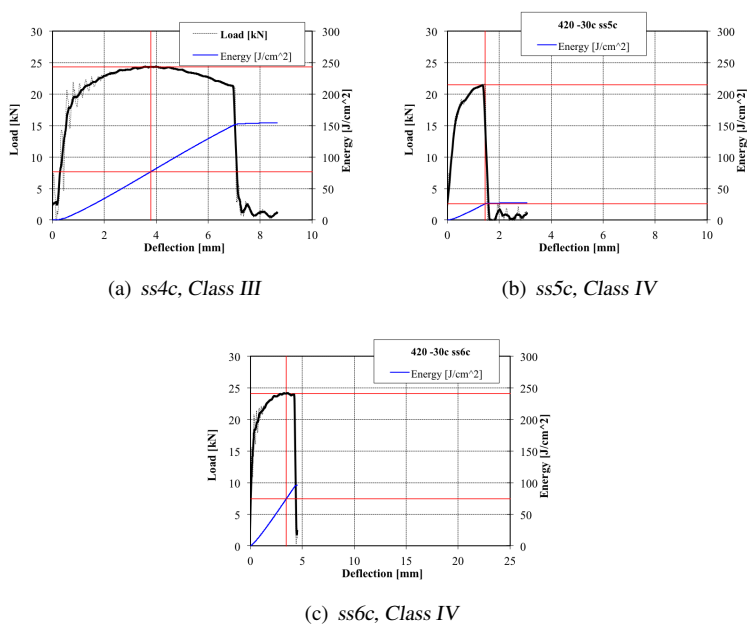


Figure C.15: CGHAZ, V-notched specimens tested at -30°C

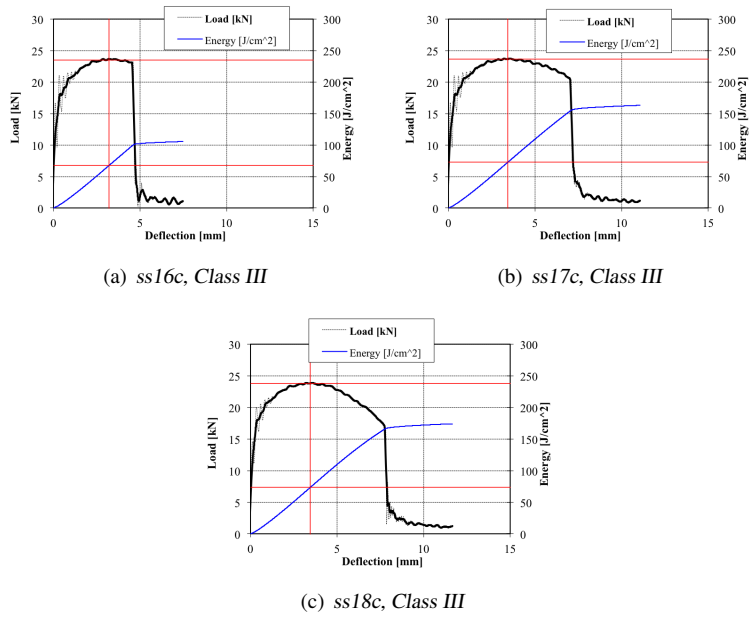


Figure C.16: CGHAZ, V-notched specimens tested at -15°C

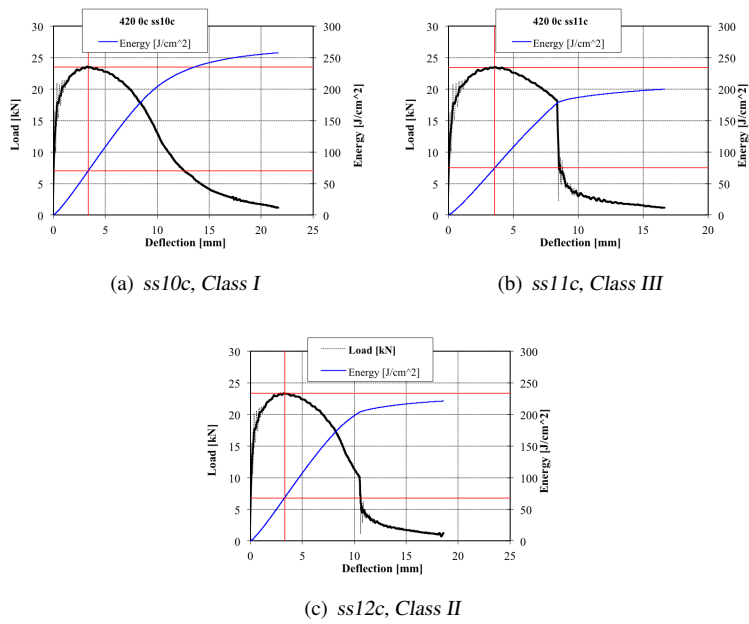
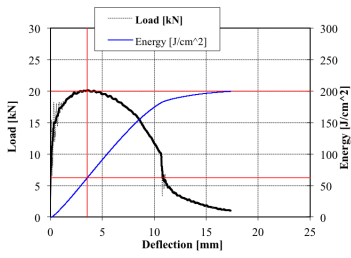
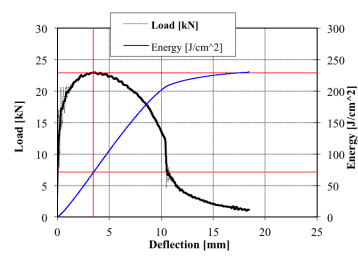


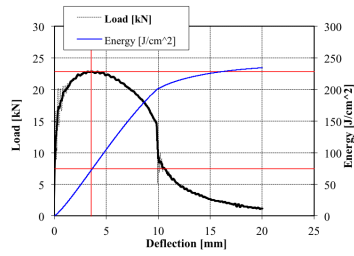
Figure C.17: CGHAZ, V-notched specimens tested at 0°C



(a) *ss13c, Class II*



(b) *ss14c, Class II*



(c) *ss15c, Class II*

Figure C.18: CGHAZ, V-notched specimens tested at 23°C

C.4 CGHAZ pre-cracked

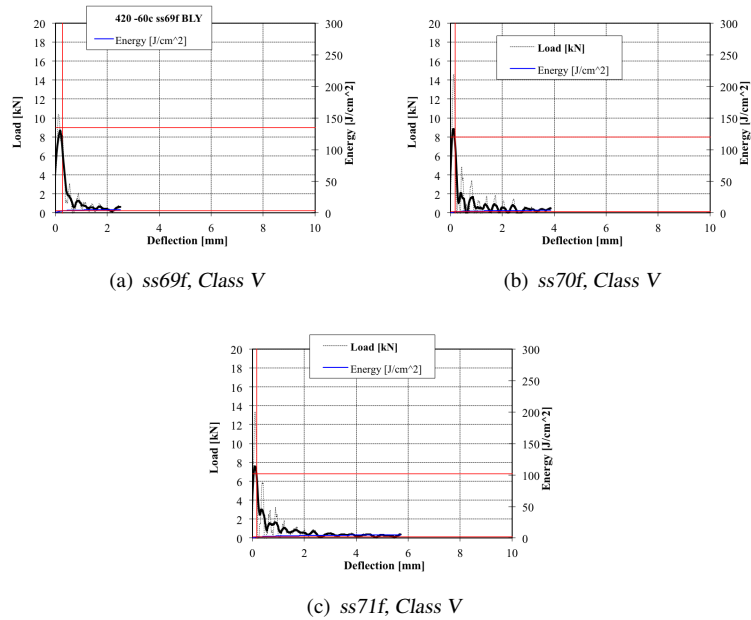


Figure C.19: CGHAZ, pre-cracked specimens tested at -60°C . One test performed at this temperature, specimen *ss72f*, had invalid curves.

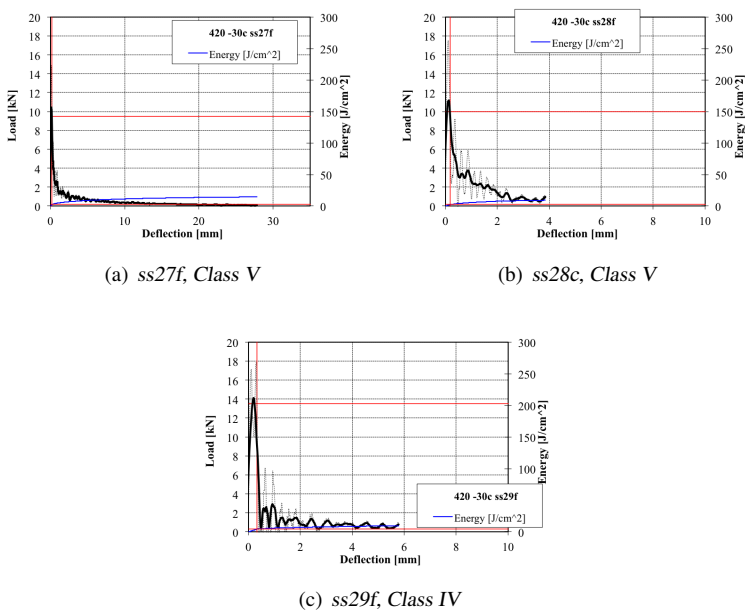


Figure C.20: CGHAZ, pre-cracked specimens tested at -30°C .

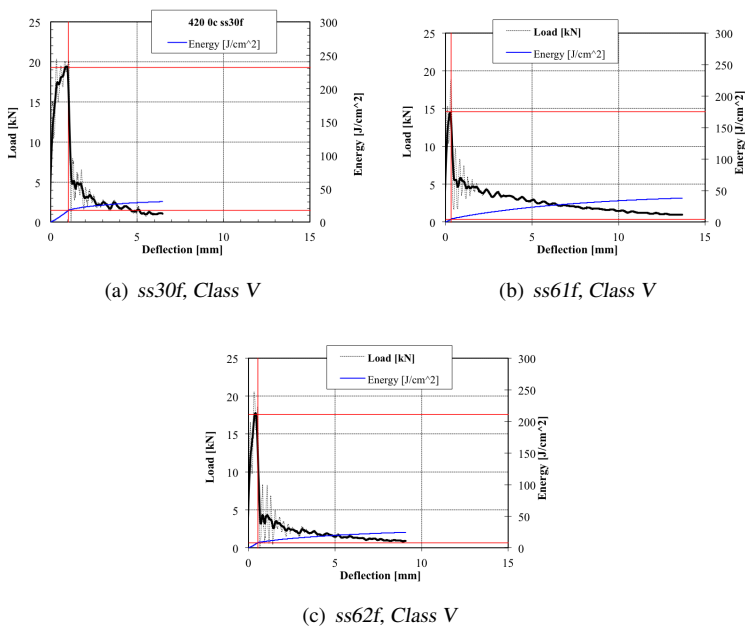


Figure C.21: CGHAZ, pre-cracked specimens tested at 0°C .

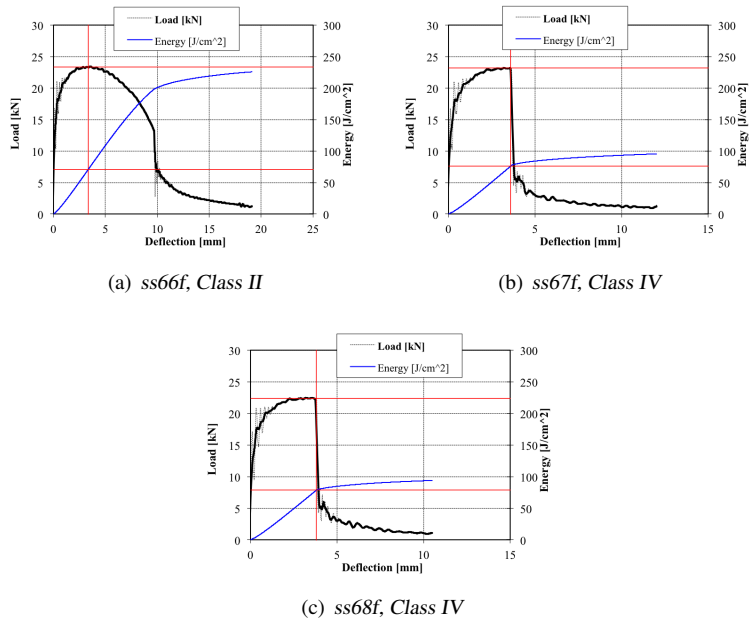


Figure C.22: CGHAZ, pre-cracked specimens tested at 11°C.

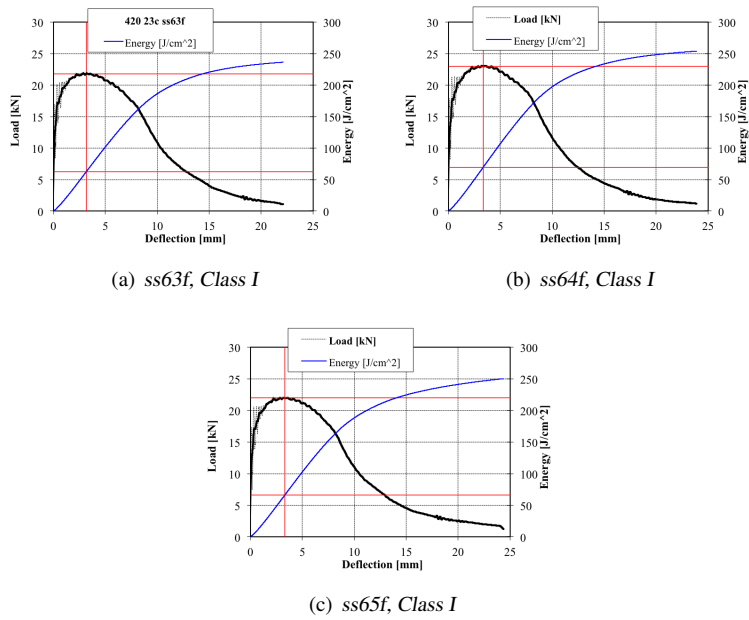


Figure C.23: CGHAZ, pre-cracked specimens tested at 23°C.

C.5 ICCGHAZ V-notched

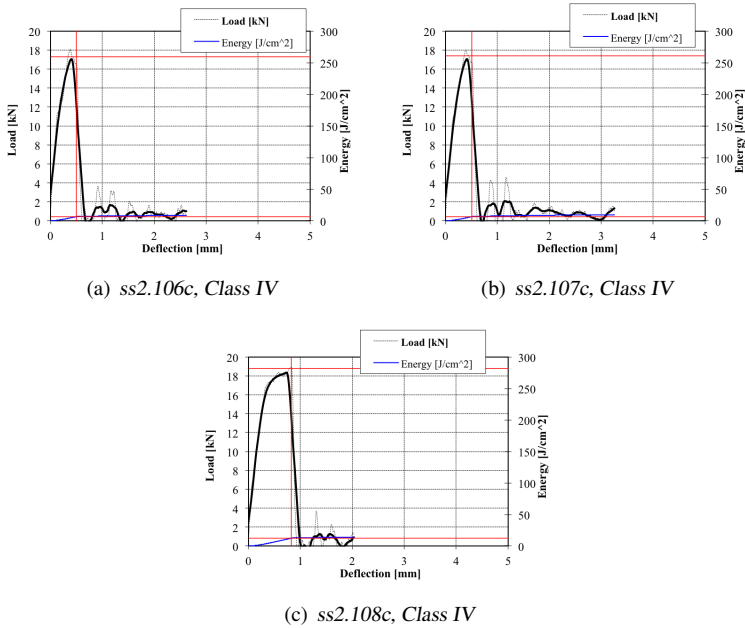


Figure C.24: ICCGHAZ, V-notched specimens tested at -60°C .

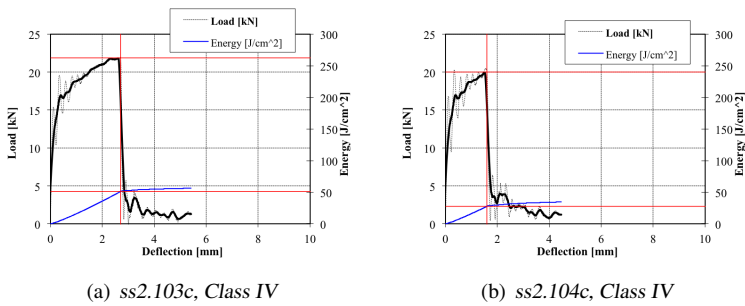


Figure C.25: ICCGHAZ, V-notched specimens tested at -30°C .

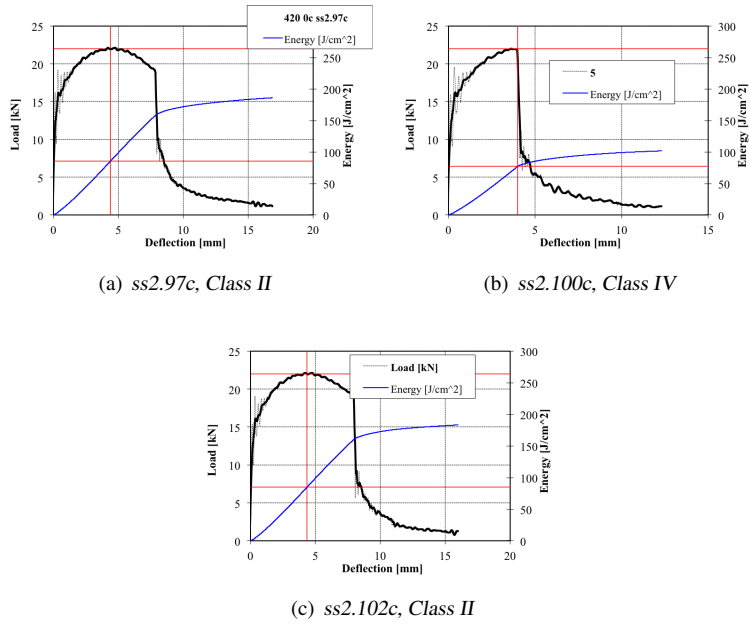


Figure C.26: ICCGHAZ, V-notched specimens tested at 0°C.

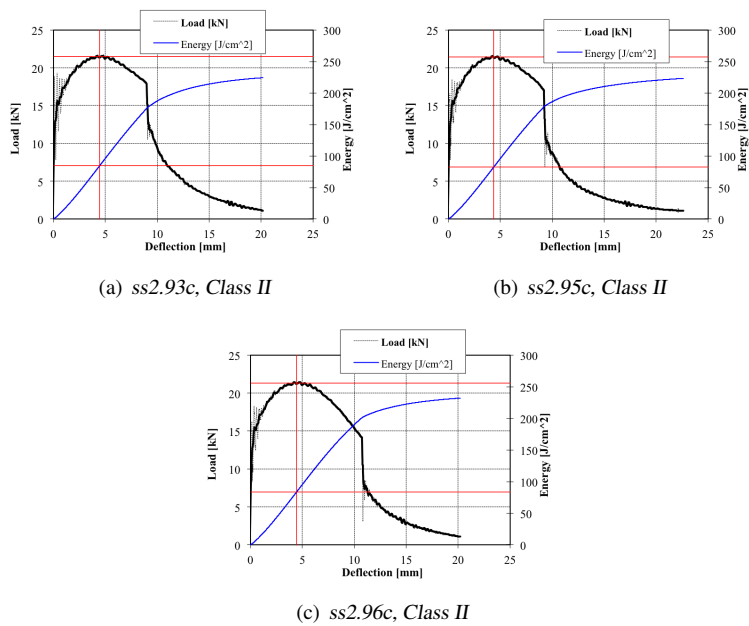


Figure C.27: ICCGHAZ, V-notched specimens tested at 23°C.

C.6 ICCGHAZ pre-cracked

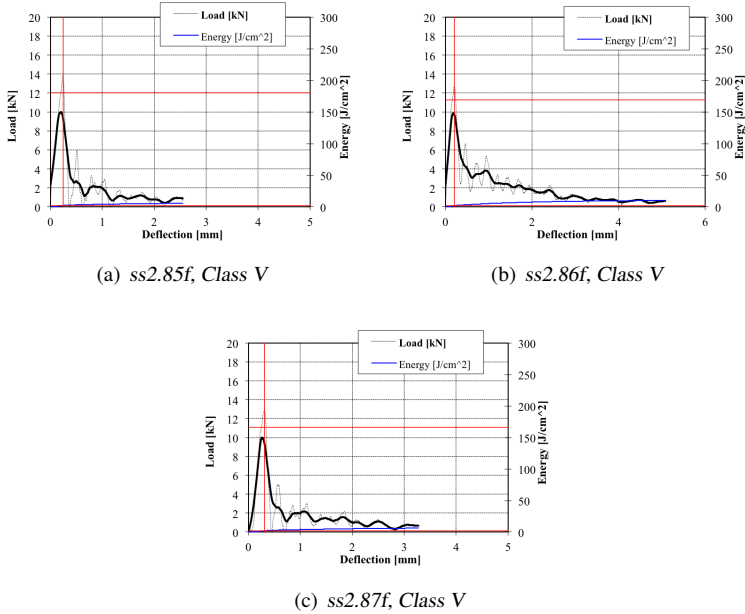


Figure C.28: ICCGHAZ, pre-cracked specimens tested at -60°C .

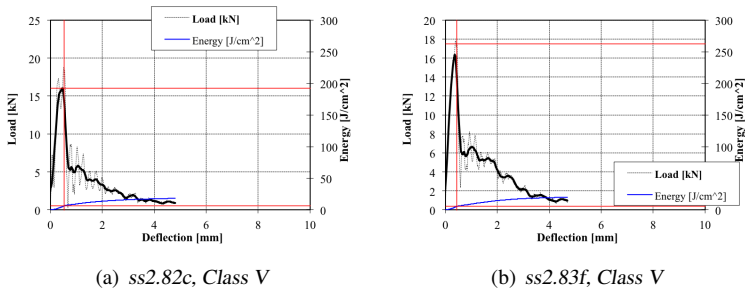


Figure C.29: ICCGHAZ, pre-cracked specimens tested at -30°C .

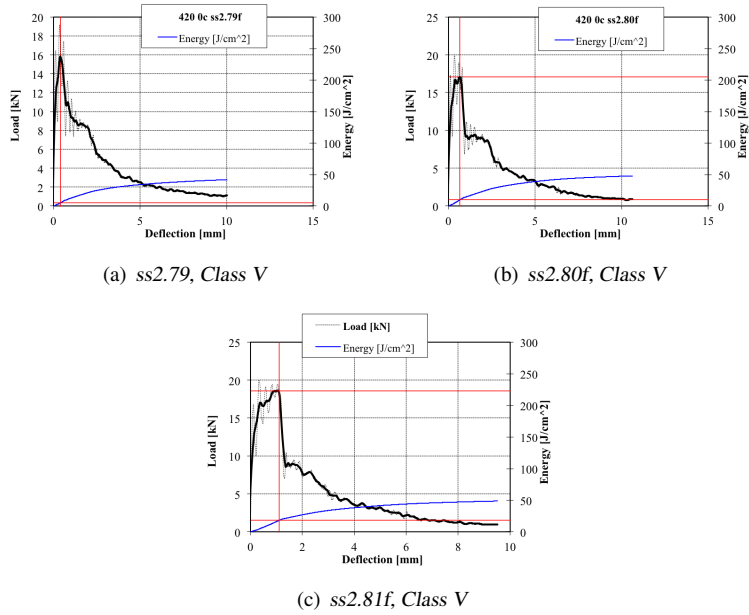


Figure C.30: ICCGHAZ, pre-cracked specimens tested at 0°C.

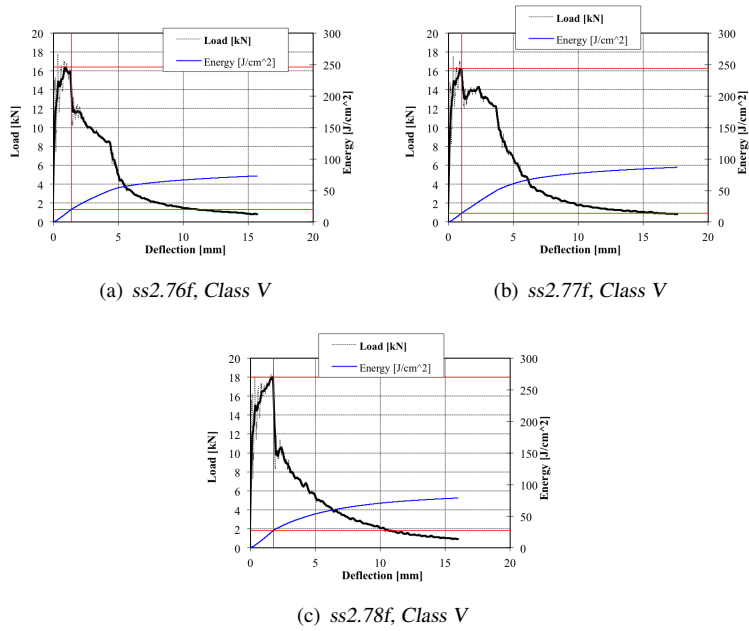


Figure C.31: ICCGHAZ, pre-cracked specimens tested at 23°C.

D Formal Problem Formulation

THE NORWEGIAN UNIVERSITY
OF SCIENCE AND TECHNOLOGY
DEPARTMENT OF ENGINEERING DESIGN
AND MATERIALS

MASTER THESIS SPRING 2014
FOR
STUD.TECHN. THERESE VADHOLM

INVESTIGATION OF LOW TEMPERATURE TOUGHNESS AND CRACK INITIATION IN WELDED STRUCTURAL STEELS

UNDERSØKELSE AV BRUDDSEIGHET VED LAVE TEMPERATURER OG BRUDDINITIERING I SVEISTE KONSTRUKSJONSSTÅL

As a lot of the world's undiscovered oil and natural gas reserves are believed to be located in northern areas, better materials that are able to withstand the harsh conditions in these areas are required. High strength, low alloy (HSLA) steels are designed for use in low temperature applications due to their accessible combinations of strength and toughness. Toughness is of special interest when investigating steels to be used in the northern areas, as sudden fracture can be a problem at low temperatures where the toughness is low and brittle failures are observed. Although HSLA steels generally provide good strength and toughness, they may also exhibit local brittle zones, like coexisting martensite and austenite phases, with detrimental results on the toughness of the steels, when they are welded. Previous work has indicated that fracture initiation can be linked to certain microstructural phases in different weld zones. In this regard, it is of interest to investigate the microstructure and fracture initiation sites in the weld zones of the candidate steels.

In qualification of welding procedures for structural applications, there is usually a requirement to employ Charpy V-notch testing since there are many decades of experience with the method, and the fact that it is simple, cheap and fast. Moreover, the use of the Charpy impact test to estimate material fracture toughness plays an important part in many material specifications, where Charpy values are used to establish design requirements for metals at minimum service temperatures in order to meet satisfactory safety levels. The current trend in the industry is to now employ more sophisticated methods of fracture toughness testing, like J or CTOD, as the industry needs to be more conservative when assessing new criteria for higher strength steels and thicker sections. It has been anticipated that Charpy tests performed with a sharp pre-crack could provide information about the meaning of the circular notch commonly used in Charpy specimens, and provide knowledge about the comparability to fracture mechanical tests, especially since the testing of welds and their resultant heat affected zones is complicated by their widely-varying microstructures.

The topics to be investigated will be:

- Characterization of microstructures in the heat affected zones of welded samples using optical light microscopy.
- Evaluation of brittle fracture initiation of samples tested at different temperature, both V notch and sharp crack.
- Comparison of transition curves for V notched and sharp cracked specimens.
- Comparison of instrumented Charpy tests with CTOD tests; all weld simulated samples.

The work will be carried out at UC Berkeley, CA, USA, in close cooperation with the Arctic Materials II project at SINTEF.

Three weeks after start of the thesis work, an A3 sheet illustrating the work is to be handed in. A template for this presentation is available on the IPM's web site under the menu "Masteroppgave" (<http://www.ntnu.no/ipm/masteroppgave>). This sheet should be updated one week before the Master's thesis is submitted.

Performing a risk assessment of the planned work is obligatory. Known main activities must be risk assessed before they start, and the form must be handed in within 3 weeks of receiving the problem text. The form must be signed by your supervisor. All projects are to be assessed, even theoretical and virtual. Risk assessment is a running activity, and must be carried out before starting any activity that might lead to injury to humans or damage to materials/equipment or the external environment. Copies of signed risk assessments should also be included as an appendix of the finished project report.

The thesis should include the signed problem text, and be written as a research report with summary both in English and Norwegian, conclusion, literature references, table of contents, etc. During preparation of the text, the candidate should make efforts to create a well-arranged and well-written report. To ease the evaluation of the thesis, it is important to cross-reference text, tables and figures. For evaluation of the work a thorough discussion of results is appreciated.

The thesis shall be submitted electronically via DAIM, NTNU's system for Digital Archiving and Submission of Master's thesis.

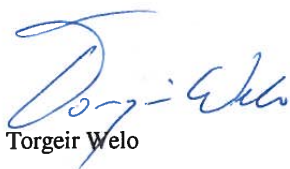
Contact persons are:

UC Berkley: Prof. Ronald Gronsky

SINTEF: Dr. Håkon Ottar Nordhagen

DNV: Dr. Erling Østby

NTNU: Prof. Odd M. Akselsen



Torgeir Welø



Head of Division



Odd M. Akselsen

Professor/Supervisor

E Risk Evaluation

NTNU	Hazardous activity identification process	Prepared by	Number	Date	
		HSE section	HMSRV-26/01	09.01.2013	
HSE		Approved by		Replaces	
		The Rector		01.12.2006	

Unit: *Materials Science and Engineering*

Date: 10.02.2014

Line manager:

Participants in the identification process (including their function): **Therese Vadholm, student**

Short description of the main activity/main process: Master project for student Therese Vadholm. Project Title: **INVESTIGATION OF LOW TEMPERATURE TOUGHNESS AND CRACK INITIATION IN WELDED STRUCTURAL STEELS**

The student will perform investigations of fracture samples in Optical Light Microscope and Scanning Electron Microscope and perform the needed sample preparation.

Is the project work purely theoretical? (YES/NO): NO

Signatures: *Responsible supervisor: Odd Magne Akselsen*

Student: Therese Vadholm

Note: *Risk evaluation is performed in accordance with applicable rules for the work performed at the external institution.*

ID nr.	Activity/process	Responsible person	Existing documentation	Existing safety measures	Laws, regulations etc.	Comment
	SEM Microscopy		Passed safety test	Training and obligatory safety tests, PPE rules	See note	
	Sample Preparation			Safety training, PPE rules	See note	
	Optical Light Microscopy			Safety training, PPE rules	See note	

 NTNU HSE/KS	Risk assessment	Prepared by	Number	Date	
		HSE section	HMSRV2603E	04.02.2011	
		Approved by		Replaces	
		The Rector		01.12.2006	

Unit: *Materials Science and Engineering*

Date: 10.02.2014

Line manager:

Participants in the identification process (including their function): **Therese Vadholm, student**

Short description of the main activity/main process: Master project for student Therese Vadholm. Project Title:
INVESTIGATION OF LOW TEMPERATURE TOUGHNESS AND CRACK INITIATION IN WELDED STRUCTURAL STEELS

The student will perform investigations of fracture samples in Optical Light Microscope and Scanning Electron Microscope and perform the needed sample preparation.


Is the project work purely theoretical? (YES/NO): NO

Signatures: *Responsible supervisor: Odd Magne Akselsen*

Student: Therese Vadholm

Note: *Risk evaluation is performed in accordance with applicable rules for the work performed at the external institution.*

Activity from the identification process form	Potential undesirable incident/strain	Likelihood: Likelihood (1-5)	Consequence:			Risk Value (human)	Comments/status Suggested measures
			Human (A-E)	Environment (A-E)	Economy/ material (A-E)		
Sample preparation	Damaged fingers during grinding and polishing of the samples.	2	A				Automated sample machining can be used. Use of existing procedures and make sure that fingers are safe during the process. Safety glasses and lab coat should be used during the process.
SEM Microscopy	Damaging equipment	2			C		Expensive SEM equipment may be damaged if the user is not precautious. Comprehensive training on the SEM to be used is

NTNU 	Risk assessment	Prepared by	Number	Date	
		HSE section	HMSRV2603E	04.02.2011	
HSE/KS	Approved by		Replaces		
	The Rector		01.12.2006		

							performed and followed up frequently.
Optical Light Microscopy	Damaging equipment	2				B	Equipment may be damaged if the user is not precautions. Training on and introduction to the equipment to be used should be performed before the work on the instrument can start.

Likelihood, e.g.:

1. Minimal
2. Low
3. Medium
4. High
5. Very high

Consequence, e.g.:

- A. Safe
- B. Relatively safe
- C. Dangerous
- D. Critical
- E. Very critical

Risk value (each one to be estimated separately):

- Human = Likelihood x Human Consequence**
Environmental = Likelihood x Environmental consequence
Financial/material = Likelihood x Consequence for Economy/materiel

Potential undesirable incident/strain

Identify possible incidents and conditions that may lead to situations that pose a hazard to people, the environment and any materiel/equipment involved.

Criteria for the assessment of likelihood and consequence in relation to fieldwork


Each activity is assessed according to a worst-case scenario. Likelihood and consequence are to be assessed separately for each potential undesirable incident. Before starting on the quantification, the participants should agree what they understand by the assessment criteria:

Likelihood

Minimal 1	Low 2	Medium 3	High 4	Very high 5
Once every 50 years or less	Once every 10 years or less	Once a year or less	Once a month or less	Once a week

Consequence

Grading	Human	Environment	Financial/material
E Very critical	May produce fatality/ies	Very prolonged, non-reversible damage	Shutdown of work >1 year.
D	Permanent injury, may produce	Prolonged damage. Long	Shutdown of work 0.5-1 year.

NTNU  HSE/KS	<h2 style="margin: 0;">Risk assessment</h2>	Prepared by	Number	Date	
		HSE section	HMSRV2603E	04.02.2011	
		Approved by The Rector		Replaces 01.12.2006	

Critical	serious serious health damage/sickness	recovery time.	
C Dangerous	Serious personal injury	Minor damage. Long recovery time	Shutdown of work < 1 month
B Relatively safe	Injury that requires medical treatment	Minor damage. Short recovery time	Shutdown of work < 1 week
A Safe	Injury that requires first aid	Insignificant damage. Short recovery time	Shutdown of work < 1 day


The unit makes its own decision as to whether opting to fill in or not consequences for economy/materiel, for example if the unit is going to use particularly valuable equipment. It is up to the individual unit to choose the assessment criteria for this column.

Risk = Likelihood x Consequence

Please calculate the risk value for "Human", "Environment" and, if chosen, "Economy/materiel", separately.

About the column "Comments/status, suggested preventative and corrective measures":

Measures can impact on both likelihood and consequences. Prioritise measures that can prevent the incident from occurring; in other words, likelihood-reducing measures are to be prioritised above greater emergency preparedness, i.e. consequence-reducing measures.

NTNU	Risk matrix	prepared by	Number	Date
		HSE Section	HMSRV2604	8 March 2010
HSE/KS		approved by	Page	Replaces
		Rector	4 of 4	9 February 2010

MATRIX FOR RISK ASSESSMENTS at NTNU

CONSEQUENCE	Extremely serious	E1	E2	E3	E4	E5
	Serious	D1	D2	D3	D4	D5
	Moderate	C1	C2	C3	C4	C5
	Minor	B1	B2	B3	B4	B5
	Not significant	A1	A2	A3	A4	A5
		Very low	Low	Medium	High	Very high
		LIKELIHOOD				

Principle for acceptance criteria. Explanation of the colours used in the risk matrix.

Colour	Description
Red	Unacceptable risk. Measures must be taken to reduce the risk.
Yellow	Assessment range. Measures must be considered.
Green	Acceptable risk Measures can be considered based on other considerations.

List of Figures

1.1	The Arctic Region	2
1.2	LAST and SMYS requirements for steel structures	3
2.1	The iron-carbon phase diagram	7
2.2	The BCT lattice	10
2.3	IT-diagram	11
2.4	Upper and lower bainite	12
2.5	Schematic transition curve	17
2.6	Strength versus toughness	20
2.7	Fusion zone and HAZ	23
2.8	CCT diagram of HSLA 100 steel	24
2.9	HAZ in single pass welds	25
2.10	Weld zones in single-pass welds	26
2.11	HAZ in single- and multi-pass welding	27
2.12	Initiation mechanisms due to presence of MA phase	32
2.13	Changes in measured fracture toughness with thickness variation	33
2.14	CTOD definitions	35
2.15	CTOD specimen and test set-up	36
2.16	Standard Charpy V-notch specimen	38
2.17	Shear area in Charpy testing	39
2.18	Force parameters on instrumented Charpy curve	41
2.19	Arrest toughness	46
3.1	Master Curve and T_0 position	57
3.2	Transition curves from previous work	59
3.3	Curve classes	61

3.4	Examples of fracture surfaces of the different curve classes	62
3.5	Curve types in NS-EN ISO 14556	62
3.6	Location of the different curve classes on the Charpy transition curve	65
4.1	Weld simulation process and parameters	68
4.2	Crack position in CTOD and SENB specimens	69
4.3	Charpy machine and test set-up used	70
4.4	Sample studied in OLM	76
4.5	SEM investigated specimens	77
5.1	Transition curves from instrumented Charpy data	87
5.2	Transition curve using lower bound values	88
5.3	Distribution of $C_{V,m}$ as a function of temperature	92
5.4	Distribution of $C_{V,f}$ as a function of temperature	93
5.5	Distribution of $\frac{C_{V,m}}{C_{V,c}}$ and $\frac{C_{V,f}}{C_{V,c}}$ as a function of curve class	96
5.6	Distribution of $\frac{C_{V,m}}{C_{V,c}}$ as a function of temperature	97
5.7	Distribution of $\frac{C_{V,f}}{C_{V,c}}$ as a function of temperature	98
5.8	Measured CTOD values	100
5.9	Micrographs of CGHAZ, V-notched,-30°C	102
5.10	Micrographs of CGHAZ, V-notched,-60 °C	103
5.11	Micrographs of CGHAZ, pre-cracked,0°C	104
5.12	Micrographs of CGHAZ, pre-cracked,-30°C	105
5.13	Micrographs of ICCGHAZ, V-notched,-30°C.	106
5.14	Micrographs of ICCGHAZ, V-notched,-60°C.	107
5.15	Micrographs of ICCGHAZ, V-notched,0°C.	108
5.16	Micrographs of ICCGHAZ, V-notched,-30°C.	109
5.17	Micrographs of ICCGHAZ, V-notched,-60 °C.	110
5.18	Microstructure of base material, etched using 2% Nital, 50X	112
5.19	Microstructure of base material, etched using LaPera, 50X	112
5.20	Microstructure CGHAZ, etched using 2 % Nital, 50X	113
5.21	Microstructure CGHAZ, etched using LaPera, 50X	113
5.22	Microstructure ICCGHAZ, etched using 2 % Nital, 50X	114
5.23	Microstructure ICCGHAZ, etched using LaPera, 50X	114

5.24 Estimation of CTOD using BS7910	116
5.25 Master Curve - ICCGHAZ, $T_k=25$, $B=10$	118
5.26 Master Curve using alternative T_0 equation - $T_k=25$, $B=10$	119
5.27 Master Curve - $T_k=0$, $B=10$	120
5.28 Master Curve - for pre-cracked series	121

List of Tables

3.1	Physical differences between Charpy and quasi-static fracture tests	51
4.1	Chemical composition of investigated steel.	67
4.2	Applied parameters for the thermal weld simulation process.	68
4.3	Charpy test performed.	72
4.4	CTOD test performed.	73
4.5	Sample preparation sequence for investigation in OLM. All equipment from Struers.	75
4.6	The samples investigated in SEM.	77
5.1	Average measured C_V values	86
5.2	Fraction of energy calculated up to maximum load	95
5.3	Average measured CTOD	100
5.4	Temperatures used in estimation of T_0	117